

A COMPREHENSIVE STUDY OF HYDRODYNAMIC PROCESSES
AT THE GALACTIC CENTER

by
Gabriel Matthew Rockefeller

A Dissertation Submitted to the Faculty of the
DEPARTMENT OF PHYSICS
In Partial Fulfillment of the Requirements
For the Degree of
DOCTOR OF PHILOSOPHY
In the Graduate College
THE UNIVERSITY OF ARIZONA

2 0 0 6

THE UNIVERSITY OF ARIZONA
GRADUATE COLLEGE

As members of the Dissertation Committee, we certify that we have read the dissertation prepared by Gabriel Matthew Rockefeller entitled “A Comprehensive Study of Hydrodynamic Processes at the Galactic Center” and recommend that it be accepted as fulfilling the dissertation requirement for the Degree of Doctor of Philosophy.

Fulvio Melia Date: 8/24/2006

Christopher Fryer Date: 8/24/2006

Keith Dienes Date: 8/24/2006

Alex Cronin Date: 8/24/2006

Philip Pinto Date: 8/24/2006

Final approval and acceptance of this dissertation is contingent upon the candidate’s submission of the final copies of the dissertation to the Graduate College.

I hereby certify that I have read this dissertation prepared under my direction and recommend that it be accepted as fulfilling the dissertation requirement.

Dissertation Co-Director: Fulvio Melia Date: 8/24/2006

Dissertation Co-Director: Christopher Fryer Date: 8/24/2006

STATEMENT BY AUTHOR

This dissertation has been submitted in partial fulfillment of requirements for an advanced degree at The University of Arizona and is deposited in the University Library to be made available to borrowers under rules of the Library.

Brief quotations from this dissertation are allowable without special permission, provided that accurate acknowledgment of source is made. Requests for permission for extended quotation from or reproduction of this manuscript in whole or in part may be granted by the head of the major department or the Dean of the Graduate College when in his or her judgment the proposed use of the material is in the interests of scholarship. In all other instances, however, permission must be obtained from the author.

SIGNED: Gabriel Matthew Rockefeller

ACKNOWLEDGMENTS

First, I want to thank Chris Fryer and Fulvio Melia. I came to The University of Arizona specifically to work with Fulvio, and I came to Los Alamos National Laboratory specifically to work with Chris; in each case I found a fantastic advisor and mentor.

I also want to thank Mike Warren, for showing me how serious computational work ought to be done, and Aimee Hungerford, for lots of helpful conversations and for sponsoring me for a postdoc position at LANL. I'd also like to thank Fred Baganoff and Daniel Wang, who each provided *Chandra* data and collaborated with me on some of the projects presented here.

Many former and current Tucson residents deserve credit for keeping me sane while I was living there. Sara LaFontain deserves special thanks for helping me escape from physics when I needed to. I owe much beer to (in alphabetical order) Jerome Buerki, Tommy Burch, Torsten Falk, Mike Fromerth, Eric Gregory, Jörg Hader, Jason Hamm, Bill Hunter, Jeremy Jones, Mike Lennek, Sarah Kenyon, Adam Newcomer, Paul Pax, Worawarong Rakreungdet, Daniel Shorb, Jeff Temple, and Giorgio Torrieri. I particularly want to thank Todd Thompson and Katra Byram for great conversations and dinners in Tucson and elsewhere.

This research was supported by NASA under grants NAG5-8239, NAG5-9205, and SWIF03-0047-0037, and by NSF grant AST-0402502. This work was funded under the auspices of the U.S. Dept. of Energy, and supported by its contract W-7405-ENG-36 to Los Alamos National Laboratory and by a DOE SciDAC grant DE-FC02-01ER41176. This research used resources of the National Energy Research Scientific Computing Center, which is supported by the Office of Science of the U.S. Department of Energy under Contract No. DE-AC03-76SF00098. Many of the simulations were conducted on the Space Simulator and Pink at Los Alamos National Laboratory.

DEDICATION

To my parents, Barbara and Larry

TABLE OF CONTENTS

LIST OF FIGURES	9
LIST OF TABLES	11
ABSTRACT	12
CHAPTER 1 INTRODUCTION TO THE GALACTIC CENTER	13
1.1 Components of the Galactic Center Region	14
1.1.1 The Central Supermassive Black Hole Sgr A*	14
1.1.2 Stars in the Central Parsec	16
1.1.3 The Circumnuclear Disk	17
1.1.4 Sgr A East	18
1.2 Research Objectives	20
CHAPTER 2 DIFFUSE X-RAYS FROM THE INNER 3 PARSECS OF THE GALAXY	22
2.1 Introduction	22
2.2 The Physical Setup	26
2.2.1 Boundary Conditions	27
2.2.2 Circumnuclear Disk	27
2.2.3 Wind Sources	29
2.3 The Gas Profile and Spectrum	33
2.4 Discussion	43
CHAPTER 3 DIFFUSE X-RAYS FROM THE ARCHES AND QUINTUPLET CLUS- TERS	45
3.1 Introduction	45
3.1.1 The Arches Cluster	47
3.1.2 The Quintuplet Cluster	52
3.2 The Physical Setup	59
3.2.1 Cluster Potential	60
3.2.2 Wind Sources	61
3.3 Observations	62
3.4 Results	63
3.4.1 Total Flux and Time Variation	63
3.4.2 Spatial Variation of the X-ray Flux	67
3.5 Discussion	72
CHAPTER 4 THE X-RAY RIDGE SURROUNDING SGR A* AT THE GALACTIC CENTER	75
4.1 Introduction	75

TABLE OF CONTENTS — *Continued*

4.2	General Physical Principles	78
4.3	Calculations and Results	79
4.4	Conclusion	83
CHAPTER 5 THE SGR B2 X-RAY ECHO OF THE GALACTIC CENTER SUPERNOVA EXPLOSION THAT PRODUCED SGR A EAST 86		
5.1	Introduction	86
5.2	The Puzzle of Sgr B2	88
5.3	Supernova Shocks at the Galactic Center	90
5.4	Time-dependent Accretion Onto Sgr A*	95
5.5	Evolution of the Sgr A East Remnant	98
5.6	Other Constraints on the Recent Galactic Center Supernova	102
5.7	Conclusions	106
CHAPTER 6 SPIN-INDUCED DISK PRECESSION IN SAGITTARIUS A* 118		
6.1	Introduction	118
6.2	Physical Principles and Method	120
	6.2.1 The Conservation Equations and SPH Code	121
	6.2.2 The Anomalous Viscosity	122
6.3	Results	123
6.4	Conclusions	129
APPENDIX A SMOOTHED PARTICLE HYDRODYNAMICS: ALGORITHM AND CODE DETAILS 131		
A.1	Introduction	131
A.2	Physics Implementation	132
	A.2.1 Gravity	132
	A.2.2 SPH Hydrodynamics	134
	A.2.2.1 Brief SPH Primer	134
	A.2.2.2 Continuity Equation	137
	A.2.2.3 Momentum Equation	137
	A.2.2.4 Energy Conservation	138
	A.2.2.5 Artificial Viscosity	139
	A.2.2.6 Equation of State	140
A.3	Computational Issues	140
	A.3.1 Treecode	141
	A.3.1.1 Key Construction	142
	A.3.1.2 Hashing	143
	A.3.1.3 Tree Construction	144

TABLE OF CONTENTS — *Continued*

A.3.2	Parallelization	145
A.3.3	Time integration	146
A.4	Code Tests	147
A.4.1	Sedov-Taylor Blast Wave	149
A.4.2	Adiabatic Collapse	152
A.4.3	Binary Orbits: Testing Angular Momentum Conservation . . .	154
A.5	Conclusions	160
REFERENCES	166

LIST OF FIGURES

FIGURE 2.1	Locations of Galactic Center wind sources	30
FIGURE 2.2	Isosurfaces of specific internal energy	35
FIGURE 2.3	X-ray luminosity from Simulation 1	36
FIGURE 2.4	X-ray luminosity from Simulation 2	37
FIGURE 2.5	X-ray luminosity radial profile	39
FIGURE 2.6	Temperature radial profile	40
FIGURE 2.7	X-ray luminosity contours from Simulation 1	41
FIGURE 2.8	X-ray luminosity contours from Simulation 2	42
FIGURE 3.1	Locations of Arches cluster wind sources	53
FIGURE 3.2	Locations of Quintuplet cluster wind sources	55
FIGURE 3.3	<i>Chandra</i> X-ray contours overlaid on <i>HST</i> Arches image . . .	64
FIGURE 3.4	X-ray luminosity from Arches cluster simulations	66
FIGURE 3.5	X-ray luminosity from Quintuplet cluster simulations	67
FIGURE 3.6	X-ray contours from Arches cluster simulations	68
FIGURE 3.7	X-ray contours from Quintuplet cluster simulations	69
FIGURE 3.8	Cumulative radial profiles of X-ray luminosity	70
FIGURE 3.9	Simulated radial profiles of X-ray flux per arcmin ²	71
FIGURE 3.10	Average radial velocity of gas in the cluster simulations . . .	72
FIGURE 4.1	<i>Chandra</i> image of the central square arcminute	77
FIGURE 4.2	Simulated density contours	80
FIGURE 4.3	Contours of X-ray luminosity at four different times	84
FIGURE 5.1	Simulated density profile of the Galactic Center	91
FIGURE 5.2	Simulated density contours	92
FIGURE 5.3	Simulated density contours from the 1.5×10^{51} erg explosion	109
FIGURE 5.4	Simulated density contours from the 1.2×10^{52} erg explosion	111
FIGURE 5.5	Accretion rate and accreted specific angular momentum . . .	113
FIGURE 5.6	Velocity radial profiles	114
FIGURE 5.7	Simulated high-energy emission	115
FIGURE 5.8	X-ray luminosity from simulated arc toward Sgr A East . . .	116
FIGURE 5.9	Isosurfaces of nickel, iron, titanium, and magnesium	117
FIGURE 6.1	SPH particles in a simulated warped disk	125
FIGURE 6.2	SPH particles in a simulated Galactic Center disk	126
FIGURE 6.3	Precession period versus disk size	128

LIST OF FIGURES — *Continued*

FIGURE A.1	Sedov blast wave profile	150
FIGURE A.2	Energy evolution during adiabatic collapse	153
FIGURE A.3	Diagram of forces between SPH particles	155
FIGURE A.4	Snapshots of a self-gravitating binary system	158
FIGURE A.5	Orbital separation and angular momentum of binary system	159
FIGURE A.6	Energy evolution of binary system	161
FIGURE A.7	Angular momentum and angular velocity profiles	162

LIST OF TABLES

TABLE 2.1	Galactic Center wind simulation properties	27
TABLE 2.2	Parameters for Galactic Center wind sources	32
TABLE 3.1	Parameters for the Arches Cluster wind sources	50
TABLE 3.2	Parameters for the Quintuplet Cluster wind sources	57
TABLE 3.3	Properties of the Arches and Quintuplet clusters	61
TABLE 5.1	Sgr A East simulation properties	96
TABLE 6.1	Galactic Center disk simulation properties	124

ABSTRACT

Our Galactic center hosts the closest known supermassive black hole candidate. With a mass of approximately 3.7 million solar masses, this compact object, known as Sgr A*, has a considerable influence on the central parsecs of the Galaxy. However, many observed features of the Galactic center result from the presence of and interactions among other stellar and gaseous components, including clusters of massive, wind-producing stars, ionized gas streamers, dense molecular clouds, and supernova remnants. We present a series of simulations and studies of the interactions among these components. In each case, we attempt to explain a particular feature or present a new interpretation of recent observations of the Galactic center. Our simulations of interactions among stellar winds in the central parsec of the Galaxy and in the Arches and Quintuplet clusters are able to explain the diffuse X-ray emission observed there by the *Chandra* X-ray Observatory. Similarly, our simulations of the explosive formation of the synchrotron shell source Sgr A East place tight constraints on the age and progenitor of such an explosion and might explain the observed X-ray fluorescence of molecular clouds at larger distances from the Galactic center. Finally, our studies of accretion disks around Sgr A* provide a first three-dimensional look at the structure of the accretion flow onto this supermassive black hole and pave the way for full simulations of accretion from length scales of parsecs down to Schwarzschild radii.

CHAPTER 1

INTRODUCTION TO THE GALACTIC CENTER

It seems natural for physicists to investigate the behavior of matter under extreme conditions and circumstances. A relationship that is postulated based only on research under typical Earth-like conditions—temperatures, densities, length and time scales, for example—might not and certainly shouldn't be expected to be true under different conditions. Given skill and a sufficient level of technology, some ranges of physical parameters can be probed in a laboratory; for example, a physicist might investigate the behavior of matter at extremely low temperatures using an apparatus that fits inside a normal laboratory space, or a team of physicists might study the interactions of fundamental particles at very high energies using a large accelerator. Similarly, astrophysicists often study environments or phenomena that are too large or massive or dense or hot to be studied in a terrestrial laboratory (although there certainly is great value in extrapolating astrophysical phenomena to smaller scales so that they can be examined at close range, in a lab setting).

Centers of galaxies are logical locations to search for extreme physical conditions and exotic phenomena. Gas temperatures in galactic centers are high, star formation rates are high, and we now believe that many galaxies are hosts to central supermassive black holes.

The center of our Galaxy lies in the constellation Sagittarius (abbreviated Sgr). The radio source Sgr A* was discovered at the center of the Sgr A complex by Balick & Brown (1974), and it is now believed to be the radio counterpart of a supermassive black hole at the center of the Galaxy. Ghez et al. (2005) have followed the orbits

of stars around Sgr A* and have determined that the mass of this central object is $(3.7 \pm 0.2) \times 10^6 [R_0 / (8 \text{ kpc})]^3 M_\odot$, where R_0 is the distance to the Galactic center.

The inner few parsecs of the Galaxy contain several observed components that coexist within the central deep gravitational potential well. Sgr A* is surrounded by a cluster of evolved and young stars, a torus of molecular material, ionized gas streamers, diffuse hot gas and Sgr A East, a shell-like synchrotron source believed to be the remnant of a supernova explosion (see Melia & Falcke, 2001). Observations at many different wavelengths and with many different instruments have been very effective in unraveling the complex behavior of the central components through their mutual interactions. While Sgr A* dominates the gravitational dynamics in the central parsecs of the Galaxy, the presence and interactions of the other central components are required to explain many observational features.

1.1 Components of the Galactic Center Region

1.1.1 The Central Supermassive Black Hole Sgr A*

At the Galactic center, the compact radio source Sgr A* appears to be the radiative manifestation of an accreting $3.7 \times 10^6 M_\odot$ supermassive black hole (Ghez et al., 2005). Its radio to mm spectrum is thought to be a composite of two principal components—a slightly inverted power-law with a notable bump at mm/sub-mm wavelengths. The latter is somewhat reminiscent of the “big blue bump” seen in many Active Galactic Nuclei (AGNs), evidently produced by an accretion disk feeding the supermassive black hole (see, e.g., Brotherton et al., 2001). But unlike the blackbody emission process that gives rise to the optical/UV thermal feature in an AGN spectrum, the radiative mechanism responsible for Sgr A*’s mm/sub-mm spectral excess appears instead to be a combination of thermal and non-thermal synchrotron emission within the inner portion ($r < 10 r_S$) of a hot, magnetized

Keplerian flow (Melia et al., 2001; Liu & Melia, 2001). (The Schwarzschild radius, r_S , for an object of this mass M is $2GM/c^2 \approx 10^{12}$ cm, or roughly 1/15 A.U.) The inferred characteristics of the compact region surrounding Sgr A* are also consistent with the $\sim 10\%$ linear polarization detected from this source at mm wavelengths (Melia et al., 2000; Bromley et al., 2001). Given the complex spatial arrangement of the mass-losing stars that feed this object, it is unlikely that the disk angular momentum axis is aligned with the spin axis of the black hole.

The rate of accretion of matter onto Sgr A* must be well below the Eddington rate, since the observed bolometric luminosity is ~ 8 orders of magnitude below the Eddington value ($L_{bol} \simeq 10^{36}$ erg s $^{-1}$ vs. $L_{Edd} \simeq 5 \times 10^{44}$ erg s $^{-1}$). Observers using *Chandra* have estimated a mass accretion rate $\dot{M} \simeq 3 \times 10^{-6} M_\odot/\text{yr}$ at $\sim 10^5$ Schwarzschild radii from Sgr A* (Baganoff et al., 2003); Bower et al. (2003) measured the linear polarization of radio emission from within $10r_S$ of Sgr A* and inferred an accretion rate of $\sim 10^{-8} M_\odot/\text{yr}$. On the other hand, estimates of the Bondi-Hoyle capture rate for gas onto the black hole (based on the mass of the black hole and the density and velocity of material in the surrounding environment) are much higher—as much as $\dot{M}_{Bondi} = 10^{-4} M_\odot/\text{yr}$. If that quantity of matter were indeed captured by the black hole at the Bondi-Hoyle capture radius $r_{Bondi} = 2GM/v_{wind}^2 \simeq 2.5 \times 10^{17}$ cm, it must either be extremely inefficient at radiating away energy as it accretes, or most of it must eventually be ejected in an outflow. However, the environment around Sgr A* is not particularly homogeneous, and there is no particular reason to expect that the flow past Sgr A* should feed the black hole at the Bondi-Hoyle rate. In fact, a combination of sub-Bondi-Hoyle capture rate, low-radiative-efficiency accretion, and eventual ejection of most of the captured material can probably explain the low luminosity of Sgr A*, although this particular hypothesis is not tested in this work.

1.1.2 Stars in the Central Parsec

The center of the Galaxy evidently supports the formation of a large number of massive stars. The Arches and Quintuplet star clusters, located ~ 25 pc from Sgr A*, are among the most massive in the Galaxy, and the so-called Central cluster that surrounds Sgr A* contains a similarly large number of O and Wolf-Rayet stars (Tanner et al., 2006).

There is ample observational evidence in this region for the existence of rather strong outflows in and around the Sgr A complex. Measurements of high velocities associated with IR sources in Sgr A West (Krabbe et al., 1991) and in IRS 16 (Geballe et al., 1991), the H_2 emission in the molecular ring and from molecular gas being shocked by a nuclear mass outflow (Gatley et al., 1986; but see Jackson et al., 1993 for the potential importance of UV photodissociation in promoting this H_2 emission), broad Br α , Br γ and He I emission lines from the vicinity of IRS 16 (Hall et al., 1982; Allen et al., 1990; Geballe et al., 1991), and radio continuum observations of IRS 7 (Yusef-Zadeh & Melia, 1991), provide clear evidence of a hypersonic wind, with a velocity $v_w \sim 500\text{--}1,000$ km s $^{-1}$, a number density $n_w \sim 10^{3-4}$ cm $^{-3}$, and a total mass loss rate $\dot{M}_w \sim 3\text{--}4 \times 10^{-3} M_\odot \text{ yr}^{-1}$, pervading the inner parsec of the Galaxy.

Tanner et al. (2006) have published the most recent observations and spectra of stars in the Central cluster, but many groups have studied these stars over the past several decades (e.g. Geballe et al., 1987; Najarro et al., 1997; Paumard et al., 2001). The work reported in this dissertation used these data primarily to constrain the spectral types, mass-loss rates, and wind velocities of the massive stars in the central parsec (and in the Arches and Quintuplet clusters, for the work reported in chapter 3). The larger community of Galactic center theorists and observers is interested in these observations not only because they constrain properties of the

individual stars in these clusters, but also because they firmly establish the simple presence of a large number of massive stars in the center of the Galaxy. In fact, the Arches, Quintuplet, and Central clusters account for most of the known O and Wolf-Rayet stars in the Galaxy. The Arches and Quintuplet clusters are interesting because of the apparently top-heavy initial mass function (IMF) for their constituent stars; the Central cluster is even more interesting because it lies within a fraction of a parsec of Sgr A*. Formation scenarios for the Central cluster and the stars within it range from *in situ* formation—when a particularly dense molecular cloud passed across Sgr A*—to the infall of a massive cluster formed at a larger distance from Sgr A*, to three-body interactions between a massive cluster and a hypothetical intermediate-mass black hole (IMBH). The small cluster known as IRS 13 might be the remnant of the core of such a massive cluster, and might potentially harbor an IMBH (Maillard et al., 2004).

1.1.3 The Circumnuclear Disk

The central parsec of the Galaxy is surrounded by a clumpy ring of molecular material known as the circumnuclear disk (CND). The CND has a well-defined inner edge at 1.5 pc and an outer edge around 3–4 pc from Sgr A*; it has a thickness of ~ 0.4 pc at the inner edge and expands to a thickness of ~ 2 pc at larger radii (Christopher et al., 2005). Observations of molecular material (HCN and HCO⁺) in clumps in the torus place the total estimated mass of the torus at $10^6 M_{\odot}$. The volume filling factor of dense clumps in the torus is low—approximately 1%. The torus is evidently orbiting the black hole; observations by Christopher et al. (2005) show a clear pattern of radial velocities indicating that the torus is inclined by 50–75 degrees from the line of sight and is orbiting around Sgr A*.

The CND is perhaps the shredded remains of a giant molecular cloud that passed by Sgr A*. The cavity within the inner ~ 2 pc of this structure may itself have

been created by the ablative influence of the cumulative wind outflow from the Central cluster, which has by now produced a bubble of hot, ionized plasma. The observed dense cores in the CND are dense enough ($n = 10^7\text{--}10^8 \text{ cm}^{-3}$) to be tidally stable even in close proximity to the central supermassive black hole. In fact, such dense cores might have provided suitable sites for star formation near Sgr A* and contributed to the formation of the Central cluster.

1.1.4 Sgr A East

The conditions in the inner 3 pc of the Galaxy are set in large part by the complex interaction of over a dozen strong Wolf-Rayet star winds and the enveloping 50 km s^{-1} giant molecular cloud (M-0.02-0.07), combined with the strong gravitational pull of the central supermassive black hole (Sgr A*). The large number of massive stars in this compact region suggests an additional influence—that of supernova explosions. Sgr A East is the remnant of such an event. An earlier consideration of its interaction with the molecular cloud, based on the energetics and time required to carve out the central cavity now occupied by Sgr A East, pointed to an unusually powerful explosion, with an energy of $\sim 10^{52}$ ergs or greater, and a remnant age exceeding $\sim 10,000$ years (Mezger et al., 1989). These estimates, however, ignored the importance of the stellar winds in clearing out the medium into which the supernova ejecta expanded following the incipient event. In chapters 4 and 5 we show with detailed 3D hydrodynamic simulations that, when one takes this additional factor into account, the current morphology of Sgr A East is actually consistent with a normal supernova explosion energy ($\sim 10^{51}$ ergs). In addition, the relatively low gas density in the wind-filled region and the consequent more rapid expansion of the remnant into the surrounding medium leads to an inferred age much younger than 10,000 years, probably $< 2,000$ years.

Sgr A East is a non-thermal radio shell source centered ~ 2.5 pc to the east of

Sgr A*. It is approximately 8 pc long (aligned roughly with the Galactic plane) and 6 pc wide (perpendicular to the Galactic plane). Several studies (Mezger et al., 1989; Maeda et al., 2002; Herrnstein & Ho, 2005) have established that Sgr A East is interacting with other components in the Galactic center, including a set of gas streamers (Sgr A West) and several massive molecular clouds to the east (where observed OH masers mark the interaction sites). Mezger et al. (1989) detected a dust ring surrounding Sgr A East and suggested that this material had been swept up by an explosive event that produced Sgr A East, and both theorists and observers since then have suggested several different scenarios for the formation of this structure.

Mezger et al. (1989) proposed some of the earliest formation scenarios, and variations on those scenarios have dominated subsequent discussions of Sgr A East. Mezger et al. (1989) proposed four different scenarios: a supernova exploding directly into a molecular cloud; a supernova exploding into the wind bubble created by the progenitor star; an explosion near Sgr A* within gas with a proper motion that carried it ~ 2.5 pc to the east between the time of the explosion and now; and a wind from the Galactic center. Each of these scenarios matches some features of Sgr A East but either conflicts with others or requires extreme physical conditions (even considering that Sgr A East exists in an exotic environment). Mezger et al. (1989) mentioned one additional possible scenario—a supernova explosion within the wind bubble of the stars in the Central cluster—but did not count it as one of their four primary formation scenarios, probably because evidence for the existence of massive stars (and their accompanying winds) was just beginning to appear at the time the paper was published.

Baganoff et al. (2003) report that the *Chandra*/ACIS-I 0.5–7 keV image of the inner $17' \times 17'$ region of the galaxy contains remarkable structure; its detail is sufficient to allow comparisons with features seen in the radio and IR wavebands. The

observed diffuse X-ray emission is strongest in the center of Sgr A East. Based on these X-ray observations, Maeda et al. (2002) conclude that Sgr A East is a rare type of metal-rich, “mixed-morphology” SNR that was produced by the Type II explosion of a 13–20 M_{\odot} progenitor. The X-ray emission from Sgr A East appears to be concentrated within the central 2–3 pc of the 6×9 pc radio shell and is offset by about 2 pc from Sgr A* itself. The thermal plasma at the center of Sgr A East has a temperature $kT \approx 2$ keV, and appears to have strongly enhanced metal abundances with elemental stratification.

1.2 Research Objectives

The work presented in the following chapters attempts to answer a set of questions about the nature and interactions of these components at the Galactic center. The primary tool used for these studies is a version of SNSPH, a three-dimensional smoothed particle hydrodynamics (SPH) code; it is described in more detail in Appendix A. The Galactic center is a hydrodynamic environment, and application of the basic equations of hydrodynamics should allow us to explain many observed phenomena.

Chapters 2 and 3 investigate the origin of the diffuse X-ray emission observed within the Arches, Quintuplet, and Central star clusters. We present the hypothesis that this diffuse X-ray emission is thermal bremsstrahlung produced in the hot plasma created by collisions between winds of massive stars, and we carry out SPH simulations of winds within clusters of model massive stars to test this idea. The simulations confirm that thermal bremsstrahlung from wind-wind collisions in these clusters is easily able to account for the diffuse emission observed by *Chandra*. This confirmation also allows us to validate estimates of the mass-loss rates and wind velocities of those stars.

We also investigate one consequence of the high density of massive stars near Sgr A*—specifically, the effect of supernova explosions on the Galactic center environment and on the accretion onto the central supermassive black hole. These studies and simulations are described in chapters 4 and 5. We reexamine the claim by Mezger et al. (1989) and later authors that the explosion that produced Sgr A East occurred $\sim 10^4$ years ago and required an energy of $\sim 10^{52}$ erg. We find that, given what we now know from simulations of the central parsecs of the Galaxy (see, e.g., chapter 2), the explosion that produced Sgr A East was probably a relatively standard $\sim 10^{51}$ erg Type II supernova explosion, and it occurred less than 2000 years ago.

Finally, we study the flow of matter toward Sgr A* at both large (parsec) and small (Schwarzschild radius) length scales. Observers studying high-energy emission from Sgr A* have often suggested that Sgr A* might have been more active or luminous in the past, and also suggested that the explosion that produced Sgr A East might have been responsible for such an increase in luminosity. In chapter 5, we test the claim that the explosion that produced Sgr A East was able to alter the accretion rate or angular momentum profile of matter near Sgr A*; we find that the combined outflow from the massive stars in the Central cluster effectively shields the ~ 0.1 pc region around Sgr A*, and the passage of the shock from the explosion does not significantly alter the mass accretion rate or angular momentum profile near the black hole. In chapter 6, we study the evolution of realistic accretion disks around Sgr A* and test the hypothesis that these disks should resist the influence of general-relativistic warping effects (the Bardeen-Petterson effect); we find that thick accretion disks with properties supported by recent observations do precess coherently, without warping, around the black hole.

CHAPTER 2

DIFFUSE X-RAYS FROM THE INNER 3 PARSECS OF THE GALAXY

2.1 Introduction

The inner few parsecs of the Galaxy contain several observed components that coexist within the central deep gravitational potential well. The point-like, nonthermal radio source Sgr A* appears to be the radiative manifestation of a ~ 3 million M_{\odot} concentration of dark matter within ~ 0.015 pc of the nucleus. This concentration, probably a central black hole, is surrounded by a cluster of evolved and young stars, a molecular dusty ring, ionized gas streamers, diffuse hot gas and Sgr A East, a shell-like, nonthermal radio source believed to be the remnant (SNR) of a supernova explosion at the center of the Galaxy some 2,000 years ago (see Melia & Falcke, 2001, and chapters 4 and 5).

Observations at infrared and, particularly, radio wavelengths have been very effective in unraveling the complex behavior of the central components through their mutual interactions. But only through recent observations with the *Chandra* X-ray Observatory have we been able to study the X-ray emission from Sgr A* and its surroundings with sub-arcsecond resolution and a broad X-ray band imaging detector. These capabilities have provided us with the means to discriminate point sources, such as Sgr A*, from the diffuse emission due to hot plasma in the ambient medium.

Baganoff et al. (2003) report that the *Chandra*/ACIS-I 0.5–7 keV image of the inner $17' \times 17'$ region of the galaxy contains remarkable structure; its detail is sufficient to allow comparisons with features seen in the radio and IR wavebands. The

diffuse X-ray emission is strongest in the center of Sgr A East. Based on these X-ray observations, Maeda et al. (2002) conclude that Sgr A East is a rare type of metal-rich, “mixed-morphology” SNR that was produced by the Type II explosion of a 13–20 M_{\odot} progenitor. The X-ray emission from Sgr A East appears to be concentrated within the central 2–3 pc of the 6×9 pc radio shell and is offset by about 2 pc from Sgr A* itself. The thermal plasma at the center of Sgr A East has a temperature $kT \approx 2$ keV, and appears to have strongly enhanced metal abundances with elemental stratification.

However, this is not the sole component of hot gas surrounding Sgr A*. *Chandra* has also detected X-ray emission extending perpendicular to the Galactic plane in both directions through the position of Sgr A*, which would seem to indicate the presence of a hot, “bipolar” outflow from the nucleus. And an additional component of X-ray emitting gas appears to have been found within the molecular ring, much closer to Sgr A*. Indeed, the western boundary of the brightest diffuse X-ray emission within 2 pc of the Galactic center coincides very tightly with the shape of the Western Arc of the thermal radio source Sgr A West. Given that the Western Arc is believed to be the ionized inner edge of the molecular ring, this coincident morphology suggests that the brightest X-ray emitting plasma is being confined by the western side of the gaseous torus. In contrast, the emission continues rather smoothly into the heart of Sgr A East toward the eastern side.

A detailed fit of the emission from the hot gas within $10''$ of Sgr A* shows that it is clearly not an extension of the X-ray emitting plasma at the center of Sgr A East. The inferred 2–10 keV flux and luminosity of the local diffuse emission are $(1.9 \pm 0.1) \times 10^{-15}$ ergs cm^{-2} s^{-1} arcsec^{-2} and $(7.6_{-1.9}^{+2.6}) \times 10^{31}$ ergs s^{-1} arcsec^{-2} , respectively. Based on the parameters of the best-fit model, it is estimated that the local, hot diffuse plasma has a RMS electron density $\langle n_e^2 \rangle^{1/2} \approx 26$ cm^{-3} . Assuming

that this plasma has a filling factor of unity and is fully ionized with twice solar abundances, its total inferred mass is $M_{\text{local}} \approx 0.1 M_{\odot}$. The local plasma around Sgr A* appears to be distinctly cooler than the Sgr A East gas, with a temperature $kT = 1.3_{-0.1}^{+0.2}$ keV. By comparison, the best-fit model for Sgr A East indicates that the plasma there has about 4 times solar abundances, and twice this temperature (see above).

At least some of this local, hot plasma must be injected into the ISM via stellar winds. There is ample observational evidence in this region for the existence of rather strong outflows in and around the nucleus. Measurements of high velocities associated with IR sources in Sgr A West (Krabbe et al., 1991) and in IRS 16 (Geballe et al., 1991), the H_2 emission in the molecular ring and from molecular gas being shocked by a nuclear mass outflow (Gatley et al., 1986; but see Jackson et al., 1993 for the potential importance of UV photodissociation in promoting this H_2 emission), broad Br α , Br γ and He I emission lines from the vicinity of IRS 16 (Hall et al., 1982; Allen et al., 1990; Geballe et al., 1991), and radio continuum observations of IRS 7 (Yusef-Zadeh & Melia, 1991), provide clear evidence of a hypersonic wind, with a velocity $v_w \sim 500\text{--}1,000$ km s $^{-1}$, a number density $n_w \sim 10^{3-4}$ cm $^{-3}$, and a total mass loss rate $\dot{M}_w \sim 3\text{--}4 \times 10^{-3} M_{\odot}$ yr $^{-1}$, pervading the inner parsec of the Galaxy.

Chevalier (1992) discussed the properties of stellar winds in the Galactic center and their ability to produce X-rays, under the assumption that the colliding winds create a uniform medium with a correspondingly uniform mass and power input within the central 0.8 pc of the Galaxy. While the assumption of uniformity may be an over-simplification, steady-state models yield central conditions similar to those calculated in our simulations and (apparently) observed in nature.

The possibility that wind-wind collisions in the dense central cluster of stars

might produce an observable X-ray signature was considered more recently in the context of transient phenomena by Ozeroy et al. (1997). These authors argued that the strong winds from OB stars or WR stars would produce shocks that heat the gas up to a temperature $T \sim 10^7$ K. Instabilities in the overall outflow could therefore produce transient high temperature regions, in which the X-ray luminosity could be as high as 10^{33} – 10^{35} ergs s $^{-1}$.

A preliminary, low-resolution 3-dimensional hydrodynamical simulation by Melia & Coker (1999) subsequently revealed that although the tessellated pattern of wind-wind collision shocks can shift on a local dynamical time scale, the overall concentration of shocks in the central region remains rather steady. This is hardly surprising, given that 25 or so dominant wind sources are distributed rather evenly about the center.

In this chapter, we study in detail the emission characteristics of shocked gas produced in wind-wind collisions within 3 parsecs of Sgr A*. We present the results of comprehensive, high-resolution numerical simulations of the wind-wind interactions, using the latest suite of stellar wind sources with their currently inferred wind velocities and outflow rates. We use their projected positions and vary the radial coordinates to determine the effect of this uncertainty on the X-ray emissivity. In addition, it is clear now from the *Chandra* image that the stellar winds are also interacting directly with the molecular ring, and so we incorporate the latter into the set of boundary conditions for our simulations. The predicted X-ray luminosity and spatial profile may then be compared with the *Chandra* data. We describe our numerical technique, including the description of this molecular ring and the characteristics of the wind sources in § 2.2 of this chapter. In § 2.3 we present our results, and discuss their implications for the conditions in the Galactic center in § 2.4.

2.2 The Physical Setup

Our calculations use the 3-dimensional smoothed particle hydrodynamics (SPH) code discussed in Fryer & Warren (2002), and Fryer et al. (2006a). The Lagrangian nature of SPH allows us to concentrate spatial resolution near shocks and capture the complex time-dependent structure of the shocks in the Galactic center.

We assume that the gas behaves as an ideal gas, using a gamma-law ($\gamma = 5/3$) equation of state. Since the mass of gas in the simulation at any time is many orders of magnitude less than the mass of the black hole and its halo of stars, we calculate gravitational effects using only the gravitational potential of the assumed central $2.6 \times 10^6 M_\odot$ point mass.

Each of our two calculations uses slightly different initial conditions; details of each calculation are summarized in Table 2.1. The initial conditions for each simulation assume that the Galactic center has been cleared of all mass (perhaps by the supernova explosion that produced Sgr A East). Massive stars then inject mass into the volume of solution via winds, gradually increasing the mass of gas in the Galactic center. The number of particles in each simulation initially grows rapidly, but reaches a steady state (~ 7 million particles) when the addition of particles from wind sources is compensated by the particle loss as particles flow out of the computational domain or onto the central black hole. The particle masses vary from $9.4 \times 10^{-7} M_\odot$ to $1.0 \times 10^{-5} M_\odot$.

In addition, we place a torus of molecular material in a circumnuclear disk surrounding the inner 1.2 pc of the Galaxy. The boundary conditions (outer and central black hole), the circumnuclear disk, and the stellar wind sources are the only modifications made to the basic SPH code of Fryer et al. (2006a) to run these simulations, and we discuss these modifications in more detail in the next three subsections.

Table 2.1. Galactic Center wind simulation properties

Simulation	z positions	$10''$ L (ergs s ⁻¹ arcsec ⁻²)	T_{mass} (keV)	T_{lum} (keV)
S1	z_1	6.45×10^{31}	1.72	0.25
S2	z_2	7.50×10^{31}	1.76	0.25

2.2.1 Boundary Conditions

The boundary conditions are the major particle sinks in the simulation. We assume that once these particles have achieved escape velocity beyond a certain distance, nothing confines the material flowing out of the Galactic center. The computational domain is a cube approximately 6 pc on a side, centered on the black hole. To simulate “flow-out” conditions, particles passing through this outer boundary are removed from the calculation.

In addition, particles passing through an inner spherical boundary with a radius of 1.9×10^{17} cm (equivalent to $2.5 \times 10^5 R_s$ or ~ 0.7 Bondi-Hoyle capture radii for Sgr A*) centered on the black hole are also removed. This assumes that the accretion onto Sgr A* continues roughly at free-fall below this point. Such a simplified assumption only provides a limit on the X-ray luminosity of the point-source of Sgr A*, but it does not affect the diffuse X-ray emission in the Galactic center that is the central topic of this chapter.

2.2.2 Circumnuclear Disk

HCN synthesis data, taken at $5'' - 10''$ spatial and 4 km s^{-1} spectral resolution, reveal a highly inclined, clumpy ring of molecular gas surrounding the ionized central ~ 2

pc of the Galaxy (Güsten et al., 1987). This ring seems to be the inner edge of a thin molecular structure extending out to $\sim 5 - 7$ pc from the center. Within this cavity, and orbiting about Sgr A*, is the huge H II region known as Sgr A West comprised of a 3-armed mini-spiral (Lo & Claussen, 1983; Lacy et al., 1991). The molecular and ionized gas in the central cavity appear to be coupled, at least along the so-called western arc (one of the spiral arms), which appears to be the ionized inner surface of the molecular ring. It has been suggested that the northern and eastern arms may be streamers of ionized gas falling toward Sgr A* from other portions of the molecular ring (see Melia & Falcke, 2001, and references cited therein).

Since 1987, observations of various tracers of molecular gas (notably H_2 , CO, CS, O I, HCN, NH_3) have somewhat refined our view of the circumnuclear disk (or CND, as it is sometimes called), leaving us with the following set of defining characteristics: a total mass of $\sim 3 \times 10^4 M_\odot$, a very clumpy distribution with an estimated volume filling factor of ~ 0.01 , a typical clump mass of $\sim 30 M_\odot$, size ~ 0.1 pc, and temperature ~ 100 K (see Gatley et al., 1986; Serabyn et al., 1986; Güsten et al., 1987; DePoy et al., 1989; Sutton et al., 1990; Jackson et al., 1993; Marr et al., 1993). As many as 500 clumps fill its overall structure. Its height at the inner edge is ~ 0.5 pc, and it flares outward with distance from the center.

The *Chandra* 0.5 – 7 keV image of the central $1.3' \times 1.5'$ region of the Galaxy (see Fig. 4 in Baganoff et al., 2003), overlaid on the VLA 6-cm contours of Sgr A* and Sgr A West, shows that the western boundary of the brightest diffuse X-ray emission coincides very closely with the shape of the western arc, adding credence to the notion that the latter tracks the inner edge of the CND if one adopts the view that the X-ray glowing plasma is itself being confined by the western side of the molecular ring.

The CND therefore appears to be an essential element in the (partial) confine-

ment of the hot gas, and we incorporate it into our simulations using a simple approach that nonetheless retains the CND’s important features. To keep the volume of solution tractable, we do not model the entire ~ 14 -pc disk, but rather introduce an azimuthally-symmetric torus with inner radius 1.2 pc (see Güsten et al., 1987) and thickness 1 pc. The latter is a fair representation of the CND’s observed height at this radius. This structure does not, of course, account for the CND’s outer regions, but as we shall see, the hot, X-ray emitting gas does not penetrate far into the molecular boundary, so the outer CND is not directly relevant to this simulation. We assume that this torus has a mass of $\sim 10^4 M_\odot$, and is composed of 200 spherical clumps, each of mass $50 M_\odot$. We also incline it by 60° from the plane of the sky, orienting its principal axis (in projection) along the Galactic plane.

2.2.3 Wind Sources

It is well known by now that the Galactic center wind is unlikely to be uniform, since many stars contribute to the mass ejection (see, e.g., Melia & Coker, 1999). For these calculations, we assume that the early-type stars enclosed (in projection) within the Western Arc, the Northern Arm, and the Bar produce the observed wind. Thus far, 25 such stars have been identified (Genzel et al., 1996), though the stellar wind characteristics of only 8 have been determined from their He I line emission (Najarro et al., 1997). Figure 2.1 shows the positions (relative to Sgr A*; $1'' \approx 0.04$ pc at the Galactic center) of these wind sources; the size of the circle marking each position corresponds to the relative mass loss rate (on a linear scale) for that star. IRS 13E1 and IRS 7W seem to dominate the mass outflow with their high wind velocity ($\sim 1,000$ km s $^{-1}$) and a mass loss rate of more than $2 \times 10^{-4} M_\odot$ yr $^{-1}$ each.

Wind sources are modeled as literal sources of SPH particles. New particles are added in shells around each wind source as the simulation progresses and the

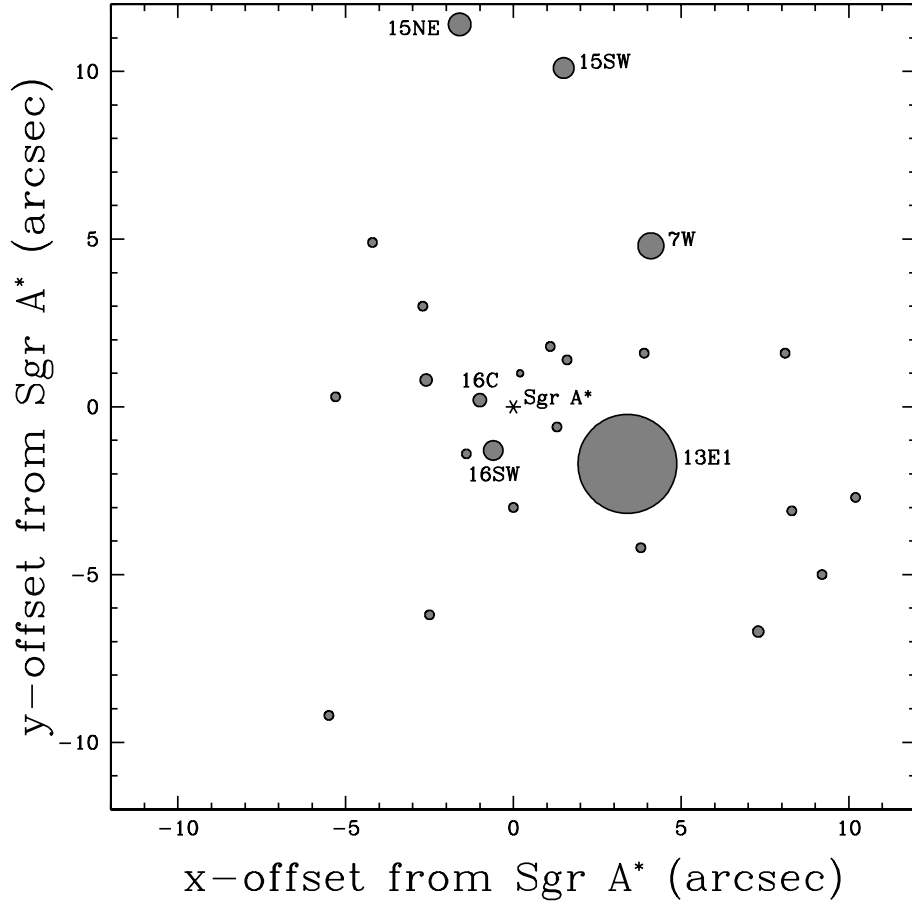


Figure 2.1 Locations of Galactic Center wind sources. Locations of the 25 wind-producing stars used in the simulations reported here, relative to the position of Sgr A* indicated by the * symbol. The radius of each circle corresponds (on a linear scale) to that star's mass loss rate. Setting the scale is 13E1, with $\dot{M} = 7.9 \times 10^{-4} M_{\odot} \text{ yr}^{-1}$.

existing particles move outward from each source. Using wind velocities inferred from observations (Najarro et al., 1997), shells around each wind source are added at a rate such that the spacing between shells is approximately equal to the spacing between particles within each incoming shell. Masses of the incoming particles are chosen to match the inferred mass loss rate for each source. The stars without any observed He I line emission are assigned a wind velocity of 750 km s^{-1} and an equal mass loss rate chosen such that the total mass ejected by the stars used here is equal to $3 \times 10^{-3} M_{\odot} \text{ yr}^{-1}$, the overall mass outflow inferred for the Galactic center region (see, e.g. Melia, 1994). The initial temperature of the stellar winds is not well known; for simplicity, we assume here that all the winds are Mach 30 at their point of ejection from the stellar surface. This corresponds to a gas temperature of $\sim 10^4 \text{ K}$. We note, however, that our results are insensitive to this value, since the temperature of the shocked gas is set primarily by the kinetic energy flux carried into the collision by the winds. For the calculations reported here, the sources are assumed to be stationary over the duration of the simulation.

An additional uncertainty is the location in z (i.e., along the line of sight) of the wind sources. To test the sensitivity of our results to the choice of z , we carry out two simulations with different coordinate assignments, and compare the overall shocked gas configurations and their X-ray emissivities. For the first choice of z positions—listed as z_1 in Table 2.2 and used in Simulation 1—we determine this third spatial coordinate randomly, subject to the condition that the overall distribution in this direction matches that in x and y . With this proviso, all these early-type stars are located within the central few parsecs surrounding Sgr A*. For the second choice of positions—listed as z_2 and used in Simulation 2—we attempt to calculate a reasonable upper limit on the luminosity produced in the central parsec by moving all the sources closer together in z , toward the $z = 0$ plane.

Table 2.2. Parameters for Galactic Center wind sources

Star	x^a	y^a	z_1^a	z_2^a	v^b	\dot{M}^c
IRS 16NE	-2.6	0.8	2.2	6.8	550	9.5
IRS 16NW	0.2	1.0	-8.3	-5.5	750	5.3
IRS 16C	-1.0	0.2	4.5	2.1	650	10.5
IRS 16SW	-0.6	-1.3	-2.5	-1.2	650	15.5
IRS 13E1	3.4	-1.7	-0.3	1.3	1,000	79.1
IRS 7W	4.1	4.8	-5.5	-2.8	1,000	20.7
AF	7.3	-6.7	6.2	-1.2	700	8.7
IRS 15SW	1.5	10.1	8.7	0.3	700	16.5
IRS 15NE	-1.6	11.4	0.7	-1.1	750	18.0
IRS 29N ^d	1.6	1.4	8.3	3.2	750	7.3
IRS 33E ^d	0.0	-3.0	0.6	6.0	750	7.3
IRS 34W ^d	3.9	1.6	4.0	-4.8	750	7.3
IRS 1W ^d	-5.3	0.3	-0.2	-4.5	750	7.3
IRS 9NW ^d	-2.5	-6.2	-3.5	-4.1	750	7.3
IRS 6W ^d	8.1	1.6	3.1	-0.4	750	7.3
AF NW ^d	8.3	-3.1	-0.1	-2.4	750	7.3
BLUM ^d	9.2	-5.0	-4.1	0.2	750	7.3
IRS 9S ^d	-5.5	-9.2	-5.9	-0.3	750	7.3
Unnamed 1 ^d	1.3	-0.6	-5.4	5.5	750	7.3
IRS 16SE ^d	-1.4	-1.4	-8.1	-5.7	750	7.3

Table 2.2—Continued

Star	x^a	y^a	z_1^a	z_2^a	v^b	\dot{M}^c
IRS 29NE ^d	1.1	1.8	3.1	-3.1	750	7.3
IRS 7SE ^d	-2.7	3.0	2.3	-5.4	750	7.3
Unnamed 2 ^d	3.8	-4.2	-8.5	4.5	750	7.3
IRS 7E ^d	-4.2	4.9	8.6	1.3	750	7.3
AF NWW ^d	10.2	-2.7	-1.9	3.9	750	7.3

^aIn arcsecs, relative to Sgr A* in l-b coordinates where +x is west and +y is north of Sgr A*

^bIn km s^{-1}

^cIn $M_{\odot} \text{ yr}^{-1}$

^dWind velocity and mass loss rate set to 750 km s^{-1} and $7.3 \times 10^{-5} M_{\odot} \text{ yr}^{-1}$, respectively (see text)

2.3 The Gas Profile and Spectrum

Wind-wind collisions in the central parsec of the Galaxy create a complex configuration of shocks that efficiently converts the kinetic energy of the winds into internal energy of the gas. Figure 2.2 shows isosurfaces of specific internal energy in the central cubic parsec of Simulation 1, $\sim 10,000$ years after the beginning of the calculation. The blue surfaces indicate regions of gas with low specific internal energy, which lie near the wind sources; the red surfaces mark regions of high specific internal energy, where gas has passed through multiple shocks. 26% of the total energy in the central parsec has been converted to internal energy via multiple shocks: the

total kinetic energy of material in the central parsec is 7.7×10^{48} ergs, while the total internal energy is 2.7×10^{48} ergs.

In order to calculate the observed continuum spectrum, we assume that the observer is positioned along the negative z -axis at infinity and we sum the emission from all of the winds—and their shocks—produced by the 25 stars in Table 2.2. For the conditions we encounter here, scattering is negligible and the optical depth is always less than unity. For these temperatures and densities, the dominant components of the continuum emissivity are electron-ion (ϵ_{ei}) and electron-electron (ϵ_{ee}) bremsstrahlung.

Figures 2.3 and 2.4 show the 2–10 keV luminosity per arcsec² from the central 10'' of Simulations 1 and 2, respectively, versus time since the beginning of each calculation. The winds fill the volume of solution after ~ 4000 years, which coincides with the point in each figure where the luminosity stops rising rapidly and begins varying by only $\sim 5\%$ around a steady value. The inset plot in each figure shows variation of the luminosity on a timescale of ~ 10 years. Data points in the insets are plotted for each of 990 time steps, where the size of each time step is 0.16 years. Variation between consecutive data points is due primarily to numerical noise, but variations on timescales of several years indicate noticeable changes in the temperature and density of the gas in the central 10''.

The range of values of the average luminosity per arcsec² measured in the central 10'' of our simulations illustrates the sensitivity of the luminosity to the positions of the wind sources. Luminosities for each of our simulations are reported in Table 2.1; for comparison, Baganoff et al. reported a 2–10 keV luminosity of $(7.6^{+2.6}_{-1.9}) \times 10^{31}$ ergs s⁻¹ arcsec⁻² from the local diffuse emission within 10'' of Sgr A*. Results from both simulations fall within the error bars reported by Baganoff et al.

Table 2.1 also includes two estimates for the temperature of the plasma within

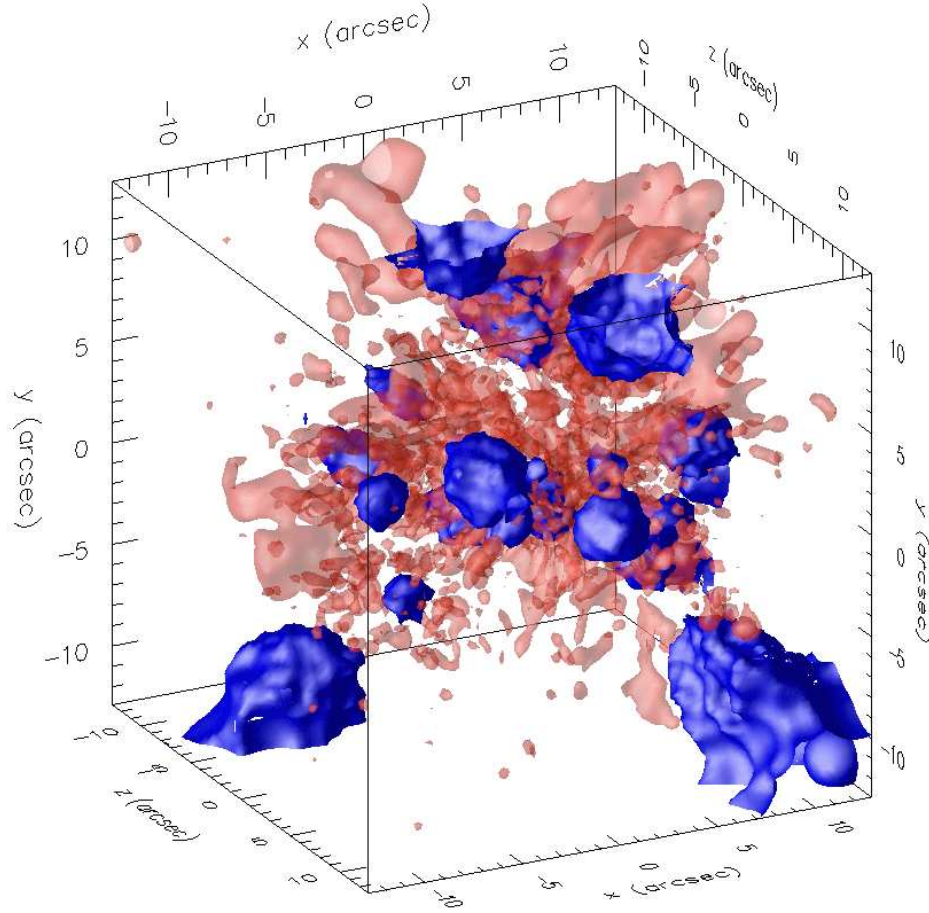


Figure 2.2 Isosurfaces of specific internal energy. Isosurfaces of specific internal energy from Simulation 1, 10,000 years after the winds were turned on. The blue surfaces correspond to a specific internal energy of 2.5×10^{12} ergs g^{-1} ; the red surfaces correspond to 3.8×10^{15} ergs g^{-1} .

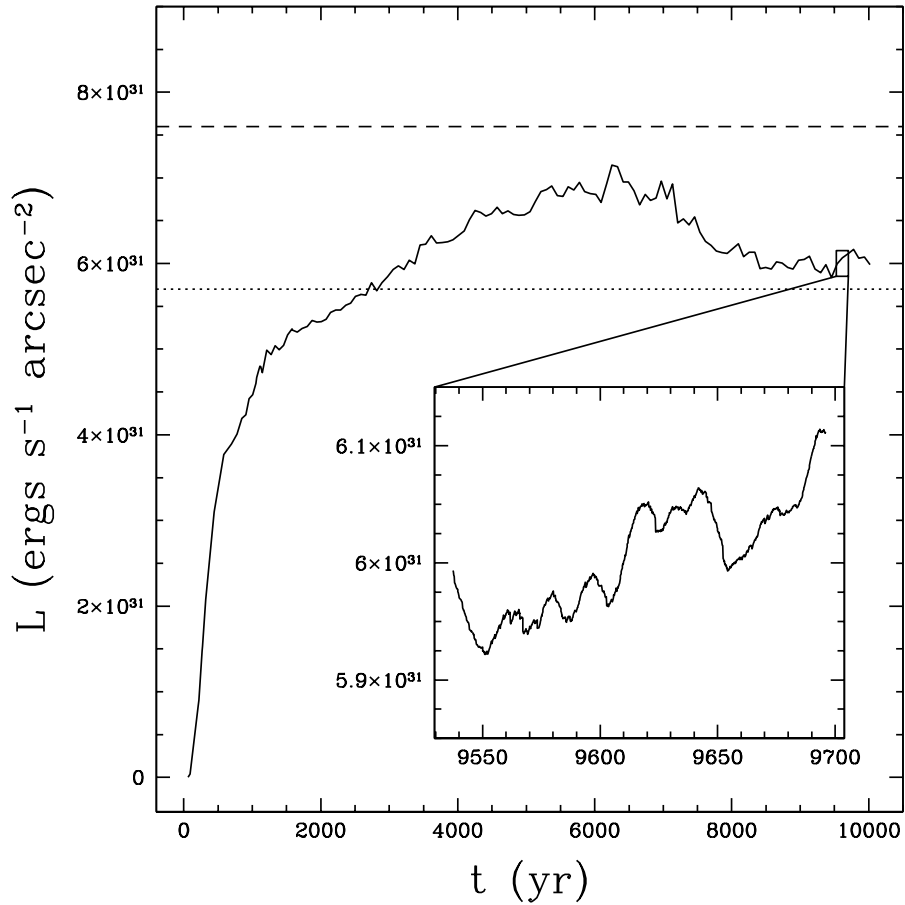


Figure 2.3 X-ray luminosity from Simulation 1. The 2–10 keV X-ray luminosity per arcsec² from the central 10'' versus time for Simulation 1. The large plot shows the variation in luminosity over the entire calculation, while the inset plot shows variation on a timescale of ~ 10 years. The winds fill the volume of solution after ~ 4000 years. The dashed line indicates the luminosity measured by *Chandra*, while the dotted line indicates the value of the lower error bar on that measurement. The upper error bar, at 1.02×10^{32} ergs s⁻¹ arcsec⁻², is not visible on this graph.

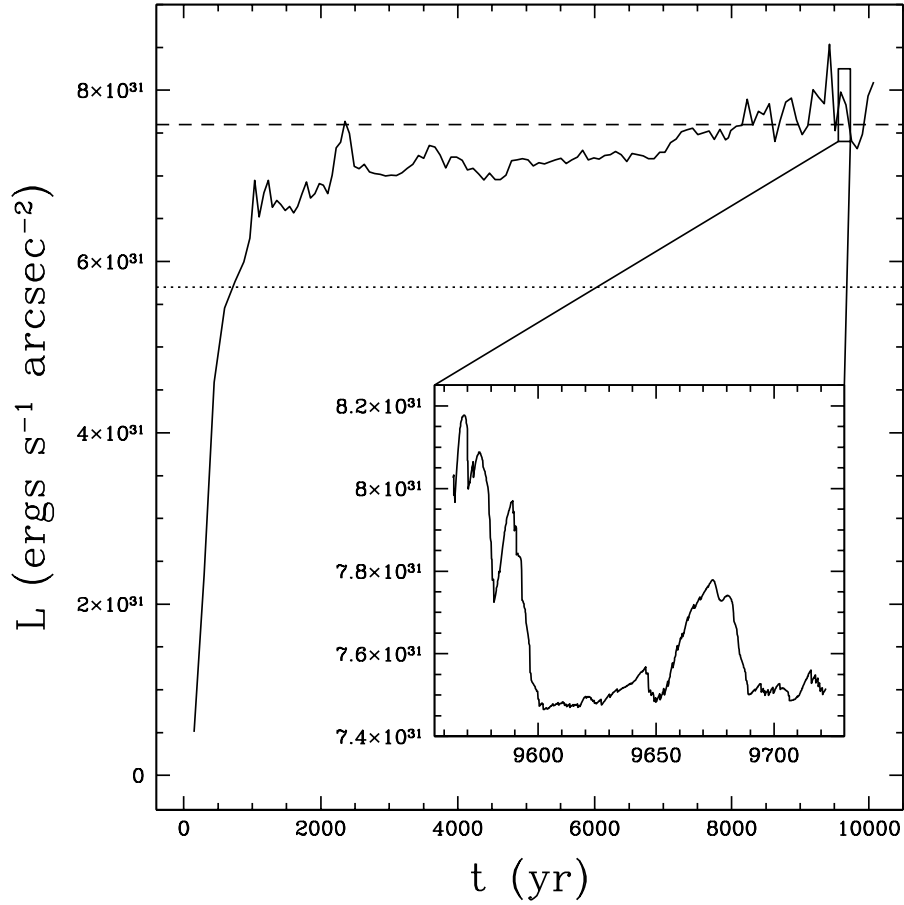


Figure 2.4 X-ray luminosity from Simulation 2. The 2–10 keV X-ray luminosity per arcsec² from the central 10'' versus time for Simulation 2. The large plot shows the variation in luminosity over the entire calculation, while the inset plot shows variation on a timescale of ~ 10 years. The winds fill the volume of solution after ~ 4000 years. The dashed line indicates the luminosity measured by *Chandra*, while the dotted line indicates the value of the lower error bar on that measurement. The upper error bar, at 1.02×10^{32} ergs s⁻¹ arcsec⁻², is not visible on this graph.

$10''$ of Sgr A*. T_{mass} is an average temperature calculated using the mass of each particle as a weighting factor, while T_{lum} uses the luminosity of each particle as a weighting factor. Since the temperature is determined primarily by the kinetic energy flux initially carried by the winds, and since the initial wind velocities in each calculation are the same, the average temperature for the plasma at the center of each calculation is essentially the same.

The average luminosity per volume as a function of radius from the center of Simulation 1 is shown in figure 2.5; the average luminosity-weighted temperature as a function of radius from the same simulation is shown in figure 2.6. The majority (77% of the overall 2–10 keV luminosity) of the 2–10 keV emission comes from the central 0.4 pc, where it is produced in wind-wind collisions. There is also noticeable emission (2.5% of the overall luminosity) from a high-temperature region centered on 1.2 pc, which is the location of the inner edge of the CND; emission here is produced when winds collide with the clumps in our model torus.

Figures 2.7 and 2.8 show contours of 2–10 keV luminosity per arcsec² from Simulations 1 and 2, respectively, 10,000 years after the winds were turned on. The dotted circle overlaid on each figure shows the size of the $10''$ central region. The zones of relatively high luminosity at the north-east and south-west corners of each figure, and along the northwest side of the Simulation 2 contours, result from collisions of the outflowing wind with the inner edge of the CND.

The gas distribution in a multiple-wind source environment like that modeled here is distinctly different from that of a uniform flow past a central accretor (Coker & Melia, 1997). Unlike the latter, the former does not produce a large-scale bow shock, and therefore the environmental impact of the gravitational focusing by the central dark mass has significantly less order in this case. We shall defer a more extensive discussion of this point to a later publication, in which we report the

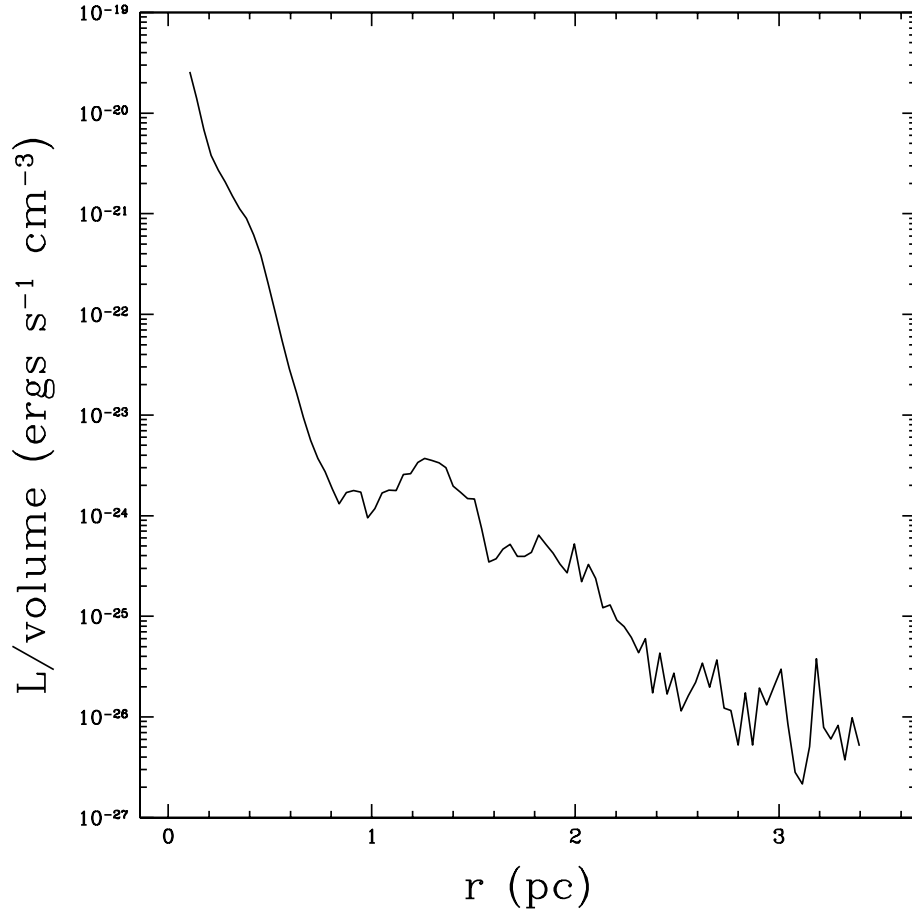


Figure 2.5 X-ray luminosity radial profile. The 2–10 keV X-ray luminosity per volume per 0.035 pc radial bin versus distance from the central black hole in Simulation 1. Collisions between the winds and the inner edge of the CND are visible as a bump near 1.2 pc.

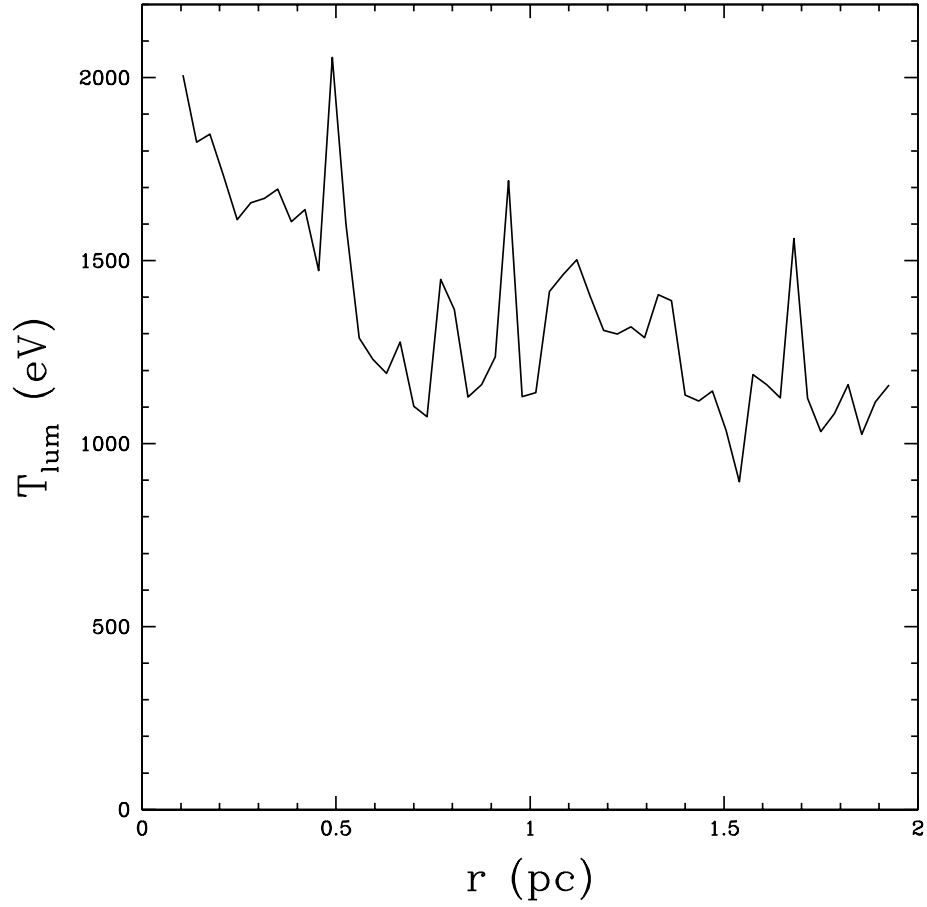


Figure 2.6 Temperature radial profile. Average luminosity-weighted temperature per 0.035 pc radial bin versus distance from the central black hole in Simulation 1. Collisions between the winds and the inner edge of the CND are visible as a spike near 1 pc.

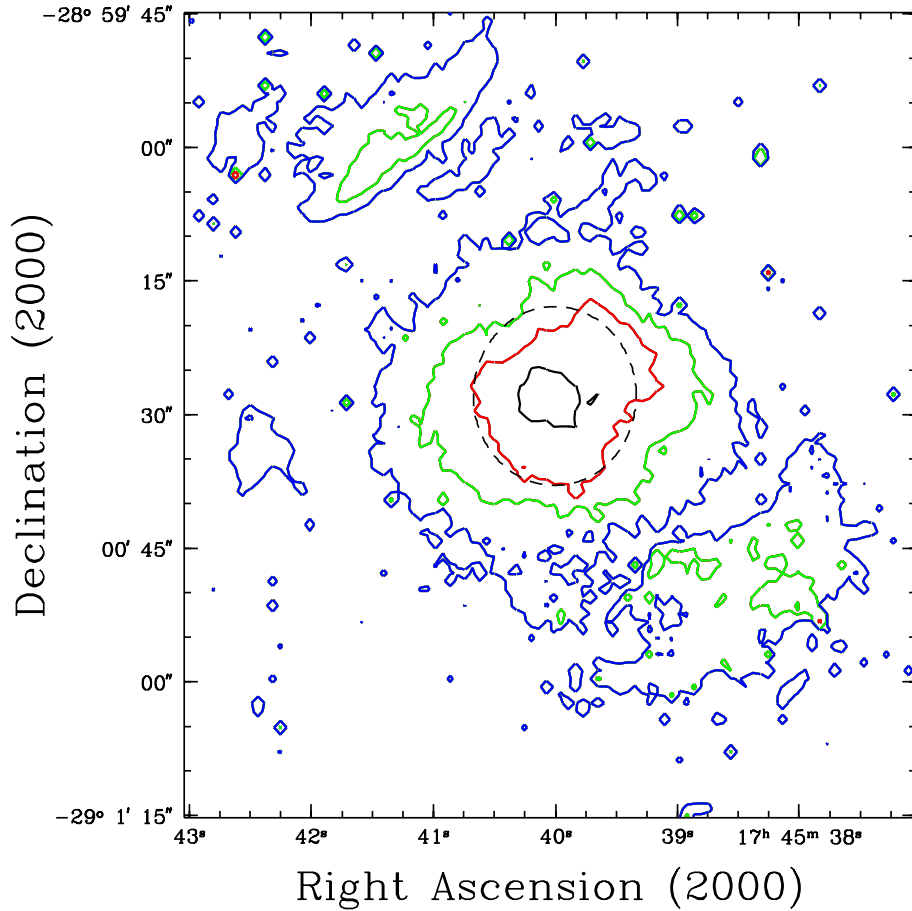


Figure 2.7 X-ray luminosity contours from Simulation 1. Contours of column-integrated 2–10 keV X-ray luminosity per simulated pixel from Simulation 1. There are 100 pixels along each axis; each pixel is $0.9''$ by $0.9''$. In order from black to red to green to blue, the luminosities indicated by the contours are 10^{32} ergs s^{-1} per pixel, 10^{31} ergs s^{-1} per pixel, 10^{30} ergs s^{-1} per pixel, and 1.5×10^{29} ergs s^{-1} per pixel. The dashed circle indicates the extent of the “local” region around Sgr A*; it has a radius of $10''$ and is centered on Sgr A*.

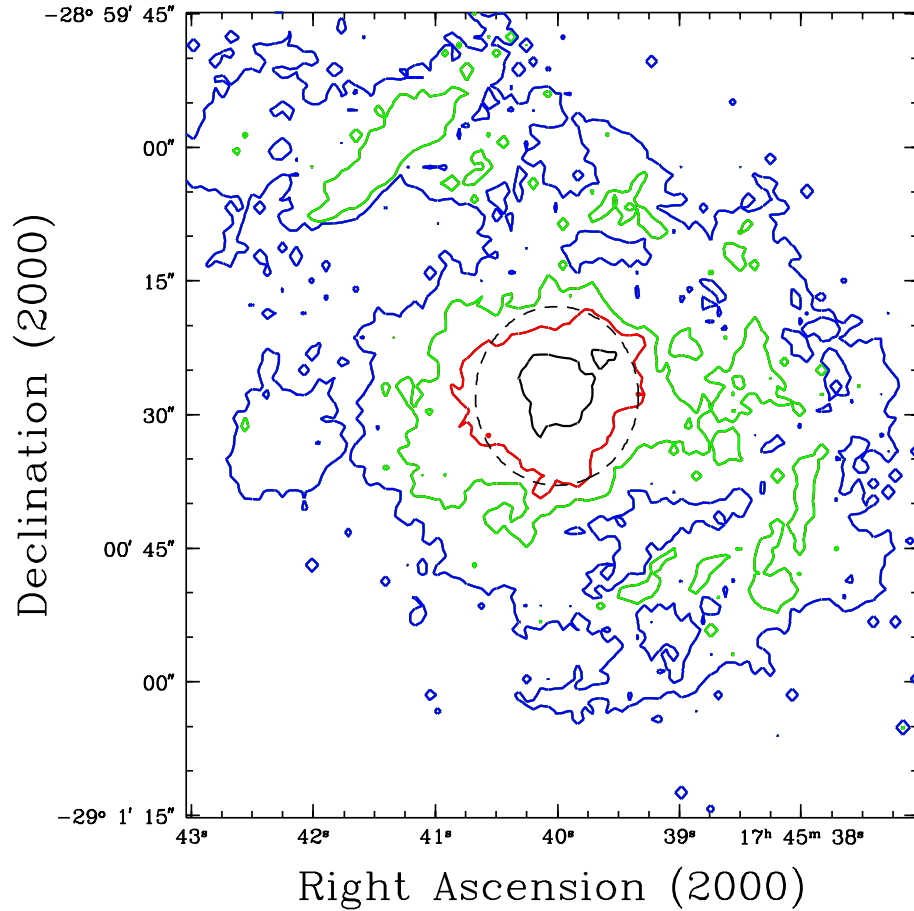


Figure 2.8 X-ray luminosity contours from Simulation 2. Contours of column-integrated 2–10 keV X-ray luminosity per simulated pixel from Simulation 2. There are 100 pixels along each axis; each pixel is $0.9''$ by $0.9''$. In order from black to red to green to blue, the luminosities indicated by the contours are 10^{32} ergs s^{-1} per pixel, 10^{31} ergs s^{-1} per pixel, 10^{30} ergs s^{-1} per pixel, and 1.5×10^{29} ergs s^{-1} per pixel. The dashed circle indicates the extent of the “local” region around Sgr A*; it has a radius of $10''$ and is centered on Sgr A*.

results of a multiple-wind source simulation for the accretion of shocked gas onto the central, massive black hole.

2.4 Discussion

Using only the latest observed stellar positions and inferred mass loss rates and wind velocities, we have produced self-consistent X-ray luminosity maps of the Galactic center. It appears that the diffuse X-ray luminosity and temperature within $10''$ of Sgr A* can be explained entirely by shocked winds; the luminosities from both of our simulations fall within the error bars associated with the diffuse 2–10 keV X-ray luminosity measured by *Chandra*. This seems rather significant in view of the fact that, were the diffuse X-rays surrounding Sgr A* being produced by another mechanism, we would need to lower the overall stellar mass-loss rate or wind velocity by a factor of 2 or more in order to render the emissivity produced by wind-wind collisions unobservable. The luminosities that we calculate are fairly insensitive to the placement of the wind sources along the line of sight to the Galactic Center; the 2–10 keV luminosity per arcsec² differs by only $\sim 15\%$ between Simulation 1—in which sources are randomly distributed in z —and Simulation 2—in which sources are compressed toward Sgr A* perpendicular to the plane of the sky.

Although the wind mass-loss rate is $3 \times 10^{-3} M_{\odot} \text{ yr}^{-1}$, the average accretion rate through our inner boundary is only $4.25 \times 10^{-4} M_{\odot} \text{ yr}^{-1}$ for Simulation 1 and $4.59 \times 10^{-4} M_{\odot} \text{ yr}^{-1}$ for Simulation 2. Even so, this is much higher than what one would expect from the X-ray emission at this inner boundary. Since we do not model this accretion, we have neglected a number of effects from magnetic fields to radiation pressure. We postpone this detailed analysis to a future work.

One possible explanation for the relatively low luminosity of Sgr A* has been that the supernova that created Sgr A East swept most of the gas out of the environment

surrounding Sgr A*. However, our calculations show that the stellar winds within 3 parsecs of the Galactic center bring the environment near the black hole back to a steady state within ~ 4000 years. In addition, the gas temperature and X-ray luminosity calculated from our results add weight to Baganoff et al.'s hypothesis that the X-ray emitting gas surrounding Sgr A* really is a different component than that at the center of Sgr A East, which has a temperature closer to 2 keV.

Collision of the wind with the inner edge of the CND may produce the western arm of the minispiral. Our simple model for the CND produces clear emission at the location of the inner edge of the molecular ring, although we do not reproduce the entire complex morphology of the X-ray emitting gas seen by *Chandra*.

The excellent agreement between our calculated X-ray luminosities and the value of the luminosity measured by *Chandra* solidifies our understanding of the gas dynamics in the Galactic center. Future calculations will move the inner boundary of the simulation inward and explore the dynamics of the shocked gas as it falls toward the central black hole.

CHAPTER 3

DIFFUSE X-RAYS FROM THE ARCHES AND QUINTUPLET CLUSTERS

3.1 Introduction

Understanding the environment's role in star formation and, in turn, the feedback exerted by star formation on the Galactic environment, is a problem of significance to several fields in astronomy, from the creation of compact objects to the formation of galaxies. The Galactic center, with its relatively high magnetic field strength, clouds with high particle density, and large velocity dispersions, provides an ideal environment to study star formation under extreme conditions (Morris, 1993; Melia & Falcke, 2001). This type of investigation can benefit from the existence of several stellar clusters in this region, including the Arches and Quintuplet clusters. Learning more about their stellar constituents, and possibly their formative history, may even give us a glimpse into the emergence of objects that will ultimately populate the central parsec of the Galaxy (e.g., Gerhard, 2001; McMillan & Portegies Zwart, 2003).

The Arches and Quintuplet clusters have been studied over a range of wavelengths, from radio to X-ray. X-rays provide a unique window for investigating both the formation of binaries (point sources from binary interactions) and the wind interactions within the entire cluster (diffuse emission). As we showed in chapter 2, the diffuse X-ray emission is a sensitive measure of the mass-loss rate of stars in mutually interactive situations. Stellar mass-loss remains one of the largest uncertainties in stellar evolution (e.g., Wellstein & Langer, 1999). X-ray observations of

these clusters represent a unique probative tool for studying the winds produced by high-metallicity systems.

In this chapter, we model the propagation and interaction of winds from stars in both the Arches and Quintuplet clusters, calculating the X-ray fluxes arising from the consequent shocked gas. Yusef-Zadeh et al. (2002) serendipitously discovered the Arches cluster with *Chandra* and identified five components of X-ray emission, which they labeled A1–A5, though only A1–A3 seem to be directly associated with the cluster (see Figure 2, Yusef-Zadeh et al., 2002). A1 is apparently associated with the core of the cluster, while A2 is located $\sim 10''$ northwest of A1. A1 and A2 are partially resolved, while A3 is a diffuse component that extends beyond the boundary of the cluster; Yusef-Zadeh et al. (2002) speculated that some or all of A1–A3 may be produced by interactions of winds from stars in the system. Analysis of additional *Chandra* observations that covered the Arches cluster and first results from the Quintuplet cluster are presented by Wang (2003) and Law & Yusef-Zadeh (2004); these new observations resolve A1 into two distinct components, labeled A1N and A1S, and indicate that A1N, A1S, and A2 are all point-like X-ray sources.

Several efforts have already been made to study the X-ray emission from clusters. Ozernoy et al. (1997) and Cantó et al. (2000) performed analytic calculations to estimate the diffuse emission from these systems. The interaction of winds in the Arches cluster has been simulated by Raga et al. (2001) using the “yguazú-a” adaptive grid code described in Raga et al. (2000). However, all previous work focused exclusively on the Arches cluster, and even the detailed simulations assumed identical large values for the mass-loss rates ($\dot{M} = 10^{-4}M_{\odot} \text{ yr}^{-1}$) and wind velocities ($v_{wind} = 1,500 \text{ km s}^{-1}$) of the constituent stars. In this chapter, we present the results of simulations of both the Arches and Quintuplet clusters, using detailed radio flux measurements (where available) and spectral classifications to pin down

the expected mass-loss rates of stars in each system. We then compare our results to the most recent X-ray observations of these two clusters, including new data presented here.

A summary of relevant properties of each cluster is presented below. We describe our numerical technique, including the characteristics of the wind sources and the gravitational potential of the clusters, in § 3.2. The new observations are described in § 3.3. A comparison of the theoretical results with the data is made in § 3.4, and the relevance to the Galactic center conditions is discussed in § 3.5.

3.1.1 The Arches Cluster

The Arches stellar cluster is an exceptionally dense aggregate of stars located at $l = 0.12^\circ$, $b = 0.02^\circ$, about $11'$ in projection from the Galactic center (see e.g. Nagata et al., 1995; Cotera et al., 1996; Figer et al., 2002). The cluster is apparently a site of recent massive star formation; it contains numerous young emission-line stars which show evidence of strong stellar winds. Using near-IR color-magnitudes and K band counts, Serabyn et al. (1998) estimated that at least 100 cluster members are O stars with masses greater than $20 M_\odot$ and calculated a total cluster mass of $\sim (1.5\text{--}6) \times 10^4 M_\odot$. Figer et al. (1999b) used *HST* NICMOS observations to determine the slope of the initial mass function (IMF) of the Arches cluster and calculated a cluster mass of $\sim 10^4 M_\odot$, with possibly 160 O stars and an average mass density of $\sim 3 \times 10^5 M_\odot \text{ pc}^{-3}$.

The 14 brightest stars of this cluster have been identified with JHK photometry and $\text{Br}\alpha$ and $\text{Br}\gamma$ hydrogen recombination lines, showing that they have the characteristic colors and emission lines of Of-type or Wolf-Rayet (WR) and He I emission-line stars. Nagata et al. (1995) inferred from the strength of the $\text{Br}\alpha$ and $\text{Br}\gamma$ line fluxes that these stars are losing mass at a prodigious rate, $\dot{M} \sim 2 \times 10^{-5} M_\odot \text{ yr}^{-1}$, in winds moving at $\sim 10^3 \text{ km s}^{-1}$. Cotera et al. (1996) confirmed the presence

of young, massive stars using K -band spectroscopy; they identified 12 stars in the cluster with spectra consistent with late-type WN/Of objects, with mass-loss rates $\dot{M} \sim (1\text{--}20) \times 10^{-5} M_{\odot} \text{ yr}^{-1}$ and wind velocities $v_{\infty} \sim 800\text{--}1,200 \text{ km s}^{-1}$.

Follow-up Very Large Array (VLA) observations at centimeter wavelengths of the brightest stars in the cluster have solidified the detection of powerful ionized stellar winds. Using the observed 8.5 GHz flux densities from 8 sources in the Arches cluster and the relationship between flux density and mass-loss rate derived by Panagia & Felli (1975),

$$\dot{M} = (5.9 \times 10^{-5} M_{\odot} \text{ yr}^{-1}) \left(\frac{S_{8.5}}{1 \text{ mJy}} \right)^{3/4} \left(\frac{v_{\infty}}{500 \text{ km s}^{-1}} \right) \left(\frac{d}{8 \text{ kpc}} \right)^{3/2}, \quad (3.1)$$

where $S_{8.5}$ is the 8.5 GHz flux density, v_{∞} is the wind terminal velocity, and d is the distance to the source ($\sim 8 \text{ kpc}$, for stars in the Arches cluster), Lang et al. (2001) calculated mass loss rates $\dot{M} = (3\text{--}17) \times 10^{-5} M_{\odot} \text{ yr}^{-1}$, assuming a wind electron temperature $T \sim 10^4 \text{ K}$, $Z = 1$, and a mean molecular weight $\mu = 2$. The Wolf-Rayet phase is short-lived, but while in this mode, stars dominate the mass ejection within the cluster.

In an attempt to represent both the identified stellar wind sources and the population of stars likely to be producing significant but currently undetected winds, we include 42 wind sources (listed in Table 3.1 and shown in Figure 3.1) in our simulations of the Arches cluster. The stars labeled AR1–AR9 correspond to the 9 radio sources identified by Lang (2002). The first 29 stars (labeled 1–29) in Table 3.1 have mass estimates greater than $60 M_{\odot}$ (Figer et al., 2002), and are likely the most powerful sources of wind in the cluster. The remaining 13 stars used in the simulations have masses less than $60 M_{\odot}$ but greater than $25 M_{\odot}$ and are located on the north side of the cluster; they are included to better represent the spatial pattern of X-ray emission around the core of the cluster. Based on the broadening of the $\text{Br}\gamma$ line observed by Cotera et al. (1996), stars in the Arches cluster simu-

lations are assigned wind velocities of $1,000 \text{ km s}^{-1}$. The stars labeled AR1–AR9, which have observed 8.5 GHz flux densities, are assigned mass-loss rates according to Equation 3.1. Stars with no associated 8.5 GHz detection but with masses larger than $60 M_{\odot}$ are assigned a mass-loss rate of $3 \times 10^{-5} M_{\odot} \text{ yr}^{-1}$, which is equal to the lowest mass-loss rate inferred from the weakest observed 8.5 GHz signal from the Arches cluster (Lang, 2002). Stars with masses less than $60 M_{\odot}$ are assigned a mass-loss rate of $3 \times 10^{-6} M_{\odot} \text{ yr}^{-1}$; their winds will have little effect on the overall luminosity but may alter the shape of the X-ray-emitting region.

Table 3.1. Parameters for the Arches Cluster wind sources

Star ^a	x ^b (arcsec)	y ^b (arcsec)	z ^c (arcsec)	v (km s ⁻¹)	\dot{M} (10 ⁻⁵ M _⊙ yr ⁻¹)
1, AR3	0.00	0.00	8.38	1,000	3.2
2	-6.75	-3.53	10.70	1,000	3.0
3, AR7	8.20	-4.13	2.66	1,000	4.2
4, AR5	4.83	4.66	2.71	1,000	3.0
5, AR8	3.29	-9.64	-5.31	1,000	3.6
6, AR1	2.87	-0.03	-1.85	1,000	17.0
7, AR4	3.53	2.73	-5.72	1,000	3.9
8, AR2	2.46	1.01	2.78	1,000	3.9
9	0.80	10.50	0.23	1,000	3.0
10	-1.83	-4.25	-0.90	1,000	3.0
11	-1.03	14.41	6.83	1,000	3.0
12	1.01	4.98	-11.46	1,000	3.0
13	-2.08	-1.39	6.12	1,000	3.0
14	6.24	-0.32	5.15	1,000	3.0
15	7.24	5.67	-14.94	1,000	3.0
16	4.22	1.59	-14.62	1,000	3.0
17	-0.89	-4.90	14.59	1,000	3.0
18, AR9	3.58	4.34	13.79	1,000	3.2
19, AR6	-5.81	-3.72	-4.97	1,000	4.5

Table 3.1—Continued

Star ^a	x ^b (arcsec)	y ^b (arcsec)	z ^c (arcsec)	v (km s ⁻¹)	\dot{M} ($10^{-5} M_{\odot} \text{ yr}^{-1}$)
20	2.90	2.58	-3.20	1,000	3.0
21	7.36	2.65	10.49	1,000	3.0
22	0.24	5.55	-8.01	1,000	3.0
23	12.50	-1.08	14.43	1,000	3.0
24	-1.42	1.55	9.62	1,000	3.0
25	-3.26	-4.30	-8.37	1,000	3.0
26	4.60	-1.27	13.43	1,000	3.0
27	5.31	2.74	4.80	1,000	3.0
28	5.77	0.55	10.79	1,000	3.0
29	7.08	4.62	11.95	1,000	3.0
36	-6.19	14.87	-8.33	1,000	3.0
37	3.54	2.99	5.89	1,000	3.0
49	-1.74	14.97	9.01	1,000	0.3
61	-1.53	23.67	2.02	1,000	0.3
75	7.42	11.51	4.86	1,000	0.3
108	7.22	11.83	7.08	1,000	0.3
111	0.65	18.90	-12.39	1,000	0.3
116	3.64	16.48	12.31	1,000	0.3
126	8.80	19.13	-0.92	1,000	0.3

Table 3.1—Continued

Star ^a	x ^b (arcsec)	y ^b (arcsec)	z ^c (arcsec)	v (km s ⁻¹)	\dot{M} (10 ⁻⁵ M _⊙ yr ⁻¹)
129	-9.61	10.04	2.44	1,000	0.3
132	7.04	20.08	6.02	1,000	0.3
149	5.54	21.20	-5.47	1,000	0.3
156	5.02	20.61	7.93	1,000	0.3

^aNumerical designations taken from Figer et al. (2002); “AR” designations taken from Lang (2002).

^bOffset from $\alpha(2000)$: 17^h 45^m 50.26^s, $\delta(2000)$: -28° 49′ 22″.76 (Figer et al., 2002). Here, positive x is ascending R.A. (to the East) and positive y is ascending declination (to the North).

^cSimulated with Monte Carlo.

3.1.2 The Quintuplet Cluster

Slightly further north of Sgr A*, the Quintuplet cluster is located at $l = 0.16^\circ$, $b = 0.06^\circ$. The cluster has a total estimated mass of $\sim 10^4 M_\odot$ and a mass density of $\sim 10^3 M_\odot \text{pc}^{-3}$ (Figer et al., 1999a). Like the objects in the Arches cluster, the known massive stars in the Quintuplet cluster have near-IR emission-line spectra indicating that they too have evolved away from the zero-age main sequence and now produce high-velocity stellar winds with terminal speeds of 500–1,000 km s⁻¹.

Figer et al. (1999a) obtained K-band spectra of 37 massive stars in the Quintuplet cluster and found that 33 could be classified as WR stars, OB supergiants, or luminous blue variables (LBVs), implying a range of wind mass-loss rates $\dot{M} \sim (0.1-$

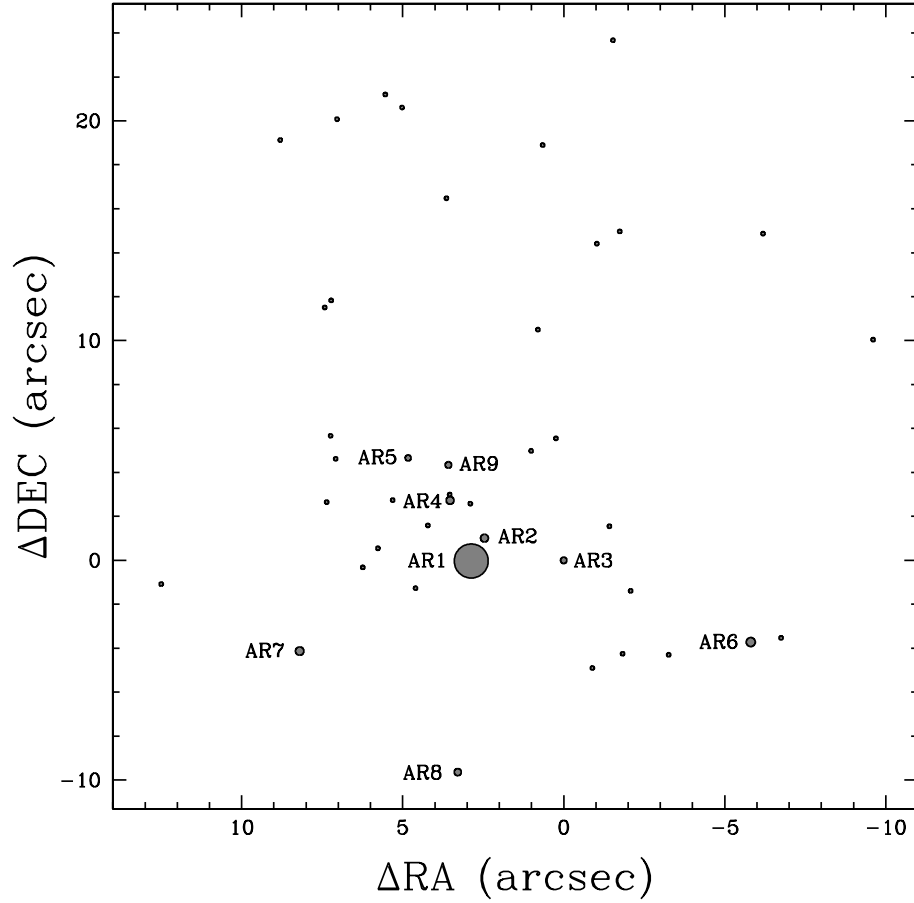


Figure 3.1 Locations of Arches cluster wind sources. Location of the 42 wind-producing stars used in the simulations of the Arches cluster, relative to $\alpha(2000)$: $17^h 45^m 50.26^s$, $\delta(2000)$: $-28^\circ 49' 22''.76$ (Figer et al., 2002). The radius of each circle corresponds (on a linear scale) to that star's mass loss rate. Setting the scale is AR1, with $\dot{M} = 1.7 \times 10^{-4} M_\odot \text{ yr}^{-1}$.

$6.6) \times 10^{-5} M_{\odot} \text{ yr}^{-1}$. VLA continuum images at 6 cm and 3.6 cm of the Sickle and Pistol H II regions reveal eight point sources located in the vicinity of the Quintuplet cluster, including the radio source at the position of the Pistol nebula (Lang et al., 1999). These are labeled QR1 through 7, and the Pistol star, in Figure 3.2 below.

The near-IR counterparts of QR4 and QR5 are hot, massive stars with high mass-loss rates, one an OB I supergiant and the other a WN9/Ofpe (Figer et al., 1999a). The sources QR1, QR2, and QR3 also have spectral indices consistent with stellar wind sources, but they have no obvious NICMOS stellar counterparts. Lang et al. (1999) speculated that this may be due to variable extinction associated with a dense molecular cloud located in front of the cluster. Given the uncertainty, and possible variation, in stellar identification for these 5 objects, we therefore adopt a value of $\sim 500 \text{ km s}^{-1}$ (typical in OB supergiants) for the speed of their wind. The Pistol star, on the other hand, is a prominent source in the near-IR NICMOS image, and is evidently a luminous blue variable (Figer et al., 1998) possessing a powerful stellar wind, though with a terminal speed of only $v_{\infty} \sim 100 \text{ km s}^{-1}$.

In our simulations of the Quintuplet cluster, we include 31 massive stars with spectral classifications identified by Figer et al. (1999a), using estimates for the wind parameters of each star according to its spectral type. Wind velocities are determined according to the broad spectral type of each star: we assume a velocity of $1,000 \text{ km s}^{-1}$ for winds from WR stars, 500 km s^{-1} winds for OB supergiants, and 100 km s^{-1} for the Pistol star, a LBV.

For those stars that are radio sources (QR1–QR3, QR6, and QR7 from Lang et al., 1999), mass-loss rates are determined according to Equation 3.1. For the rest of the stars, we estimate the mass-loss based on the spectral classifications by Figer et al. (1999a). For OB stars, the mass-loss rate was assumed to be $10^{-5} M_{\odot} \text{ yr}^{-1}$ for stars with classification higher than BO. For smaller stars, the mass-loss rate was

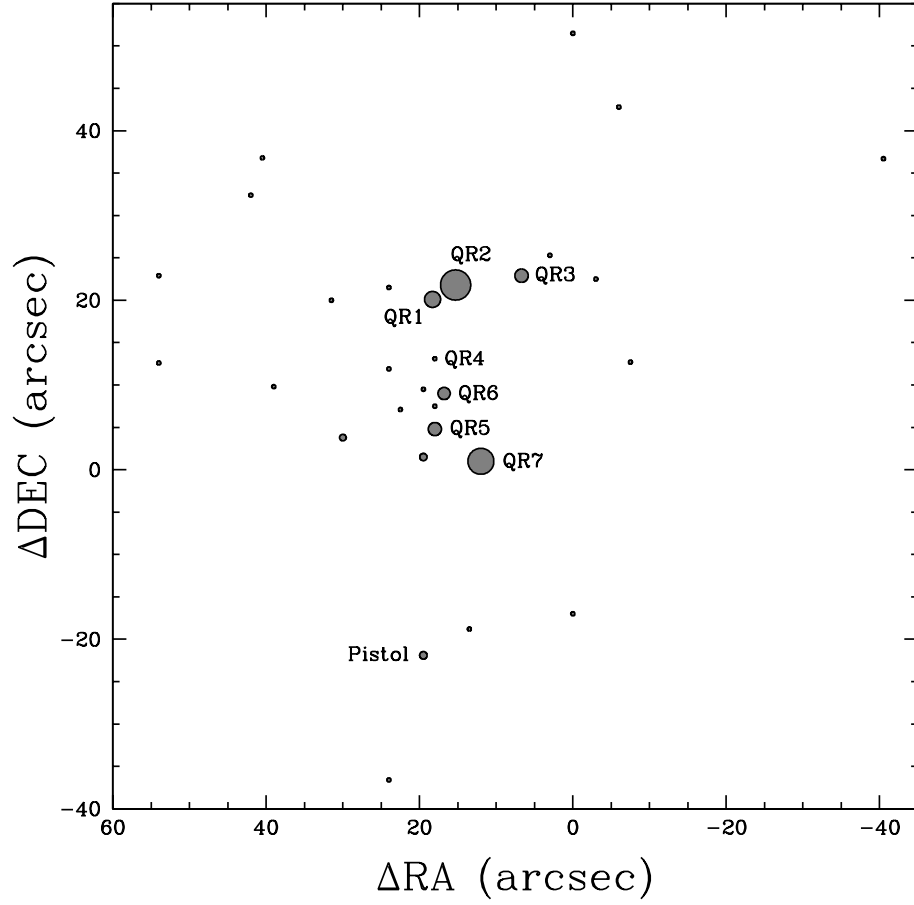


Figure 3.2 Locations of Quintuplet cluster wind sources. Location of the 31 wind-producing stars used in the simulations of the Quintuplet cluster, relative to $\alpha(1950)$: $17^h 43^m 4.5^s$, $\delta(1950)$: $-28^\circ 48' 35''$ (Lang et al., 1999). The radius of each circle corresponds (on a linear scale) to that star's mass loss rate. Setting the scale is QR2, with $\dot{M} = 1.5 \times 10^{-4} M_\odot \text{ yr}^{-1}$.

assumed to be $10^{-6} M_{\odot} \text{ yr}^{-1}$. For Wolf-Rayet stars, we use a luminosity-mediated mass-loss relation (Wellstein & Langer, 1999):

$$\log \left(\frac{-\dot{M}_{\text{WR}}}{M_{\odot} \text{ yr}^{-1}} \right) = k + 1.5 \log \left(\frac{L}{L_{\odot}} \right) - 2.85 X_s, \quad (3.2)$$

where L is the stellar luminosity from Figer et al. (1999a), X_s is the hydrogen mass fraction, and k is a constant which we calibrated using our radio-determined mass-loss rates. The locations and wind parameters of the stellar wind sources are summarized in Table 3.2, and their relative positions are shown in Figure 3.2.

Table 3.2. Parameters for the Quintuplet Cluster wind sources

Star ^a	x ^b (arcsec)	y ^b (arcsec)	z ^c (arcsec)	v (km s ⁻¹)	\dot{M} (10 ⁻⁵ M _⊙ yr ⁻¹)
QR1	-3.30	20.10	-36.41	500	8.0
QR2	-0.30	21.80	9.39	500	15.1
QR3	8.30	22.90	-42.78	500	6.7
QR6	-1.80	9.00	31.80	1,000	6.1
QR7	3.00	1.00	-26.99	1,000	13.0
76	-9.00	-36.60	-9.50	1,000	0.28
134, Pistol	-4.50	-21.90	-28.26	100	3.8
151	1.50	-18.80	-20.94	1,000	1.1
157	15.00	-17.00	8.82	500	0.16
235	-4.50	1.50	-2.91	1,000	3.7
240	-15.00	3.80	-9.06	1,000	3.3
241, QR5	-3.00	4.80	39.75	1,000	6.6
250	-7.50	7.10	48.44	500	1.0
256	-24.00	9.80	-9.66	1,000	0.70
257	-4.50	9.50	-19.34	500	1.0
269	-9.00	11.90	24.33	500	0.1
270, QR4	-3.00	13.10	-29.77	500	1.4
274	-39.00	12.60	42.80	1,000	0.67
276	22.50	12.70	-7.87	500	0.1

Table 3.2—Continued

Star ^a	x^b (arcsec)	y^b (arcsec)	z^c (arcsec)	v (km s ⁻¹)	\dot{M} (10 ⁻⁵ M_{\odot} yr ⁻¹)
278	-3.00	7.50	-36.93	500	1.0
301	-16.50	20.00	-4.93	500	0.1
307	-9.00	21.50	-41.15	500	1.0
309	-39.00	22.90	-38.32	1,000	0.26
311	18.00	22.50	34.69	500	0.1
320	12.00	25.30	-18.66	1,000	0.61
344	-27.00	32.40	4.04	500	0.1
353	55.50	36.70	-6.15	1,000	0.22
358	-25.50	36.80	-15.30	500	0.32
362	-46.50	38.40	-13.75	100	3.0
381	21.00	42.80	-22.20	500	0.40
406	15.00	51.50	-26.93	500	0.1

^aNumerical designations taken from Figer et al. (1999a); “QR” designations taken from Lang (2002).

^bOffset from $\alpha(1950)$: $17^h 43^m 4.5^s$, $\delta(1950)$: $-28^{\circ} 48' 35''$ (based on Lang et al., 1999). Here, positive x is ascending R.A. (to the East) and positive y is ascending declination (to the North).

^cSimulated with Monte Carlo.

3.2 The Physical Setup

Our calculations use the three-dimensional smoothed particle hydrodynamics (SPH) code discussed in Fryer & Warren (2002) and Fryer et al. (2006a), modified as described in chapter 2 to include stellar wind sources. The gridless Lagrangian nature of SPH allows us to concentrate spatial resolution near shocks and model gas dynamics and wind-wind interactions on length scales that vary by several orders of magnitude within a single calculation.

We assume that the gas behaves as an ideal gas, according to a gamma-law ($\gamma = 5/3$) equation of state. The effect of self-gravity on the dynamics of the gas should be negligible compared to the effect of the central cluster potential; we calculate gravitational effects by approximating the potential of each cluster with a Plummer model.

The computational domain for the simulation of each cluster is a cube approximately 6 pc on a side, centered on the middle of the cluster. To simulate “flow-out” conditions, particles passing through the outer boundary are removed from the simulation. The initial conditions assume that the space around and within each cluster is empty; massive stars in each cluster then inject matter into the volume of solution via winds as the calculation progresses. The number of particles in each simulation initially grows rapidly, but reaches a steady number (~ 6.6 million particles for simulations of the Arches cluster and ~ 3.3 million particles for the Quintuplet simulations, since there are fewer identified wind sources in the latter) when the addition of particles from wind sources is compensated by the loss of particles through the outer boundary of the computational domain.

3.2.1 Cluster Potential

We model the gravitational potential Φ of each cluster using a Plummer model (Plummer, 1911),

$$\Phi(r) = \frac{-GM}{\sqrt{r^2 + b^2}}, \quad (3.3)$$

where M is the total mass of the cluster. The radial density profile assumed for the cluster is therefore

$$\rho(r) = \rho_0 \left(1 + \frac{r^2}{b^2}\right)^{-5/2}, \quad (3.4)$$

where the central density ρ_0 is

$$\rho_0 = \frac{3M}{4\pi b^3}. \quad (3.5)$$

We note that the spatial distributions of massive stars in the clusters are not entirely consistent with the distribution implied by the Plummer potential; for example, the average projected distance of both the set of massive stars and the set of all observed stars in the Arches cluster is roughly twice the average distance predicted by a Plummer model based on the estimated total mass and central density of the cluster. We include the Plummer potential to approximate the combined gravitational influence of the entire cluster, including the estimated mass of stars too small or dim to be observed.

Figer et al. (1999a) provide estimates of the total mass of each cluster by measuring the mass of observed stars, assuming a Salpeter IMF slope, and extrapolating down to $1 M_{\odot}$ —observed stars account for at most 25% of the mass of the Arches cluster and 16% of the mass of the Quintuplet cluster. They also estimate the density of each cluster by determining the volume of the cluster from the average projected distance of stars from the cluster center, and dividing the total mass by this volume; because the values are calculated using the total cluster mass but only the average projected cluster radius, the density estimates are probably closer to the

Table 3.3. Properties of the Arches and Quintuplet clusters

Cluster	M ^a (M_{\odot})	ρ_0^a ($M_{\odot} \text{ pc}^{-3}$)	b (pc)
Arches	2.0×10^4	6.3×10^5	0.20
Quintuplet	6.3×10^3	1.6×10^3	0.98

^aSee Figer et al. (1999a).

central densities than the average densities. We assume that the values reported are the central densities of the clusters. The total cluster mass and central density and the calculated value of b for each cluster are presented in Table 3.3.

3.2.2 Wind Sources

We implement wind sources as literal sources of SPH particles, using the scheme described in chapter 2. The mass loss rates and wind velocities inferred from observations are reported in Tables 3.1 and 3.2. We position each source at its observed x and y location and choose the z coordinate randomly, subject to the constraint that the wind sources are uniformly distributed over a range in z equal to the observed range in x and y . The choice of z positions has a much smaller effect on the X-ray luminosity than the choice of mass-loss rate (discussed below); in chapter 2 we presented the results of simulations of wind sources in the central few parsecs of the Galaxy with two different sets of z positions, and the average 2–10 keV X-ray luminosity from the central $10''$ of the simulations differed by only 16% ($7.50 \times 10^{31} \text{ erg s}^{-1} \text{ arcsec}^{-2}$ from a simulation with a dense arrangement of wind sources in the center of the volume of solution versus $6.45 \times 10^{31} \text{ erg s}^{-1} \text{ arcsec}^{-2}$

from a simulation with wind sources uniformly distributed in z). In addition, Raga et al. (2001) conducted three simulations of the Arches cluster in which z positions of sources were chosen by sampling from a distribution function $f(R) \propto R^{-2}$; they found a difference in 0.5 – 8 keV X-ray luminosity of only 3% between the most and least luminous simulations.

Figure 3.1 shows the positions in the sky plane of the wind sources in the Arches cluster, while Figure 3.2 shows the wind sources in the Quintuplet cluster; the size of the circle marking each source corresponds to the relative mass loss rate (on a linear scale) for that star. The initial temperature of the winds is not well known; for simplicity, we assume that all of the winds have a temperature of 10^4 K. Our results are fairly insensitive to this value, however, since the temperature of the shocked gas is determined primarily by the kinetic energy flux carried into the collision by the winds. The sources are assumed to be stationary over the duration of the simulation.

We conduct two simulations of the wind-wind interactions in each cluster; the simulations differ only in the choice of mass-loss rate for each star, with the wind speed assumed constant. The “standard” simulations use mass-loss rates inferred from observations as described in §§ 3.1.1 and 3.1.2, while the “high- \dot{M} ” simulations use mass-loss rates increased from the standard value by a factor 2.

3.3 Observations

An on-axis *Chandra* observation of the Arches cluster was taken on 2004 June 8 for 98.6 ksec. The ACIS-I detector was placed at the focal plane. The data were analyzed with the latest CIAO (version 3.1). While results of this observation will be presented in an upcoming paper (Wang, 2004), we concentrate here on the comparison of the data with the simulations. Figure 3.3 shows an overlay of an X-ray intensity contour map on a *HST* NICMOS image of the Arches cluster (Figer

et al., 1999b). The actual spatial resolution (with a FWHM $\lesssim 1''$) is better than what appears on this smoothed image. The position coincidence of the point-like X-ray sources and bright near-IR objects is apparent. To compare with the simulated cluster wind properties, we remove a region of twice the 90% energy-encircled radius around each of the sources.

3.4 Results

All four simulations were run significantly past the point in time when the stellar winds fill the volume of solution and gas shocked in wind-wind collisions fills the core of each cluster. The Arches cluster simulations were run past $t = 10,000$ yr; the Quintuplet simulations were run for over 14,000 yr. The winds in each simulation reach the edge of the volume of solution after $\sim 3,000$ yr, but the most relevant timescale for determining when the simulations reach a steady level of X-ray luminosity is the time required to fill the core of each cluster with shocked gas. The Arches cluster core is roughly five times smaller in radius than the core of the Quintuplet cluster, so the X-ray luminosity from the Arches simulations reaches a steady value relatively quickly compared to the Quintuplet simulations.

3.4.1 Total Flux and Time Variation

In order to calculate the observed continuum spectrum, we assume that the observer is positioned along the positive z -axis at infinity and we sum the emission from all of the gas injected by the stellar wind sources into the volume of each calculation. For the conditions encountered in the two clusters, scattering is negligible and the optical depth is always less than unity. For these temperatures and densities, the dominant components of the continuum emissivity are electron-ion (ϵ_{ei}) and electron-electron (ϵ_{ee}) bremsstrahlung. We assume that the gas is in ionization equilibrium, although spectra obtained from the Arches cluster with *Chandra* indicate the presence of

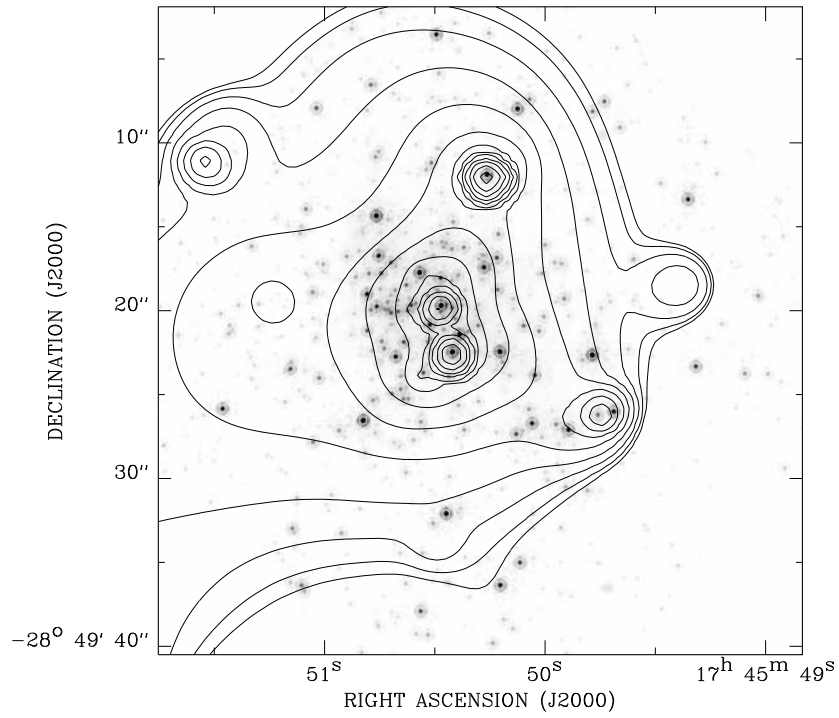


Figure 3.3 *Chandra* X-ray contours overlaid on *HST* Arches image. *Chandra* ACIS-I 1–9 keV intensity contours overlaid on a *HST* NICMOS image of the Arches cluster. The image is exposure-corrected and is adaptively smoothed with the CIAO csmooth routine ($S/N \sim 3\sigma$). The contour levels are at $(31, 32, 34, 38, 46, 62, 94, 158, 286, 542, 1054, 2078, 4126) \times 10^{-3} \text{ counts s}^{-1} \text{ arcmin}^{-2}$.

line emission at 6.4 keV; however, no other significant lines are observed, so our use of a bremsstrahlung model without line emission is a reasonable approximation. Future, more refined versions of the calculations reported here will need to include the effects of partial ionization in the shocked gas, a condition suggested by the iron line emission. We note, however, that the overall energetics and diffuse X-ray luminosity calculated by assuming full ionization err only marginally since the fraction of charges free to radiate via bremsstrahlung should be very close to one.

The X-ray luminosities calculated from our simulations support the recent result of Law & Yusef-Zadeh (2004) that the majority of the X-ray emission from these clusters (e.g., $\sim 60\%$ for Arches) is probably due to point sources. The diffuse 0.2–10 keV X-ray luminosity calculated from our “standard” Arches cluster simulation— 5.4×10^{34} erg s $^{-1}$ —falls below the 0.2–10 keV luminosity of 4.1×10^{35} erg s $^{-1}$ from the A1 and A2 components reported in Yusef-Zadeh et al. (2002); the simulation using elevated estimates for the mass-loss rates produces 2.2×10^{35} erg s $^{-1}$ between 0.2 and 10 keV, or 53% of the emission observed by *Chandra*. On the other hand, Law & Yusef-Zadeh (2004) now identify A1 and A2 as point-like components; after subtracting the contributions of A1 and A2, Yusef-Zadeh et al. (2002) find that the A3 component has a 0.5–10 keV luminosity of $\sim 1.6 \times 10^{34}$ erg s $^{-1}$. Our “standard” simulation produces 2.7×10^{34} erg s $^{-1}$ between 0.5 and 10 keV; lowering the mass-loss estimates of all wind sources by $\sim 30\%$ or slightly decreasing the assumed wind velocities would produce even better agreement.

Our “standard” and “high- \dot{M} ” simulations of the Quintuplet cluster produce 1.5×10^{33} erg s $^{-1}$ and 5.9×10^{33} erg s $^{-1}$, respectively, between 0.5 and 8 keV. Law & Yusef-Zadeh (2004) estimate a 0.5–8 keV luminosity of $\sim 1 \times 10^{34}$ erg s $^{-1}$ for the diffuse emission from the Quintuplet cluster, but they point out that other regions of diffuse emission to the north and south of the cluster introduce a complicated

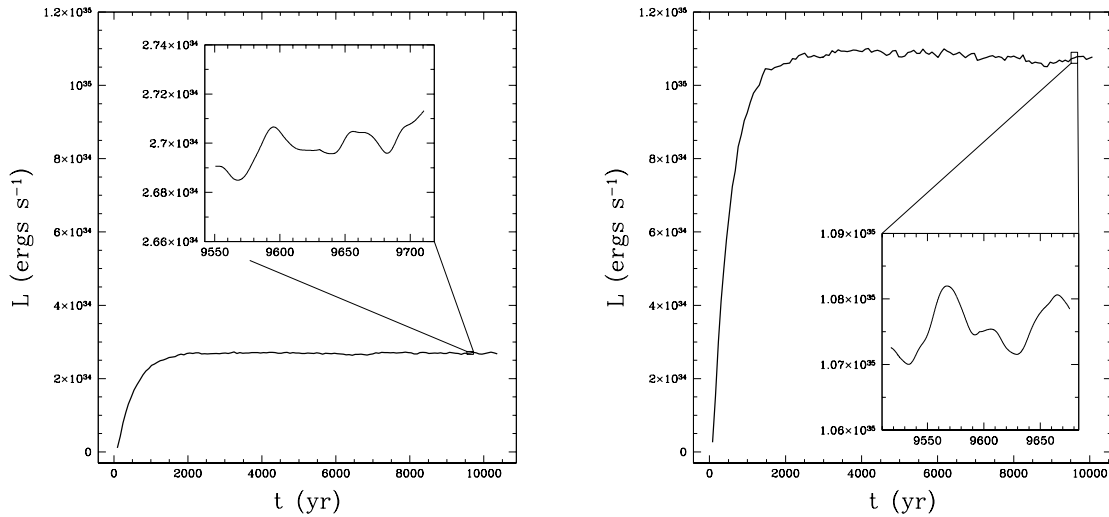


Figure 3.4 X-ray luminosity from Arches cluster simulations. The 0.5–8 keV X-ray luminosity versus time from the “standard” (left) and “high- \dot{M} ” simulations of the Arches cluster. The large plot shows the variation in luminosity over the entire calculation, while the inset plot shows variation on a timescale of ~ 10 years. The winds fill the core of the cluster after $\sim 2,000$ years.

pattern of background emission and limit the precision of this estimate.

The long-term variation of the X-ray luminosity as a function of time demonstrates some of the key differences between the two clusters. Figures 3.4 and 3.5 show the time variation of the 0.5–8 keV X-ray luminosity from all four simulated clusters. Each large graph shows the variation over the course of the entire simulation ($> 10,000$ yr for the simulations of the Arches cluster, and $> 14,000$ yr for the Quintuplet simulations), while each inset graph shows variation over 1,000 timesteps, or ~ 150 yr. The fact that the Quintuplet cluster is nearly five times larger in radius than the Arches cluster means that much more time is required for shocked gas to fill the central region. The Arches cluster reaches a steady X-ray luminosity after less than 2,000 yr, while the luminosity of the Quintuplet cluster does not clearly level off until more than 10,000 yr have passed.

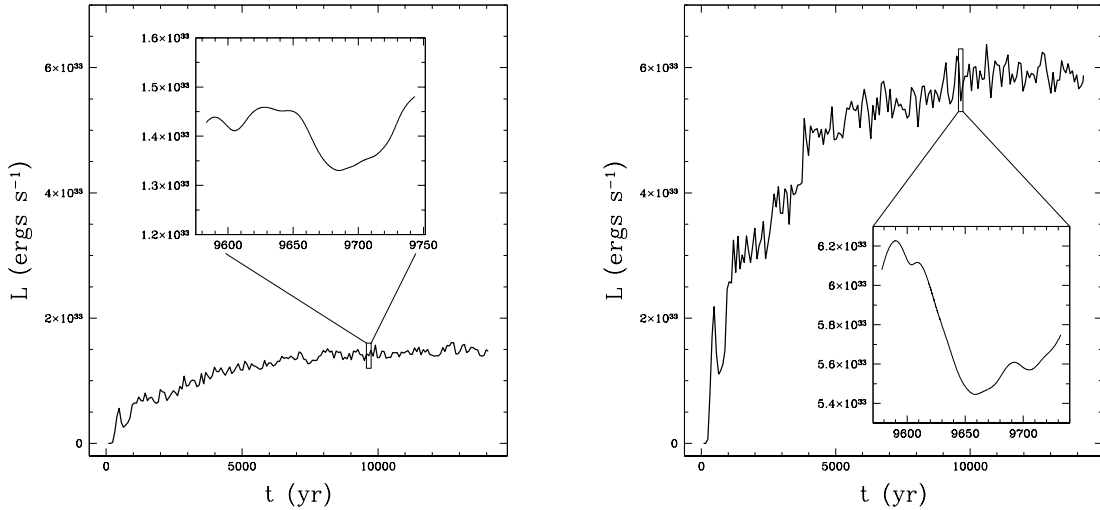


Figure 3.5 X-ray luminosity from Quintuplet cluster simulations. The 0.5–8 keV X-ray luminosity versus time from the “standard” (left) and “high- \dot{M} ” simulations of the Quintuplet cluster. The large plot shows the variation in luminosity over the entire calculation, while the inset plot shows variation on a timescale of ~ 10 years. The winds fill the core of the cluster after $\sim 10,000$ years.

The two clusters also exhibit differences in the size of short-term fluctuations in X-ray luminosity. Both simulations of the Arches cluster show short-term variations in luminosity of $\sim 1\%$ over timescales of ~ 50 yr, while the X-ray luminosity in the “standard” Quintuplet simulation fluctuates by $\sim 4\%$, and short-term variations in the “high- \dot{M} ” simulation of the Quintuplet cluster are as large as $\sim 7\%$.

3.4.2 Spatial Variation of the X-ray Flux

Figure 3.3 shows that many of the bright X-ray peaks in the Arches cluster correspond to actual stars, presumably binaries whose binary wind interactions produce the strong localized X-ray emission. These sources must be subtracted to study the diffuse X-ray emission.

The simulated 0.5–8 keV X-ray contours from the region near the core of the Arches cluster, shown in Figure 3.6, are generally comparable to the contours gen-

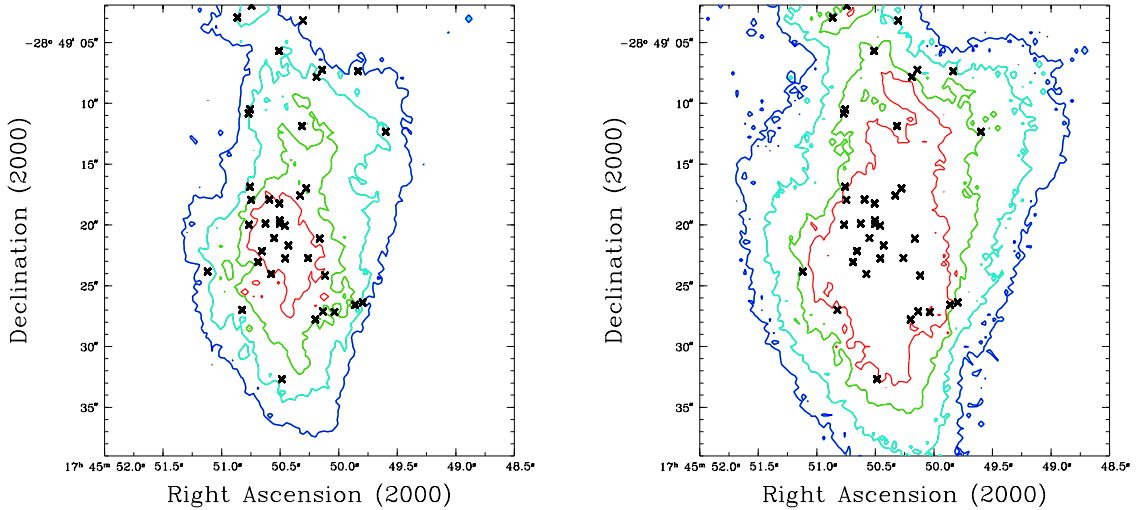


Figure 3.6 X-ray contours from Arches cluster simulations. Contours of column-integrated 0.5–8 keV X-ray luminosity per arcsec² from the “standard” (left) and “high- \dot{M} ” simulations of the Arches cluster. In order from blue to cyan to green to red, the luminosities indicated by the contours are 10^{30} , 2.5×10^{30} , 8×10^{30} , and 2×10^{31} ergs s⁻¹ arcsec⁻². The crosses indicate the positions of wind sources included in the simulations.

erated from *Chandra* observations (Figure 3.3; see also Figure 2b, Yusef-Zadeh et al., 2002). The strongest emission in the simulations and in *Chandra* images comes from the core of the cluster, and both sets of contours form elliptical patterns aligned primarily north-south. X-ray contours from the simulation of the Quintuplet cluster are shown in Figure 3.7; the Quintuplet cluster is significantly less dense than the Arches cluster, so the X-ray emission is correspondingly less strongly peaked toward the center of the cluster.

The plots in Figure 3.8 show the total 0.5–8 keV luminosity from concentric columns aligned along the line of sight and extending outward in radius from the center of the Arches (left) and Quintuplet (right) clusters. The most luminous gas in the Arches cluster is confined to within 20'' of the center of the cluster; in contrast, we include stars beyond 50'' in the Quintuplet cluster, and its luminosity continues

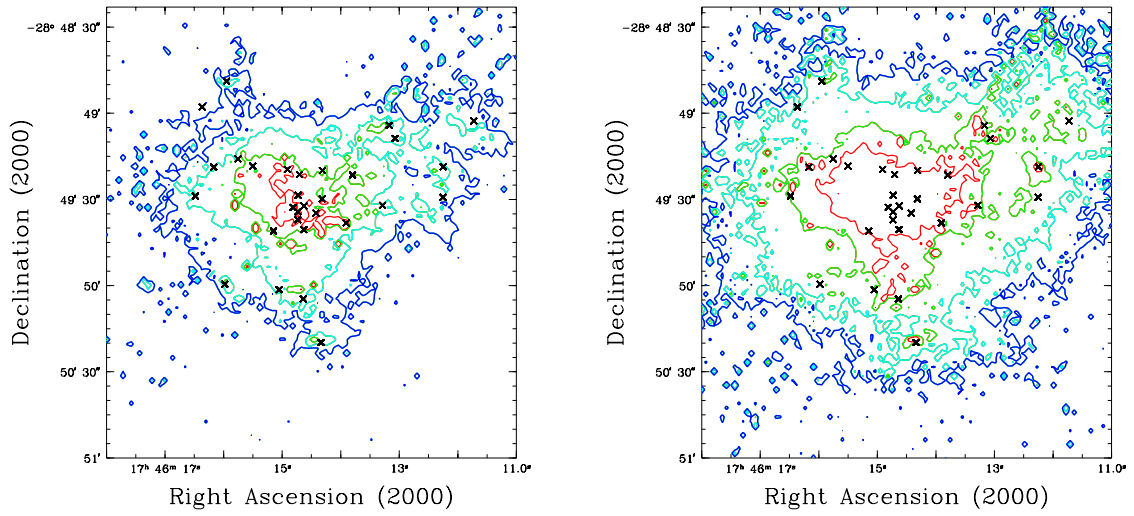


Figure 3.7 X-ray contours from Quintuplet cluster simulations. Contours of column-integrated 0.5–8 keV X-ray luminosity per arcsec² from the “standard” (left) and “high- \dot{M} ” simulations of the Quintuplet cluster. In order from blue to cyan to green to red, the luminosities indicated by the contours are 7×10^{28} , 1.8×10^{29} , 7×10^{29} , and 2×10^{30} ergs s⁻¹ arcsec⁻². The crosses indicate the positions of wind sources included in the simulations.

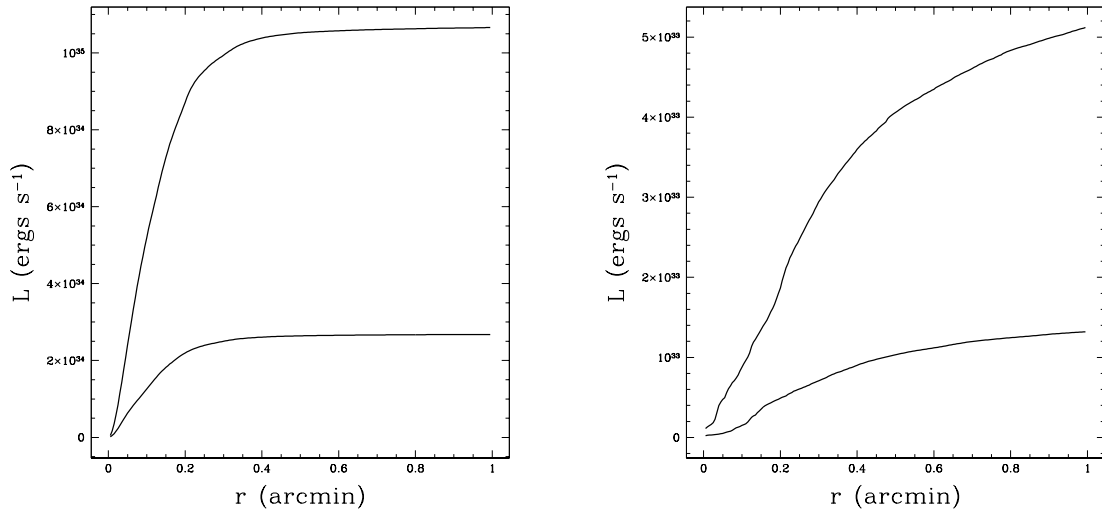


Figure 3.8 Cumulative radial profiles of X-ray luminosity. Total 0.5–8 keV X-ray luminosity from concentric cylinders aligned with the center of the Arches (left) and Quintuplet clusters. The lower line in each graph represents the “standard” simulation of that cluster; the upper line represents the “high- \dot{M} ” simulation.

to increase even beyond a radius of $50''$.

Similarly, the plots in Figure 3.9 show the 2–8 keV X-ray flux per square arcmin as a function of distance from the center of each cluster from all four simulations. The individual crosses and error bars in the graph from the Arches cluster represent flux measurements from *Chandra* observations of the cluster, after point sources have been removed and an estimate of the background X-ray flux has been subtracted. Here we assume that all of the emission centered around NICMOS stellar sources is due to binary wind interactions. The estimated background— $0.064 \text{ counts s}^{-1} \text{ arcmin}^{-2}$ —is the average number of counts obtained in an annulus between radii of $0.5'$ and $0.9'$. The simulations of the Arches cluster apparently produce more X-rays near the center of the cluster but decrease in intensity more rapidly toward larger radii. The relatively flat surface brightness profile evident in the *Chandra* data outside a radius of $0.3'$ may arise in part from the presence of

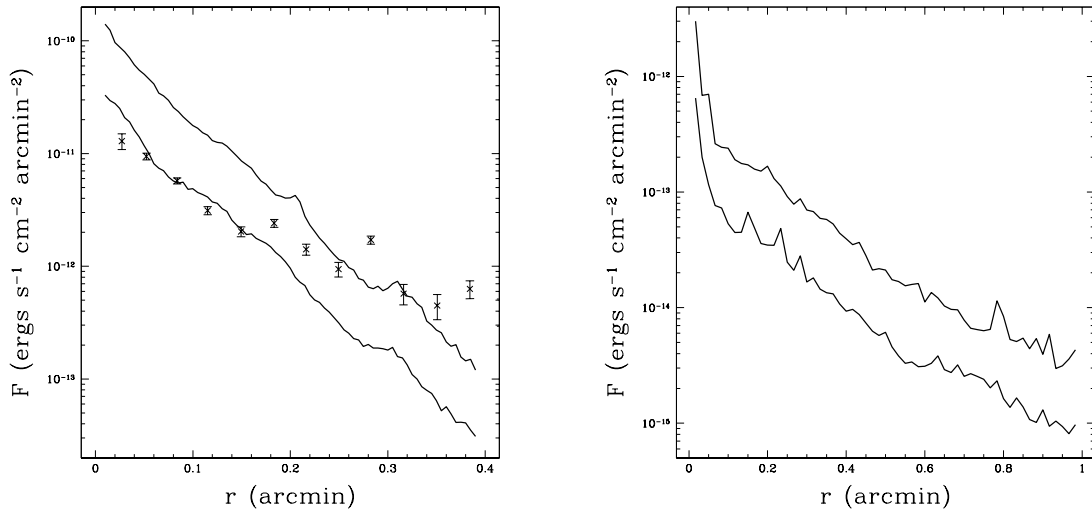


Figure 3.9 Simulated radial profiles of X-ray flux per arcmin². The 2–8 keV X-ray flux per arcmin² from concentric cylinders aligned with the center of the Arches (left) and Quintuplet clusters. The lower line in each graph represents the “standard” simulation of that cluster; the upper line represents the “high- \dot{M} ” simulation. Crosses and error bars in the left graph represent flux measurements from *Chandra* observations of the Arches cluster.

additional background X-ray emission near the Galactic center. It may also indicate confinement of the X-ray-emitting gas in the Arches cluster by ram pressure exerted by a molecular cloud or other external medium surrounding the cluster; our calculations include no such medium, so the simulated gas escapes and cools more rapidly as it leaves the core of the cluster.

One way to constrain the amount of confining material surrounding the cluster is to measure expansion velocities of the gas out of the cluster. In our simulations, which did not include confining gas, the material accelerates until it reaches an asymptotic velocity limit roughly equal to the mean wind velocity (Figure 3.10). In the Arches cluster, we reach that limit. In the (larger) Quintuplet cluster, that limit apparently occurs at a distance from the cluster center that is larger than the size of the simulation. However, if molecular clouds or additional stars with strong

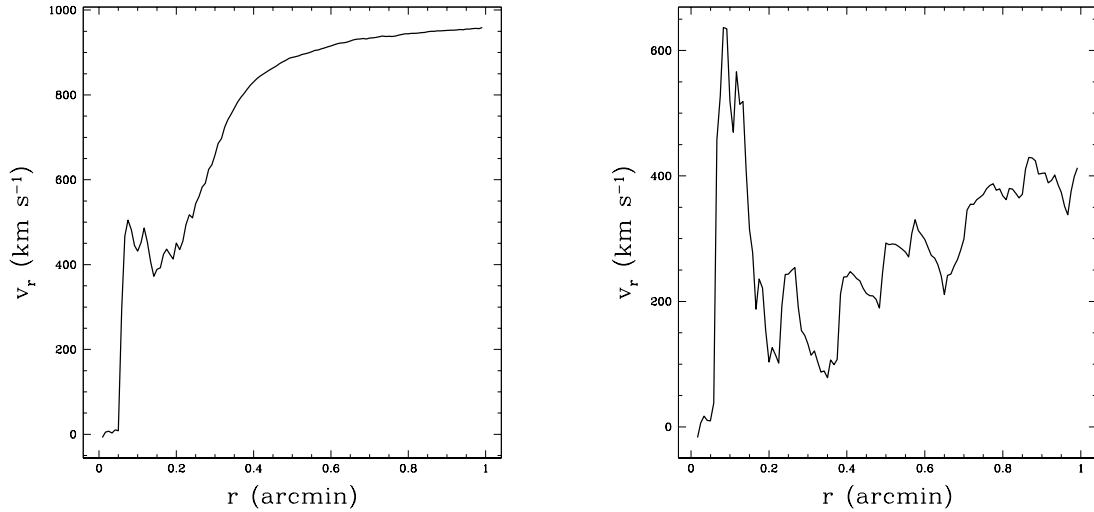


Figure 3.10 Average radial velocity of gas in the cluster simulations. Average radial velocity of gas in the “standard” simulations of the Arches (left) and Quintuplet clusters, versus distance from the center of each cluster.

winds are producing a confining ram pressure around this cluster, the outflowing gas will decelerate. Measurements of this velocity will constrain the parameters of the surrounding material; future simulations can use these constraints to include the effects of this material.

3.5 Discussion

Although the diffuse X-ray flux in clusters may be used to probe stellar mass-loss, two notable complications in the case of the Arches and Quintuplet clusters are the X-ray background present in the Galactic center, and the contributions made to the overall emission by point (i.e., binary wind) sources. The contribution made by the X-ray background is difficult to quantify; Law & Yusef-Zadeh (2004) report that background contributions lead to significant uncertainty in the measured X-ray flux from the Quintuplet cluster. The contribution from point sources is easier to handle; with its relatively high spatial resolution, *Chandra* can produce reasonable

images in which the required point-source subtraction may be made. Point sources in the Arches cluster all exhibit a 6.7 keV line; the absence of such a line in the spectrum of the diffuse emission indicates that the point-source contribution to the diffuse emission is not likely to be significant.

If, based on the observations made by Yusef-Zadeh et al. (2002), we assume that A1 and A2 are not point-like and do not subtract the contributions of point sources from the overall X-ray flux, it appears that the diffuse X-ray flux is consistent with higher mass-loss rates than the $(0.3 \times 10^{-5} M_{\odot} \text{ yr}^{-1})$ $3 \times 10^{-5} M_{\odot} \text{ yr}^{-1}$ assumed for stars (less than) above $60 M_{\odot}$. As we have seen, however, the observed point-source-subtracted diffuse emission matches our calculated X-ray flux to within a factor 2 when we adopt the currently accepted stellar mass-loss rates. Indeed, lowering the mass-loss rate estimates of all wind sources by about 30% would produce significant agreement between theory and observation. But we must make sure that we have a complete accounting of all the wind sources and carry through with a more careful point-source subtraction before we can completely confirm such claims.

The fact that the simulated X-ray flux density from the Arches cluster drops off more rapidly than the observed profile (see Figure 3.9) means that (1) we may have underestimated the contribution of the X-ray background; or, (2) we have ignored the possibly important dynamical influence of a confining molecular gas outside the cluster. Interpreting data beyond these radii (roughly $0.3'$ for Arches and $1.0'$ for Quintuplet) requires more detailed information on the cluster environment there.

X-rays do prove to be an ideal probe of bulk mass-loss rates in clusters. The X-ray emission depends sensitively on the mass-loss rates of the constituent stars and, based on our simulations of the Arches cluster, we can already limit the mass-loss rates to within a factor of 2 of the currently accepted values. This also implies that the assumed abundances in the Galactic center environment are essentially correct,

since the mass-loss rates from stellar models depend on the adopted metallicity. In addition, studying the X-ray emission from the outer region of the cluster may eventually lead to a better understanding of the medium within which the cluster is embedded. This is clearly relevant to the question of how these unusual clusters came to be, and the relative roles played by “standard star formation” versus stellar capture from outside the cluster. The inferred stellar constituents of these clusters (Cotera et al., 1996; Figer et al., 1999a, e.g.,) also seem to be consistent with the required mass loss rates, so the inferred unusual mass function of the Arches, Quintuplet, and Central clusters continues to pose a challenge to our understanding of how these stellar aggregates were first assembled.

CHAPTER 4

THE X-RAY RIDGE SURROUNDING SGR A* AT THE GALACTIC
CENTER

4.1 Introduction

While Sagittarius A* (Sgr A*) dominates the gravitational dynamics in the central parsecs of the Galaxy, many other components are required to explain the wealth of detailed observations of this busy region. Even as we focus on the inner 3 parsecs, it is clear that other classes of object contribute to the overall radiative emission from the Galactic center (for a recent review, see Melia & Falcke, 2001; see also Maeda et al., 2002). For example, the medium within which Sgr A* is embedded—bounded by the circumnuclear disk (CND, with inner radius $\sim 2\text{--}3$ parsecs)—has a temperature ~ 1.3 keV and emits a *Chandra*-detectable glow of diffuse X-rays (Baganoff et al., 2003). We showed in chapter 2 that this emission may be understood as the result of mutual interactions between the winds of Wolf-Rayet and O/B stars within ~ 1 parsec of the supermassive black hole.

The CND is perhaps the shredded remains of a giant molecular cloud that passed by Sgr A*. The cavity within the inner $\sim 2\text{--}3$ parsecs of this structure may itself have been created by the ablative influence of the cumulative wind outflow, which has by now produced a bubble of hot, ionized plasma. To make matters even more complex, observations of the supernova (SN) remnant Sgr A East suggest that its broadband emission arises from shock heating in a recent ($< 10,000$ -year-old) supernova (or other explosive outburst; see Mezger et al., 1989) originating within ~ 3 parsecs of the black hole.

Any comprehensive model of this region must therefore include the effects of all these components: the supermassive black hole, the Wolf-Rayet and O/B winds, the dense CND and the expanding supernova remnant, which we now see predominantly as a radio-emitting shell. Although interacting winds can explain the bulk of the diffuse X-ray flux from the inner $\sim 2\text{--}3$ parsecs, several other features seen in the *Chandra* X-ray image are not as easy to explain without the influence of some other interaction. In particular, a well-defined ridge of X-ray emission just outside the central region, to the NE of Sgr A* (see Figure 4.1), may be evidence of an ongoing collision between the SN ejecta and the cumulative Wolf-Rayet and O/B winds emanating from within the cavity (Maeda et al., 2002).

In this chapter, we model the expansion of the supernova, focusing on the effect this explosion has on the central few parsecs surrounding Sgr A*. We then directly compare the X-ray emission arising from the interaction zone with the actual *Chandra* image.

Interestingly, using the well-studied wind conditions at the Galactic center, we may also be able to place tighter constraints on the supernova explosion itself—both the released energy and the age of the remnant. With this knowledge, we can address several outstanding issues pertaining to the influence of this explosion on the morphology of the Galactic center: Did the supernova shock clear out the region surrounding the black hole, effectively shutting down what would otherwise have been a high accretion rate onto the black hole? Could the supernova have caused a brief increase in the accretion rate onto Sgr A*, producing a spike in X-ray emissivity that irradiated the X-ray-fluorescing Sgr B2 and other nearby molecular clouds some 300 years ago (see, e.g., Sunyaev & Churazov, 1998; Fromerth et al., 2001)?

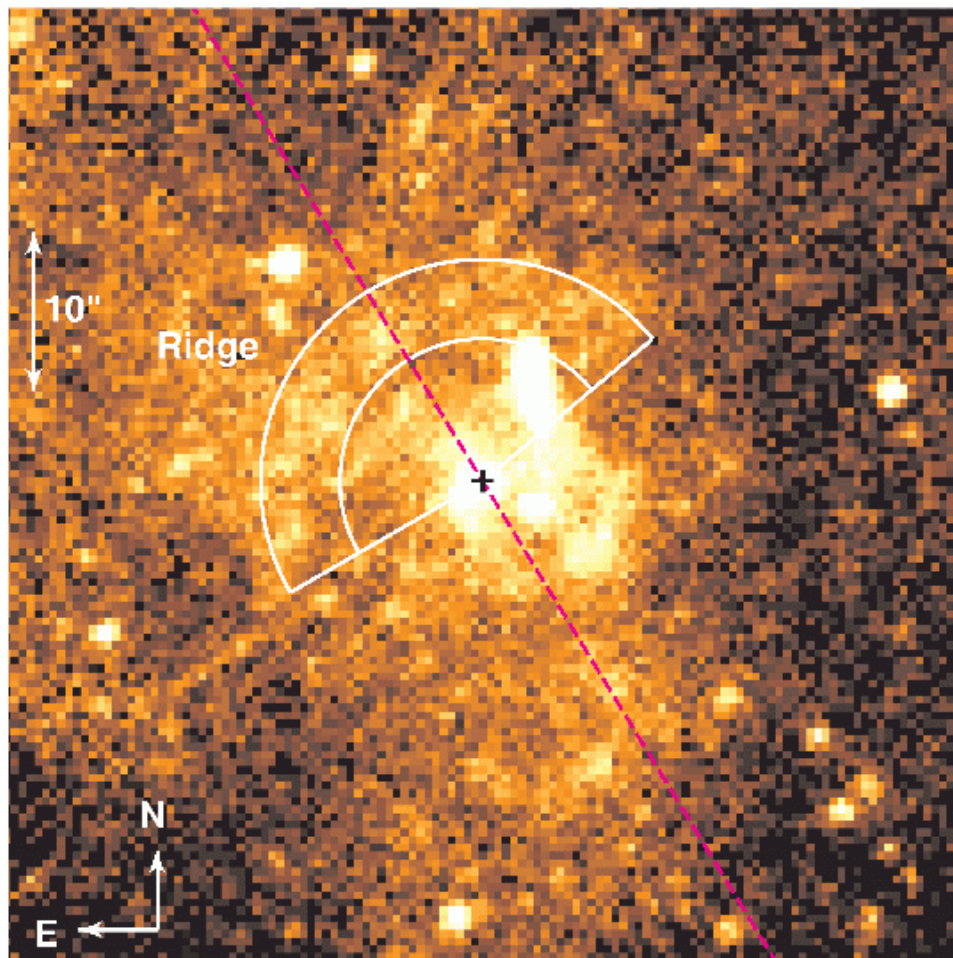


Figure 4.1 *Chandra* image of the central square arcminute. *Chandra* image of the inner $1' \times 1'$ of the Galaxy, centered on the location of the radio source Sgr A*. The (square) pixel size is $0.''492 \times 0.''492$, and the two arcs indicate distances of $9''$ and $15''$ from the center. The X-ray ridge, to the NE of Sgr A* and in the direction of Sgr A East, is bounded by these two arcs.

4.2 General Physical Principles

Our simulation uses the SNSPH smoothed particle hydrodynamics code (Fryer et al., 2006a) to follow the supernova explosion as it crosses the Galactic center. The domain of solution is a cube, 6 pc on a side, centered on the black hole. Particles that move beyond this domain, or within 1.9×10^{17} cm of the origin (effectively onto the black hole), are removed to simulate outflow (or inflow) conditions. Our initial (pre-explosion) conditions are taken from the structure of the wind-swept medium at the end of the simulation presented in chapter 2. The initial particle distribution is constructed from a ~ 1 million particle supernova explosion placed 2 pc due east (in right ascension) of the central supermassive black hole within a ~ 6 million particle wind-filled Galactic center region.

We assume that the density structure within this domain of solution at the time of the supernova explosion is dominated by matter lost by the Wolf-Rayet and O/B stars, plus the dense CND surrounding the central black hole. The CND is mimicked by 200 spherical clumps (totaling $10^4 M_{\odot}$), in a torus with a low filling factor surrounding the black hole. The winds from these stars (which we assume have not changed noticeably in the past 10,000 years) have blown a bubble in the Galactic center that is probably at the edge of the 50 km s^{-1} molecular cloud (Mezger et al., 1989).

Note, however, that our initial conditions do not include the initial molecular cloud blown out by the stellar winds. There is evidence that the supernova shock has reached the boundary between the wind-blown bubble and this cloud (Yusef-Zadeh et al., 1999). We can not address these effects with this current set of simulations. We also do not include the effect of mass loss from the supernova progenitor itself. However, the density structure near the X-ray ridge and the central black hole is dominated by the ~ 25 stars we do include (see chapter 2), and not by any outer

stars or the surrounding molecular cloud.

The structure of the supernova ejecta is set using a spherically symmetric model from Hungerford et al. (2005a). This $15 M_{\odot}$ star is exploded with an energy of 1.5×10^{51} erg; these properties are typical of a supernova explosion, both in composition and energy. We place the explosion into our domain of solution after the shock has moved out for 1 year, at which point the explosion material is still within 0.02 pc of the supernova site.

4.3 Calculations and Results

The wind-swept initial conditions of the Galactic center lead to an aspherical progression of the supernova shock. Plowing through diffuse regions with density ~ 1 particle cm^{-3} , across the dense CND, and through central regions with densities $> 10^4$ particle cm^{-3} , the supernova shock is far from symmetric. The ejecta flow around the dense regions, taking the path of least resistance and producing shocks where they collide with and are decelerated by the dense material. Figure 4.2 shows the density profile and position of a set of tracer supernova particles 650 years after the launch of the supernova explosion. This is roughly the time of deepest penetration of the supernova ejecta into the region surrounding the supermassive black hole. The actual supernova shock has now moved beyond the Galactic Center and has already passed beyond the southern and eastern edges of our simulation grid. The ejecta do not sweep through the central region, nor do they significantly alter the density of the inner 0.2 pc surrounding the black hole. A more detailed discussion of the effects of the supernova shock on the central region, the implications for the black hole accretion rate, and the possible excitation of Sgr B2, will be presented in chapter 5.

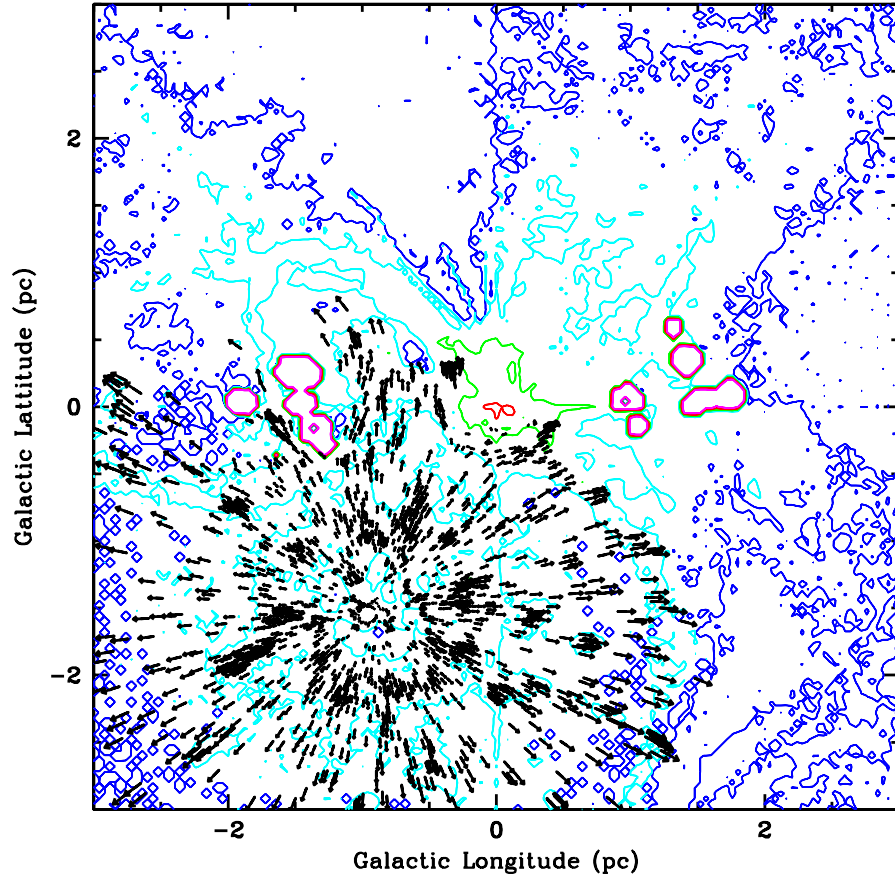


Figure 4.2 Simulated density contours. Density contours of a 2-dimensional slice of the inner 3 pc surrounding Sgr A* 650 y after the launch of the supernova explosion. The contours take mean densities from a 0.2 pc slice centered on the radial distance of the supermassive black hole and correspond to number densities of 1 (blue), 10 (cyan), 100 (green), 1000 (red), and 10^4 (magenta) cm^{-3} . The supermassive black hole is located at 0,0. Roughly at longitude = -0.89 pc, latitude = -1.47 pc is the origin of the supernova (at the same radial distance as the supermassive black hole). The circumnuclear disk is modeled with several dense spherical clumps with a low volume filling factor (magenta contours). The vectors show tracer particles of the supernova ejecta themselves (arrows denote velocity direction and length denotes velocity magnitude). Note that the explosion flows around Sgr A* and the dense central region along paths where the density is lowest.

Mezger et al. (1989) estimated the age and energy of the supernova remnant by assuming the supernova was plowing through a 10^4 particle cm^{-3} molecular cloud. They calculated a supernova remnant age of 7,500 years and, to fit the observed shock temperature, they required an explosion energy in excess of 10^{52} erg. However, using the lower mean density in our wind-swept initial conditions allows us to account for the observed remnant characteristics with a more typical supernova explosion ($\sim 10^{51}$ erg). Our simulation also suggests that the supernova remnant is younger than the estimate of Mezger et al. (1989) (see chapter 5 for more details on the fitting). From the position of the shock, we can set a crude lower limit to the remnant's age at $\sim 1,000$ years, but a more precise answer may be determined by comparing our predicted X-ray ridge properties to the observations shown in Figure 4.1.

The column integrated X-ray emission from our models is shown in Figure 4.3 in a series of temporal snapshots. For very energetic shocks, the high compression ratio at the point of impact can lead to significant particle acceleration and nonthermal emission, but by this time in the interaction, the dominant 2–10 keV emission mechanism is expected to be optically thin bremsstrahlung (see chapters 2 and 5 for details). The supernova shock reaches the dense inner 0.2–0.3 pc of the Galactic Center in 160 years and sweeps around this area after 650 years. The X-ray emission is highest where the shock is strongest (a function of both shock velocity and density of the impacted region).

By 1,740 years after the explosion, the supernova shock has swept beyond our simulation grid. However, over 95% of the mass in the supernova ejecta is moving at less than half the speed of the supernova shock front. This slow-moving material continues to impinge on the inner 0.2–0.3 pc of the Galaxy. It is the interaction between the stellar winds pushing against the slow-moving supernova ejecta that

produces the X-ray ridge observed today (Fig. 4.1).

For direct comparison between our simulation and the properties evident in Figure 4.1, we restrict our attention to the region bounded by the 9'' and 15'' arcs in this image; this appears to be the primary interaction site at the present time. The observed flux is accurately modeled with two components at different temperatures: a 5.6 keV component with a 2–10 keV flux of $3.92 \times 10^{-13} \text{ erg cm}^{-2} \text{ s}^{-1}$ and a 1 keV component with a 2–10 keV flux of $5.8 \times 10^{-13} \text{ erg cm}^{-2} \text{ s}^{-1}$; these correspond to 2–10 keV luminosities of $3.0 \times 10^{33} \text{ erg s}^{-1}$ and $4.4 \times 10^{33} \text{ erg s}^{-1}$, respectively, at a distance of 8 kpc from the Galactic center.

In our simulation, both the location of, and the X-ray intensity from, this region vary with time, so we have essentially two important constraints on the comparison between theory and observation. We suspect that the 1 keV component arises from either foreground or background emission; this is supported by the fact that the luminosity-weighted temperature in this region of our simulation is 4.9 keV after 1,740 years. From our simulation, we find that the column-integrated 2–10 keV luminosity from the interaction within the swath highlighted in Figure 4.1 is $3.6 \times 10^{33} \text{ erg s}^{-1}$ after 1,619 years and $2.7 \times 10^{33} \text{ erg s}^{-1}$ after 1,740 years. These values are within 20% of the observed luminosity of the 5.6 keV component, and the good match between theory and observation for both the morphology and the X-ray radiance of the ridge therefore provides us with compelling evidence that $\sim 1,700$ years must be a reasonable estimate for the remnant's age.

As the velocity of the impinging supernova ejecta decreases, the X-ray ridge moves out and dims. By 2,560 years, the ridge will have moved out 30'' and its flux should then be 3 times lower than its (current) 1,740-year value.

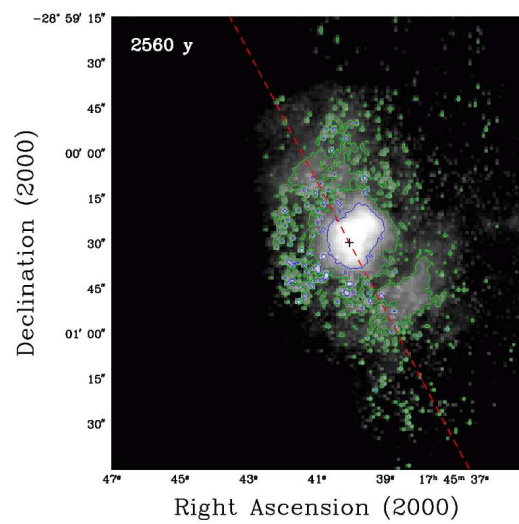
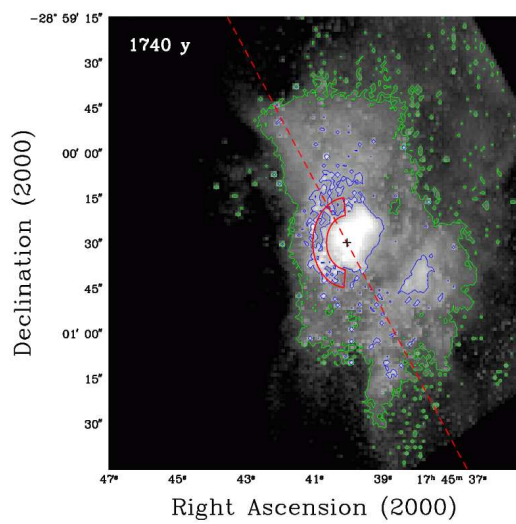
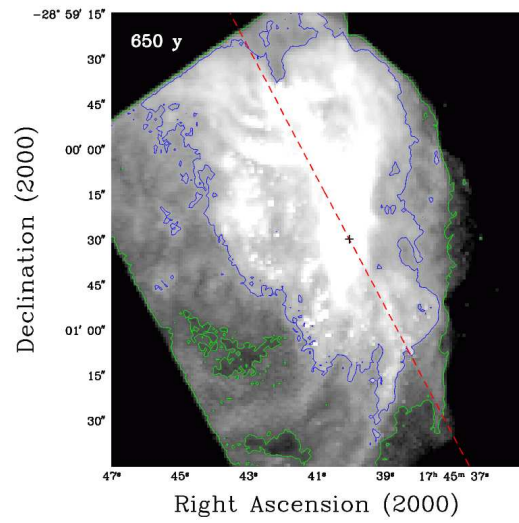
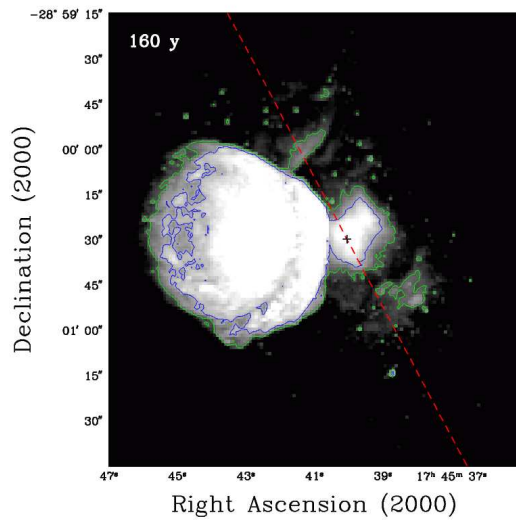
4.4 Conclusion

Our simulation of the passage of Sgr A East across the Galactic center has produced several new insights into the structure of the environment within ~ 3 pc of Sgr A*. The front of the SNR flowed around the Galactic center $\sim 1,100$ years ago (650 years after the supernova explosion). The shock front pushed back the combined winds from the Wolf-Rayet and O/B stars, but did not get within ~ 0.2 pc of the accreting supermassive black hole. The collision between the supernova ejecta and the central winds produces a ridge of X-ray-emitting gas $\sim 9''$ – $15''$ to the NE of the black hole. Comparing our simulations with the observations allows us to estimate the age of the supernova remnant to be $\sim 1,700$ years. We predict that this X-ray ridge will move out and dim with time. In ~ 800 years, it should be roughly twice its current distance from Sgr A*, and a factor ~ 3 dimmer.

The supernova did not significantly alter the accretion rate onto the black hole. Our simulations demonstrate how rich in information are the X-ray observations of the Galactic Center. Although this region contains several complex flows that are difficult to simulate completely, the extensive body of data contains many features that we can employ to tightly constrain the calculations. As we continue to refine our models, we expect to uncover additional new features regarding the environment and physical processes at the Galactic center.

This work has barely scratched the surface of what we can learn about the Galactic center by carefully studying the gas dynamics in this region. In chapter 5, we will discuss in more detail the hydrodynamic evolution of the shock and calculate the emission as the shock hits the large molecular cloud to form Sgr A East. We will also report in detail the metallicity gradients expected within Sgr A East as a function of time and distance from Sgr A*, providing yet another observational signature that may be used to better constrain this remnant's age.

Figure 4.3 Contours of X-ray luminosity at four different times. Contours of column-integrated 2–10 keV X-ray luminosity per $1''.2 \times 1''.0$ bin from our simulation, shown at four different snapshots in time (160, 650, 1740, and 2560 years after the supernova explosion). In order from blue to cyan to green to red, the luminosity densities indicated by the contours are 1.5×10^{29} , 10^{30} , 10^{31} , 10^{32} erg s⁻¹ bin⁻¹. At 160 years, the shock from the supernova ejecta hitting the dense wind-dominated region surrounding Sgr A* produces an X-ray hot spot. The X-ray hot spot moves around Sgr A* as the head of the supernova shock sweeps around the central region (650 years). After 1740 years, the stellar wind material begins to reassert itself. The shock between it and the slower moving supernova ejecta forms an X-ray ridge with a 2–10 keV luminosity of roughly 3×10^{33} erg s⁻¹. This is our best estimate for the current state of the Galactic center. With time, this ridge will move out and dim. By 2560 years after the launch of the explosion (800 years from now), the luminosity of the ridge will be a factor ~ 3 dimmer, and the feature will lie nearly $30''$ away from Sgr A*.



CHAPTER 5

THE SGR B2 X-RAY ECHO OF THE GALACTIC CENTER
SUPERNOVA EXPLOSION THAT PRODUCED SGR A EAST

5.1 Introduction

The conditions in the inner 3 pc of the Galaxy are set in large part by the complex interaction of over a dozen strong Wolf-Rayet star winds and the enveloping 50 km s^{-1} giant molecular cloud (M-0.02-0.07), combined with the strong gravitational pull of the central supermassive black hole (Sgr A*) (see Melia & Falcke, 2001, for a recent review). The large number of massive stars in this compact region suggests an additional influence—that of supernova explosions. Sgr A East is the remnant of such an event. An earlier consideration of its interaction with the molecular cloud, based on the energetics and time required to carve out the central cavity now occupied by Sgr A East (Mezger et al., 1989), pointed to an unusually powerful explosion, with an energy of $\sim 10^{52}$ ergs or greater, and a remnant age exceeding $\sim 10,000$ years. These estimates, however, ignored the importance of the stellar winds in clearing out the medium into which the supernova ejecta expanded following the incipient event. In chapter 4 we showed with detailed 3D hydrodynamic simulations that, when one takes this additional factor into account, the current morphology of Sgr A East is actually consistent with a normal supernova explosion energy ($\sim 10^{51}$ ergs). In addition, the relatively low gas density in the wind-filled region and the consequent more rapid expansion of the remnant into the surrounding medium leads to an inferred age much younger than 10,000 years, probably $< 2,000$ years.

Chapter 4 focused on the X-ray ridge to the NE of Sgr A*, formed by the

interaction of the stellar winds—which emanate from within the cavity enclosed by the circumnuclear disk (CND)—and the slowing supernova ejecta expanding away from the site of the explosion that produced Sgr A East. In this chapter, we discuss several additional features that have emerged from our simulations, along with other important implications of a young supernova remnant. These include the remnant’s evolution, its impact on the supermassive black hole’s accretion, and the spatial distribution of heavy elements formed in the supernova progenitor. In particular, we wish to examine the consequences of a young supernova remnant colliding with the 50 km s^{-1} cloud, focusing on the X-ray illumination this would have produced on extended objects, such as the molecular cloud Sgr B2, ~ 300 light years to the NE of Sgr A*. Sgr B2’s current emission of a strongly-fluoresced Fe line appears to be the X-ray “echo” of that interaction, providing the best (circumstantial) evidence of the impact the supernova would have had on the Galactic center in the past several hundred years.

We begin by describing the current observational status of Sgr B2 (§ 5.2) and then take a step back to discuss the basic principles of shock expansion in the Galactic center (§ 5.3). Using a combination of 3-dimensional and 1-dimensional simulations, we then show how the supernova shock would have affected the accretion rate onto Sgr A* (§ 5.4) and the concurrent evolution of the supernova remnant Sgr A East (§ 5.5), focusing on how these interactions might have accounted for the irradiation of Sgr B2. We also present abundance distributions produced by the explosion (§ 5.6) which, if measured, could provide us with much tighter constraints on the supernova explosion energy. Finally, we return to Sgr B2 and conclude with a possible explanation for the origin of the illumination that produced the current fluorescent Fe emission.

5.2 The Puzzle of Sgr B2

The region within ~ 100 pc of Sgr A* contains giant molecular clouds with a mean number density $\sim 10^4$ cm $^{-3}$ and a gas temperature on the order of 60 K (Lis & Carlstrom, 1994). Over the past decade, several instruments, including ASCA (Koyama et al., 1996; Murakami et al., 2000) and *BeppoSAX* (Sidoli, 1999), have revealed a source of bright fluorescent Fe K α line radiation within the cloud Sgr B2; several other smaller clouds also exhibit strong 6.4 keV line emission, though with low absolute fluxes compared to Sgr B2. The latter has a radius ~ 10 – 20 pc and a total enclosed mass ~ 2 – $6 \times 10^6 M_{\odot}$ (Lis & Carlstrom, 1994). All of these fluorescing clouds produce a 6.4 keV line with an unusually large equivalent width (EW > 1 – 2 keV), though Sgr B2 stands out with the largest width, at ≈ 2 – 3 keV. The surrounding continuum is quite flat, and shows strong absorption below 4.5 keV and a sharp Fe K α absorption feature at 7.1 keV.

The large EW is a strong indicator of how this fluorescent emission is produced (Sunyaev et al., 1993; Sunyaev & Churazov, 1998; Fromerth et al., 2001). A cloud radiates via X-ray fluorescence when it is illuminated, either internally or externally, by an X-ray source. However, a steady source embedded within the cloud produces an upper limit to the EW of only ~ 1 keV (see, e.g., Fabian, 1977; Vainshtein & Sunyaev, 1980; Fromerth et al., 2001), regardless of how one chooses the parameters. The smaller molecular clouds might therefore be marginally consistent with an internal illuminator (see, e.g., Fromerth et al., 2001). However, Sgr B2 must necessarily be illuminated either by a time-dependent internal source whose flux has diminished, or by an external source. In the former case, the continuum will have faded away relative to the line intensity; in the latter, we are not directly observing the full ionizing flux. In both cases, the equivalent width would be larger than in a situation where the continuum spectrum of the irradiating source is still visible.

Recently, Revnivtsev et al. (2004) have reported an association of the hard X-ray source IGR J17475-2822 with Sgr B2, showing that the ASCA (3–10 keV) and INTEGRAL/IBIS (20–400 keV) spectral components match very well. They showed that the combined spectrum at 3–200 keV can be well fit by a model in which X-rays from an external source, possibly at the location of Sgr A*, are scattered and reprocessed by a homogeneous spherical cloud of cold, molecular hydrogen and helium gas, with iron abundance ~ 1.9 times solar.

The possible identification of Sgr A* as the external illuminator of Sgr B2 would provide some measure of its recent variability at X-ray energies. This association is motivated in part by the fact that the iron emission in Sgr B2 is strongest on the side of the cloud facing Sgr A* (Koyama et al., 1996). We may be witnessing the X-ray echo, delayed by 300–400 years relative to the direct signal from the black hole, due to the light travel time from the Galactic center out to Sgr B2’s position. In this scenario, the fluorescent Fe emission would then be direct evidence of the black hole’s enhanced X-ray emissivity some 300 years ago.

Alternative scenarios seem to be falling out of favor (see, e.g., Revnivtsev et al., 2004). For example, although the time-dependent internal irradiator model can match the Fe line shape as well as the external irradiator (Fromerth et al., 2001), the lack of any significant variation in the line flux with the passage of time argues against this geometry. The large EW of the 6.4 keV line implies that the primary source should have faded away before the ASCA observation of 1993. But the light crossing time of the Sgr B2 cloud is ~ 30 –60 years, so one might have expected to see a detectable decline of the 6.4 keV line flux in the 7 years between the ASCA and *BeppoSAX* observations, unless the irradiation of Sgr B2 is still ongoing because not all the X-ray waves have yet reached the cloud.

Though it is very tempting to invoke Sgr A* as the external illuminator, there

are several reasons for taking a cautious view of this picture. Chief among them is the fact that this scenario would require a change in the black hole’s 2 – 10 keV X-ray luminosity by a factor of $\sim 10^6$ in only 300 years, from $L_x \approx 5 \times 10^{38}$ erg s^{-1} (Revnivtsev et al., 2004) to the currently observed value of $L_x \lesssim 10^{33}$ erg s^{-1} (Baganoff et al., 2003). One of the principal goals of this work is to examine the role played by the recent Galactic center supernova in illuminating Sgr B2, which may alleviate the difficulties described above.

5.3 Supernova Shocks at the Galactic Center

Molecular cloud remnants, inflowing plumes, and hot ionized bubbles all combine to form a complex density structure across the Galactic center, rendering it inappropriate for the “spherically symmetric cow” approach preferred by most theorists. These deviations from isotropy are well-reflected in the anisotropic propagation of the supernova shock. Figure 5.1 shows the initial 3-dimensional density structure used in our simulations. We have here made the same model assumptions as in chapter 4, in which the density profile is determined solely by the mass-losing stars interacting with the dense circumnuclear disk (CND) within the gravitational potential of the central supermassive black hole. We have also assumed that the stellar wind ejecta have not changed significantly in the past $\sim 5,000$ – $10,000$ years. Figure 5.2 shows a 0.2 pc slice of this density structure centered on Sgr A* at the time of the explosion.

Before we discuss the propagation of the shock through this complex density distribution, we review the spherically symmetric picture and consider the 3 basic evolutionary phases of supernova remnants and their shocks (Cox, 1972; Chevalier, 1974):

- Phase I (free-streaming): The supernova explosion initially propagates essentially unimpeded by the surrounding medium. This phase ends roughly when

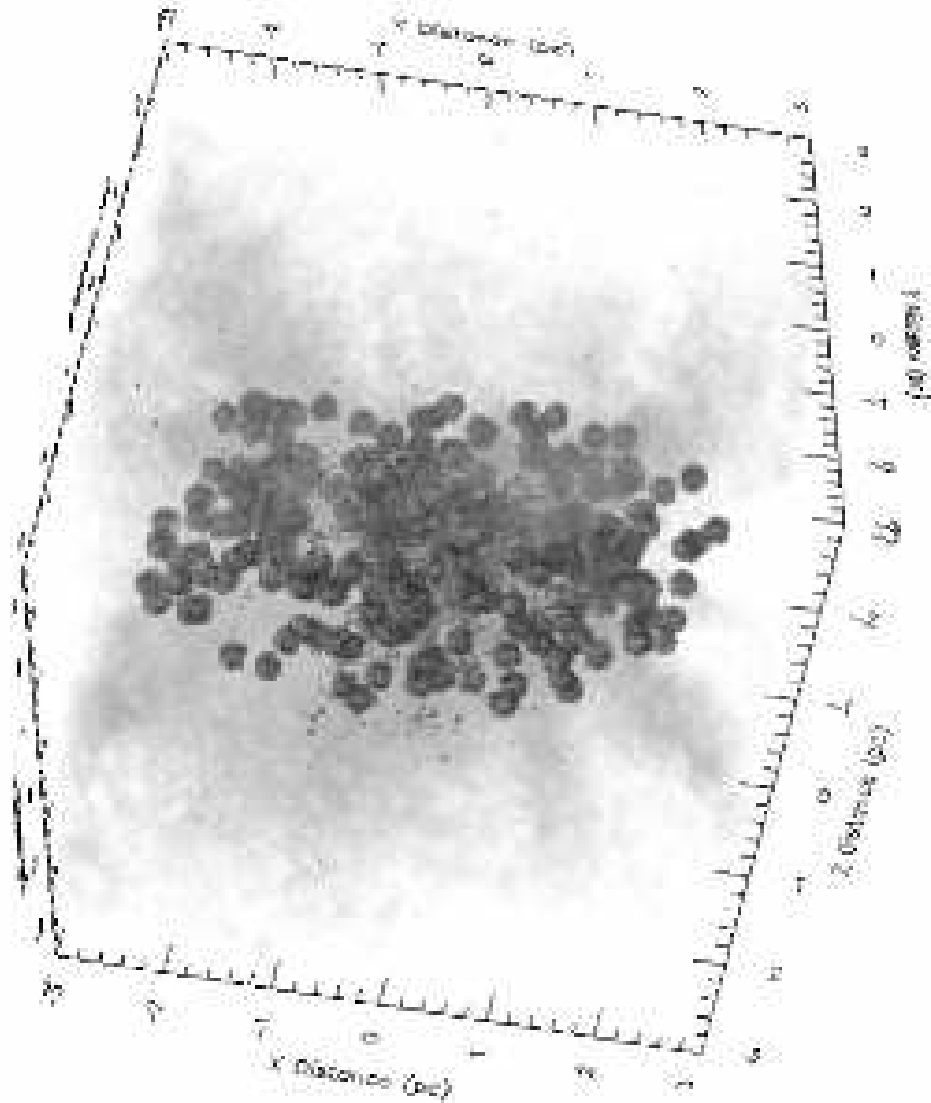


Figure 5.1 Simulated density profile of the Galactic Center. Density profile of the Galactic Center. The shading corresponds to number density values of $\log n \lesssim 1 \text{ cm}^{-3}$. The contour corresponds to density values of $\log n > 1.5 \text{ cm}^{-3}$. The contour shows our low-filling factor disk along with the high-density central region around Sgr A*. The shading shows the very aspherical structure of the low density matter.

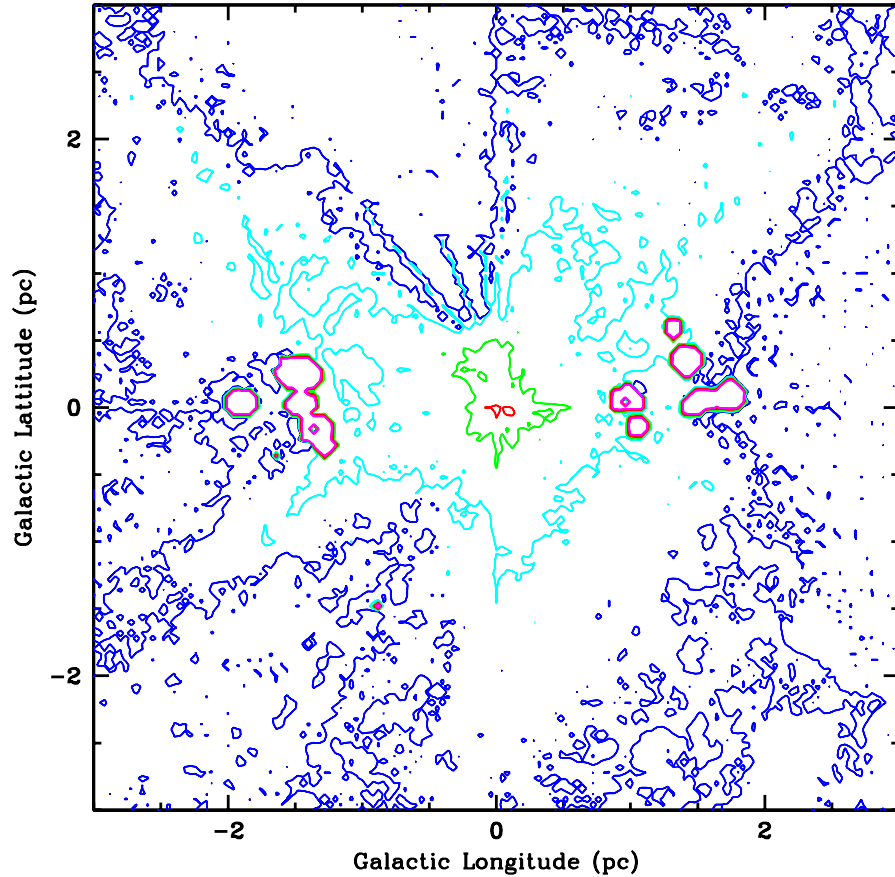


Figure 5.2 Simulated density contours. Density contours of a 2-dimensional slice of the inner 3 pc surrounding Sgr A*, 1 year after the launch of the supernova explosion at longitude = -0.89 pc, latitude = -1.47 pc. The contours show mean densities from a 0.2 pc slice centered on the supermassive black hole and correspond to densities of 1 (blue), 10 (cyan), 100 (green), 1,000 (red), and 10^4 (magenta) cm^{-3} . The supermassive black hole is at 0,0. The origin of the supernova appears as a small point density spike. The circumnuclear disk is modeled as a number of dense spherical clumps with a low covering factor (magenta contours). Note that the density in this inner region is much lower than that of a typical molecular cloud and is highly asymmetric.

the supernova has swept up a mass equal to the pre-explosion mass of the progenitor.

- Phase II (adiabatic): The remnant evolves into a second phase where cooling is still not important. The shock can be described using adiabatic, self-similar blast wave solutions (Sedov, 1959; Taylor, 1950).
- Phase III (snow-plow): The final phase occurs when radiative cooling becomes important. In this phase, the thermal energy of the shock is rapidly radiated and the shock moves forward by momentum conservation alone. This phase ends when the velocity of the shock decreases below the sound speed of the surrounding medium.

For a $15 M_{\odot}$ star, the end of the free-streaming phase ($t_{\text{free-streaming}}$), and the remnant's radial extent ($R_{\text{free-streaming}}$) at that time, are given, respectively, by the expressions

$$t_{\text{free-streaming}} \approx 2,000 E_{51}^{-1/2} n^{-1/3} \text{ years} \quad (5.1)$$

and

$$R_{\text{free-streaming}} \approx 5.3 n^{-1/3} \text{ pc}, \quad (5.2)$$

as functions of supernova explosion energy E_{51} (in units of 10^{51} ergs) and density of the surrounding medium n (in units of cm^{-3}). Here we have assumed that the velocity is $\sqrt{2E_{\text{SN}}/M_{\text{SN}}}$ (where E_{SN} and M_{SN} are the supernova energy and mass, respectively) which, however, underestimates the lead shock speed. We can use these spherical estimates, combined with the density structure at the Galactic center (Figure 5.2), to follow the free-streaming phase along specific paths. That portion of the supernova shock that moves away from Sgr A* (where the number density is low: $\sim 1 \text{ cm}^{-3}$) does not decelerate significantly until it hits the 50 km s^{-1} molecular cloud that surrounds the Galactic center (roughly 4 pc from the launch site of the

supernova). But the ejecta moving toward Sgr A* propagate through an increasingly dense medium. The remnant on this side of the explosion leaves the free-streaming phase more than 0.5 pc away from Sgr A*.

Beyond the free-streaming phase, but before radiative cooling becomes important, the shock propagates adiabatically. This phase lasts for a period set by the cooling time of the shock. Wheeler et al. (1980) estimated the radial and temporal extent of the shock for different cooling functions. When lines dominate, they find

$$t_{\text{cooling}} \approx 110 E_{51}^{0.22} n_4^{-0.56} \text{ years} \quad (5.3)$$

and

$$R_{\text{cooling}} \approx 0.29 E_{51}^{0.29} n_4^{-0.43} \text{ pc}, \quad (5.4)$$

where n_4 is the number density in units of 10^4 cm^{-3} . For the segment of the shock directed toward the Galactic center, where densities are in the range of $10^3 - 10^4 \text{ cm}^{-3}$, the shock travels less than ~ 0.5 pc before cooling takes over. From these rough calculations, we might therefore expect the shock to just reach Sgr A*. However, as we shall see in § 5.4, the fact that the shock can flow around this dense region, made impenetrable by the persistent outward ram pressure of the stellar winds, means that the shock actually never reaches the Galactic center. Correspondingly, the ejecta moving away from the Galactic center have a much more extended adiabatic phase; it lasts until they hit the molecular cloud, at which point the phase ends almost immediately.

Timing is also important. The total travel time for the ejecta to reach the nucleus is just 600 years. If the molecular cloud is 4 pc away from the explosion site, our rough velocity estimate leads to the shock leaving the adiabatic phase at roughly 1600 years. Let us now compare these results to the actual numerical calculations.

5.4 Time-dependent Accretion Onto Sgr A*

We use both 1-dimensional and fully 3-dimensional simulations to trace the evolution of the supernova remnant and to provide us with a basic understanding of its effect on the Galactic center. Of course, in the 1-dimensional case, we model the properties of the medium into which the shock front expands in an angle-averaged sense. Under the assumption of spherical symmetry, we have found that the shock passes through both its free-streaming and adiabatic phases prior to reaching Sgr A*, but that it is less clear whether or not the shock actually reaches Sgr A* before cooling and assimilating into its surroundings.

These spherically-symmetric simulations obviously cannot model the same geometric effects that appear in multi-dimensional calculations. Just as an ocean wave flows around a rocky promontory, the supernova shock will flow around the dense stellar-wind-filled region surrounding Sgr A*. Using the SNSPH code described in Fryer et al. (2006a), we have modeled the propagation of the supernova through the inner 3 pc region surrounding the Galactic nucleus (for details, see chapter 4. The density profile was taken from the simulations presented in chapter 2 and the supernova was assumed to occur with an energy of 1.5×10^{51} ergs, in a progenitor with a mass of $15 M_{\odot}$ (Hungerford et al., 2005a). We placed it at longitude = -0.89 pc and latitude = -1.47 pc relative to Sgr A* in Galactic coordinates, or 2 pc due east of Sgr A* in right ascension (but at the same radial distance from us). We have also modeled a more energetic explosion ($\sim 1.2 \times 10^{52}$ erg) by artificially increasing the velocity of the ejecta by a factor 3; Table 5.1 summarizes the properties of both simulations.

Figure 5.3 shows a series of snapshots recording the temporal evolution of the supernova explosion and the resulting remnant from our 3-dimensional ($\sim 10^{51}$ erg) simulation. The contours indicate regions with different densities, while the vectors

Table 5.1. Sgr A East simulation properties

Simulation	Energy (10^{51} erg)	$D_{\text{SgrA}^*}^{\text{min}}$ ^a (pc)	T_{GMC} ^b (y)	Remnant Age (y)
Standard	1.5	0.4	1,200	1,700
Energetic	12	0.2	400	700

^aThe distance of closest approach of the shock to Sgr A*

^bThe time it would have taken for the shock to reach the
50 km s⁻¹ Giant Molecular Cloud

highlight the supernova shock; the dark vectors correspond to the supernova ejecta themselves and the light vectors indicate shocked wind material. The shock collides with and flows around the inner 0.4 pc region primarily along paths of lowest density. It ultimately clears out much of the inner 3 pc region, except for those portions shadowed by the CND or by the outflowing winds from the central 0.4 pc. The depth to which our simulated shock penetrates in the direction of Sgr A* may be checked by simply comparing the ram pressure of the supernova shock with that of the winds. At 430 years, the shock is within $\sim 0.4 - 0.5$ pc of the black hole. The density and velocity of the shock are roughly 3 particles cm⁻³ and 4,000 km s⁻¹, respectively. The corresponding values for the wind outflow are 100 particles cm⁻³ and 700 km s⁻¹. The energy density (or equivalently, the ram pressure, ρv^2) of one flow is equal to that of the opposing flow, and neither makes headway. This roughly marks the time of maximum penetration of the supernova shock, which eventually flows around the central region. By 1,400 years after the explosion, the ram pressure

of the supernova shock decreases below that of the wind, and the latter begins to reassert itself.

In the $\sim 10^{52}$ erg simulation (shown in Figure 5.4 in a similar series of snapshots), the shock moves much faster and penetrates deeper into the stellar wind region surrounding Sgr A*. By 170 years, the shock is within 0.2 pc of the black hole, but as in the standard-energy simulation the shock flows around the dense central region, and even at the distance of closest approach—roughly 270 years after the explosion—the supernova shock never penetrates closer than 0.1 pc from Sgr A*. After 1,200 years, the shock has swept through the entire 3 pc central region, clearing out most of the material except for the CND and the stellar winds, which have begun to reassert themselves beyond 0.4 pc.

Even though the shock doesn't actually reach Sgr A*, it can still affect the medium there, and possibly alter the rate at which matter (and its angular momentum) is accreted onto the black hole. Figure 5.5 shows the accretion rate and accreted specific angular momentum as a function of time for both simulations. Even the high-energy simulation exhibits an increase in accretion rate of less than a factor 2 around the time of closest approach of the supernova shock to the black hole; the standard-energy simulation shows an increase of only $\sim 20\%$. The accreted specific angular momentum shows similar variation; the specific angular momentum accreted in the high-energy simulation jumps by more than a factor 2 for a short period, but the normal-energy simulation shows almost no change at all.

In summary, our simulations demonstrate that even with a $\sim 10^{52}$ erg explosion, a supernova (or “hypernova”, as these rare energetic explosions are often called) does not penetrate all the way to Sgr A* and does not significantly alter the accretion rate. It is difficult to imagine any scenario in which such minor changes in the accretion rate can result in a brightening of Sgr A* by a factor of a million, allowing

it to be the transient irradiator of Sgr B2 several hundred years ago. If Sgr B2 was indeed illuminated by emission at the Galactic center, the source of those X-rays must lie beyond Sgr A*.

5.5 Evolution of the Sgr A East Remnant

As the supernova shock moves outward, it ultimately hits the 50 km s^{-1} molecular cloud behind and to the east of Sgr A*. The last vestige of this interaction is visible now as Sgr A East. However, the dense molecular cloud lies well outside the simulation space of our 3-dimensional calculations. Currently, the inclusion of such a large volume, with the spatial resolution we need in order to produce images such as those shown in earlier figures, is beyond our present computational capability in 3 dimensions.

In this section, we examine the evolution of Sgr A East, focusing on its viability to act as a source for the past illumination of Sgr B2. To do so, we employ a simplified version of the 1-dimensional Lagrangian code developed by Fryer et al. (1999). We include in this code an approximate cooling term, using mean values of the cooling function given in Sutherland & Dopita (1993). We vary the magnitude of this energy loss rate and find, within the range of values given by our temperatures, that the exact value of the cooling rate does not affect our results considerably. What is important, however, is the density profile of the medium through which the shock is propagating.

In their detailed study of molecular gas in the central 10 parsecs of the Galaxy, Herrnstein & Ho (2005) examined the interaction between the Sgr A East shell and the 50 km s^{-1} cloud and concluded that the expansion of the former apparently did not move a significant amount of the latter's mass. This is consistent with the results of our simulation, in which the supernova ejecta at first moved rather quickly

through the medium surrounding Sgr A*, which had been mostly cleared out by the powerful winds of stars situated within $\sim 2 - 3$ parsecs of the black hole. But Sgr A East is clearly interacting with the 50 km s^{-1} cloud now, as evidenced by the presence of seven 1720 MHz OH maser emission regions within several arcmins of the Galactic center (Yusef-Zadeh et al., 1996, 1999). This transition of the OH molecule is a powerful shock diagnostic and is collisionally pumped by H₂ molecules at the site where C-type supernova shocks drive into adjacent molecular clouds. Most of these maser spots are located to the SE of Sgr A*, at the boundary of Sgr A East and M-0.02-0.07. In addition, Zeeman splitting measurements suggest that the magnetic field at these locations is of order $2 - 4 \text{ mG}$. Both the relatively high intensity of this field, and the intense OH maser emission, indicate that the shock at the interface between Sgr A East and M-0.02-0.07 must be very strong, since the impact is compressing the gas and the field lines.

The present interaction region between Sgr A East and M-0.02-0.07 appears to be $\sim 1' - 1.5'$ in projection from Sgr A* (Yusef-Zadeh et al., 1996; Herrnstein & Ho, 2005). At the distance to the Galactic center, this corresponds to $\approx 2.4 - 3.6$ parsecs; taking projection into account, we infer ~ 4 parsecs as a reasonable estimate of the distance between the interaction site and Sgr A*. Thus, with our chosen supernova site 2 parsecs due east (in Right Ascension) of Sgr A*, it would have taken ~ 1200 years for the shock front to reach the molecular cloud traveling at a speed of $v \sim \sqrt{2E_{\text{SN}}/M_{\text{SN}}} \sim 2,500 \text{ km s}^{-1}$.

Figure 5.6 shows several snapshots in time of the velocity of propagation for three 1-dimensional explosion calculations. The basic setup of these models is a diffuse ($n < 10 \text{ cm}^{-3}$) wind-swept region with an outer dense ($n > 10^4 \text{ cm}^{-3}$) molecular cloud, roughly starting at 4 pc. As we would expect from the Sedov blast wave similarity solution (Sedov, 1959; Taylor, 1950), the shock decelerates as

it propagates through the diffuse wind-swept medium. If the diffuse density were higher, the shock would decelerate faster and reach the molecular cloud at a later time. If the explosion energy were higher, the shock would move faster and hence reach the molecular cloud earlier. In all cases, the shock essentially hits a wall at the molecular cloud and bounces back, sending a reverse shock through the diffuse, lower density region.

The energy dissipated when the shock interacts with the molecular cloud can be a significant, albeit transitory, source of high-energy radiation. Supernova remnants interacting with molecular clouds are efficient electron accelerators and sources of hard X-ray and γ -ray emission (Bykov et al., 2000). The energy spectrum of the nonthermal electrons is shaped by various processes, including first and second-order Fermi acceleration in a turbulent plasma, and energy losses due to Coulomb, bremsstrahlung, synchrotron, and inverse Compton interactions. The spectrum produced by these particles between ~ 1 keV and ~ 1 MeV is essentially a power law, $\nu F_\nu \propto \nu^{-\alpha}$, with $\alpha \sim 0.25$. The efficiency of energy transfer from the shock flow to the nonthermal electrons is roughly 5%, though the actual value depends on the velocity of the shock, the density in the cloud, and the radiative efficiency; the efficiency may be lower, but under some conditions, it could be as much as a factor of 2 greater. Since the detailed calculation of the particle acceleration and radiation is beyond the scope of the present work, we will here simply adopt 5% efficiency as the fiducial value, and calculate the overall X-ray/ γ -ray luminosity from the Sgr A East/M-0.02-0.07 interaction site by estimating the shock energy dissipation rate from our 1-dimensional simulation, and assuming that all of the nonthermal particle energy is eventually radiated. We note that with our simplified 1-dimensional simulations, the reverse shock ultimately produces many regions of compression, bouncing backwards and forwards. However, these subsequent shocks are unlikely

to be as strong as the first in the aspherical geometry of the Galactic center. Here, we focus only on the energetics of the first (or leading) impact.

The $\sim 2\text{--}200$ keV luminosity resulting from the interaction we are simulating here is shown as a function of time in Figure 5.7. This light curve is calculated with the conservative assumption, described above, that only 5% of the dissipated energy in the leading shock is converted into photons above 2 keV. Since the 50 km s^{-1} molecular cloud does not completely envelop the Galactic center, we also assume that the interaction site occupies only $4\pi/3$ of solid angle; this estimate is, of course, only a rough approximation, but it does not significantly impact our conclusion.

The result shown in Figure 5.7 clearly establishes the possibility that the interaction between the supernova that created Sgr A East, and the giant molecular cloud, produced the transient X-ray flux whose echo we see today in the Fe fluorescence of Sgr B2. This conclusion comes with several caveats, however, mostly having to do with uncertainties in the overall irradiating luminosity: first, recall that the shock will bounce off of the molecular cloud and send a reverse shock back through the outflowing ejecta, causing the total > 2 keV emissivity to be higher than the value we have calculated here; this is potentially good for the model. Second, when we allow for additional dimensions in the calculation, the shock may flow around the molecular cloud, so the shock in Sgr A East may not be as strong as we find in our 1-dimensional simulation; of course, this will lower the yield of nonthermal particles, and hence the $2 - 200$ keV luminosity. Which of these factors wins out may ultimately determine whether or not this model is correct. Given the level of sophistication of our current calculations, we can only say that both the luminosity and the timing associated with the peak of the dissipation seem to be those required to account for the properties of Sgr B2. Our calculation shows that within the last $\sim 400 - 500$ years, over $10^{39} \text{ erg s}^{-1}$ were released in photons with energy above 2

keV.

It is beyond the scope of the present work to calculate in detail the spectrum of the irradiating flux, but we note from the work of Bykov et al. (2000) that the radiation produced by the nonthermal particles is essentially a power law with flux $F(\nu) \propto \nu^{-0.75}$. Thus, the integrated luminosity in the 2 – 10 keV range should be $\sim 20\%$ of the total. With reference to *Chandra's* spectral band, our predicted X-ray flux is therefore roughly 1/5th the value shown in Figure 5.7. Given that the peak irradiance occurred ~ 400 years ago, the 2 – 10 keV flux level now is therefore consistent with *Chandra's* current measured X-ray luminosity of $\sim 10^{36}$ ergs s^{-1} from the Sgr A East/molecular cloud interaction region. And since our calculated light curve is also a good match to the required illumination of Sgr B2 by a $\sim 2 - 200$ keV spectrum with a peak luminosity of $\sim 10^{39}$ ergs s^{-1} some 300 – 400 years ago (Revnivtsev et al., 2004), we see that both the temporal variation of the high-energy flux, and its associated spectrum, are consistent with all the currently available data.

5.6 Other Constraints on the Recent Galactic Center Supernova

Two uncertainties dominate our solution of the Sgr B2 illumination problem: the supernova explosion itself and the environment through which the explosion traveled. Understanding the environment requires first trying to get a full 3-dimensional structure from observations and then extrapolating that structure backward in time (a process that also requires knowledge of the supernova explosion and its progenitor star). Here, we will instead focus on possible observations that can help constrain the supernova explosion only. In particular, we would like to study the issue of the supernova remnant's age and related issues concerning the origin of the explosion and its energy.

In chapter 4 we found that the structure of the X-ray ridge and its X-ray flux constrained the remnant’s age. They assumed a roughly “standard” (1.5×10^{51} erg) explosion, a radial position of the origin of the supernova set to the radial position of Sgr A*, and a central region whose structure is dominated by the interaction of the stellar winds with the CND and a central supermassive black hole. In this work, we have expanded this study to include a much more energetic $\sim 1.2 \times 10^{52}$ erg explosion. By carrying out a similar study of the X-ray luminosity and shape of the X-ray ridge, we estimate the age of the remnant produced by the strong explosion to be 700 y. It may be difficult to explain the current luminosity of Sgr A East with such a young, strong supernova explosion.

Clearly, the remnant’s age corresponding to either explosion energy is much less than previously thought. But can we place an upper limit on this age? Figure 5.8 shows the 2-10 keV luminosity of the X-ray ridge. Observations of this ridge can be fit with a two-component model to its luminosity: a 1 keV component with a flux of 5.8×10^{-13} erg cm⁻² s⁻¹, and a 5.6 keV component with a flux of 3.92×10^{-13} erg cm⁻² s⁻¹; these fluxes translate to luminosities of 4.4×10^{33} erg s⁻¹ and 3.0×10^{33} erg s⁻¹, respectively, assuming a distance of 8.0 kpc to the Galactic center. If we assume that only the 5.6 keV component is actually associated with the interaction that produces the ridge, we find that the standard simulation matches this luminosity at $\sim 1,700$ y; the energetic simulation matches it at ~ 700 y. A factor 2 uncertainty in the flux would place an upper age limit at $\sim 2,100$ y for the standard explosion and at ~ 900 y for the energetic event.

Such a short remnant age has serious implications on the chemical enrichment from this supernova. The ⁵⁶Ni (which decays into the main iron products of the supernova) is produced only in the inner layers of the star. The explosion quickly develops into a homologous expansion (meaning that the ejecta velocity is propor-

tional to the radius); the iron, produced in the inner layers of the ejecta, is moving slowly. In our standard explosion, it is never moving faster than about 2000 km s^{-1} (in contrast, the highest velocity in the energetic explosion is roughly 6000 km s^{-1}). If the iron moved at this high velocity without decelerating, our standard-energy supernova would not enrich regions in the Galactic center beyond 3.6 pc, but because the iron does decelerate (along with the rest of the shock), this number is closer to 2 pc (Figure 5.9). In the energetic explosion, the iron travels faster and penetrates farther into the Galactic center medium. Indeed, the intermediate weight elements (e.g. silicon and magnesium) have traveled beyond our computational grid boundaries. From Figure 5.9, we see that elements made near the iron layer are, like the iron, limited to a reduced region around the origin of the supernova; elements made further out in the star extend much farther into the surrounding region. In addition, there is a zone shadowed by the stellar winds around Sgr A* that is not enriched at all by the supernova.

There are two major caveats to these abundance plots. First, we have assumed a spherically symmetric explosion and subsequent expansion. But we now know that core-collapse supernovae are far from symmetric (see Hungerford et al., 2003, 2005a, for reviews). Asymmetries in the explosion will allow some iron to mix much further out in the star, and due to the homologous outflow, achieve higher velocities. However, the bulk of the iron will not reach velocities significantly different from what we have obtained in our spherical models. We also did not incorporate into our energetic event the greater yield of heavy elements in a stronger explosion (Hungerford et al., 2005b). The more energetic event could produce a factor 2 more iron, and 10 times more ^{44}Ti , but the basic distribution would remain the same.

The X-ray ridge observations push for a young supernova remnant. Using the X-ray ridge ages, we expect the iron to still be close to the origin of the supernova

explosion (further out for the strong explosion than for the weak explosion). If the remnant truly is 5,000-10,000 y old, the iron should be well mixed all the way into Sgr A*. High resolution abundance maps could both confirm or cast-into-doubt the young age predicted by the X-ray ridge. In addition, such maps could help locate the origin of the explosion. Combined with better models of Sgr A East, such information will also constrain the supernova energy. One way to get this information is to look for evidence of compositional variation in the dust grains and molecular gas in the denser regions: e.g., in the CND, the Northern Ridge, or the Western Streamer (Herrnstein & Ho, 2005). Depending on the supernova energy, age, and location, one or more of these dense regions may be enriched by metals from the supernova itself. For the standard supernova explosion simulation, we expect only the CND to be enriched by iron or even silicon. Since elements like silicon and magnesium are primarily tied up in dust grains, depending sensitively on the physical conditions, accurate abundance measurements may be difficult to obtain.

Emission from radioactive elements is less sensitive to the physical conditions and could also provide some clues. The major intermediate age elements are ^{44}Ti and ^{59}Ni . Unfortunately, for the standard supernova explosion energy, the age of the remnant is so much larger than the ~ 60 y half-life of ^{44}Ti , that the resultant high energy flux from its decay is 10 million times fainter than that of 1987a (for the energetic explosion with its likely higher ^{44}Ti yield and younger age, this value is still a million times fainter than 1987a). This is well beyond any detection limit. However, the ^{59}Ni flux (with its 75,000 year lifetime) could be as high as $2.5 \times 10^{-7} \text{cm}^{-2} \text{s}^{-1}$ (possibly even higher for the energetic explosion). Although beyond detectable limits of current instruments (Leising, 2002), this flux may be observed with an improved generation of high-energy telescopes.

None of these observational constraints are easy to obtain. We provide this

information to encourage and justify experimental and observational programs that might be able to shed more light on this complex problem.

5.7 Conclusions

The fact that Sgr A East had little impact on Sgr A*’s accretion rate as the remnant passed across the Galactic center is of some consequence to the question of how Sgr B2 and other nearby molecular clouds produce their strong fluorescent Fe line emission at 6.4 keV. This puzzle has been viewed as an important indicator of past high-energy activity at the Galactic center, though with very little guidance from gas dynamic studies—until now.

This is where our results from the 3-dimensional and 1-dimensional simulations enter the discussion. One might have thought that the passage of the supernova remnant’s front across Sgr A* could have triggered a significant increase in the rate of gas infall, possibly even producing an enhanced accretion rate onto the black hole to fuel its $\sim 10^6$ factor increase in X-ray luminosity. The implication of this model would be that the supernova shock passed through the Galactic center some 300 – 400 years ago. As we have seen, however, the gas dynamics within the inner 3 – 4 parsecs of the Galaxy negate this possibility, because the strong, cumulative outflux of matter from the interior of the CND prevents Sgr A East from penetrating closer than ~ 0.2 parsecs from Sgr A*. At best, the black hole’s accretion rate could have increased by possibly 20 – 30%, far short of the value required to account for the irradiation of Sgr B2.

Instead, our modeling of Sgr A East’s interaction with the Galactic center has produced what we believe is a far more plausible scenario for the variable illumination of Sgr B2 several hundred years ago. As we saw earlier, the remnant’s shock front apparently reached the Galactic center some 160 years after the supernova

explosion, and swept around the inner $0.2 - 0.3$ parsec region in ~ 650 years. Our modeling of the X-ray ridge NE of Sgr A* suggests that we are viewing the interaction between the remnant and the winds flowing out from the ionized cavity $\sim 1,700$ years after the supernova event. There is strong observational evidence that Sgr A East is now also interacting with the so-called 50 km s^{-1} molecular cloud behind Sgr A* (Yusef-Zadeh et al., 1999). But this interaction should have produced an intense X-ray/ γ -ray glow when the impact first occurred, due to the initial rapid dissipation of kinetic energy flux into heat, nonthermal particle acceleration and radiation. Given the proximity of the supernova event site to the Galactic center (only several parsecs away from Sgr A*), the ensuing irradiation of Sgr B2 would still show the tell-tale characteristics of a Galactic center source, albeit now a diffuse X-ray/ γ -ray emitter, rather than a point source associated directly with Sgr A*. The key constraint is that Sgr A East's X-ray/ γ -ray glow should not have ended more than ~ 400 years ago—approximately $1,350$ years after the supernova explosion—this being the light travel time between the interaction site and Sgr B2.

There may even be related evidence that the X-ray/ γ -ray glow may have persisted closer to the present time, perhaps to within the past 100 or 200 hundred years. In their analysis of Sgr A East and its X-ray properties, Maeda et al. (2002) showed that the ionized gas halo into which Sgr A East is currently expanding (i.e., in regions other than where it is colliding with the 50 km/s cloud) may have been ionized by the same irradiator that produced the current fluorescence in Sgr B2. For an ambient gas density $\sim 10^3 \text{ cm}^{-3}$, the required luminosity would have been $\sim 10^{40} \text{ ergs s}^{-1}$, but since the recombination time in such a gas is shorter than ~ 300 years, the (still) high ionization fraction in the ISM argues for a period of irradiation extending to well within 300 years of the present. However, the current X-ray luminosity from the Sgr A East shell, including the region of interaction with

the 50 km/s cloud, places a rather severe constraint on how rapidly the X-ray/ γ ray glow must have subsided to its present value. This 2 – 10 keV limit is $\approx 10^{36}$ ergs s^{-1} , if we take the whole shell into account. A reduction in the solid angle subtended by the interaction zone at the site of the explosion would lower this level even further.

The circumstantial evidence for a youthful Sgr A East remnant is building. We now have several observational indicators that self-consistently point to the explosion occurring not more than $\sim 1,750$ years ago. These include the current morphology and X-ray luminosity of the Ridge, the diffuse X-rays from the central 2 – 3 parsecs, which apparently point to stellar winds as the sole contributors to the ISM within the cavity, and the timing and 2 – 200 keV luminosity associated with the remnant's interaction with the 50 km s^{-1} molecular cloud, which apparently irradiated Sgr B2 and, possibly, the ionized halo surrounding the Galactic center several hundred years ago.

On the theoretical plane, several additional steps remain to be taken. These include a more thorough examination of the nonthermal particle injection and radiation at the remnant-cloud interface, and a subsequent analysis of the time-dependent spectrum illuminating Sgr B2 and other nearby clouds. Eventually, when the necessary computational resources become available, it would be very helpful to redo these calculations in 3 dimensions. Observationally, this work would benefit from a high resolution mapping of the metal abundances surrounding the explosion site. The morphology of this distribution should be directly coupled to the energetics of the explosion and the age of the remnant.

Figure 5.3 Simulated density contours from the 1.5×10^{51} erg explosion. Time series of a 0.2 pc slice centered on Sgr A* from our simulation of a 1.5×10^{51} erg explosion. Contours show density (same as Fig. 5.2). The vectors show the shock (black denotes supernova ejecta, red is the front of the shock composed of accelerated wind material). Note that the shock flows around the dense central region surrounding Sgr A* but does not penetrate closer than 0.4 pc from the black hole. The deepest penetration occurs at 650 y. At 1,400 y the shock has cleared out most of the central 3 pc. However, the region shadowed by the central 0.4 pc surrounding Sgr A* is not cleared. By 1,740 years the wind material has begun to reassert itself and is expanding back into the supernova ejecta.

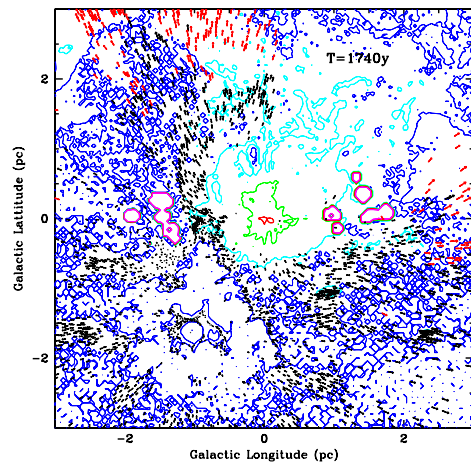
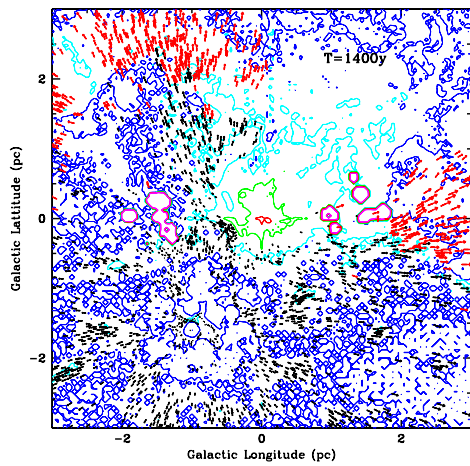
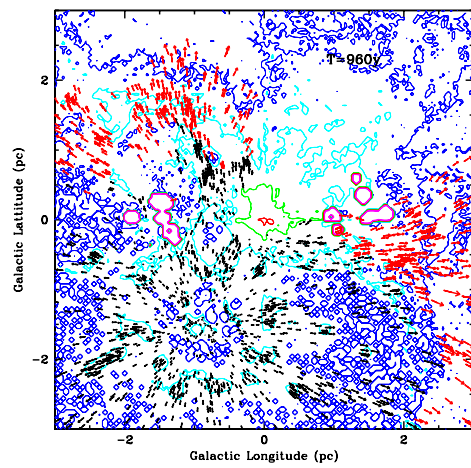
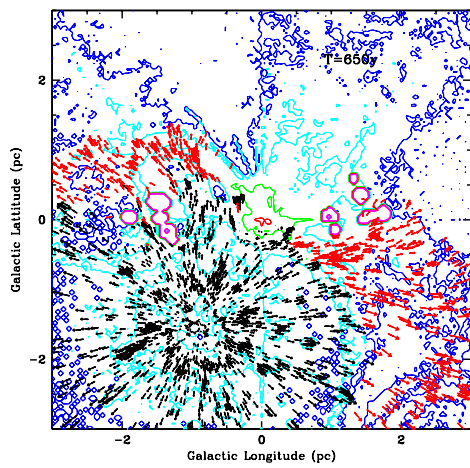
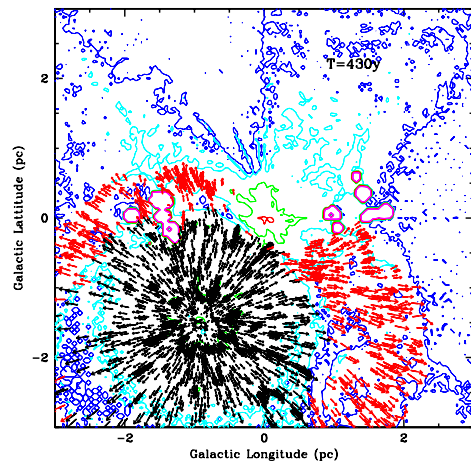
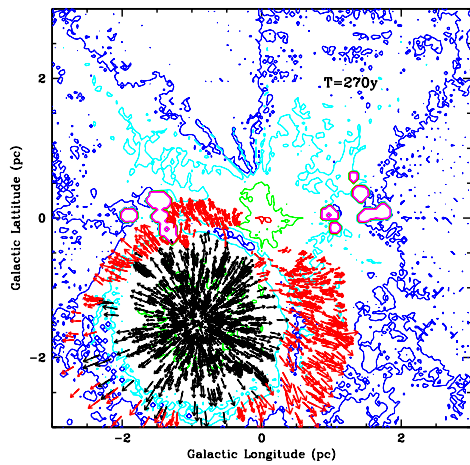
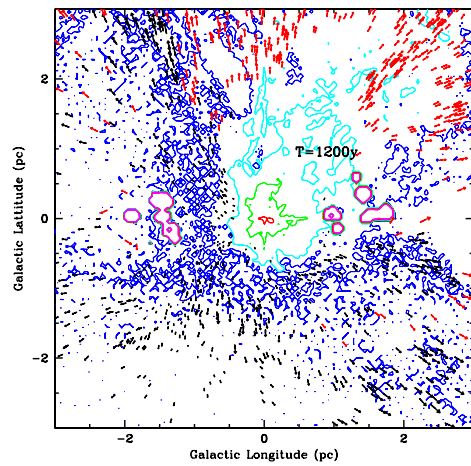
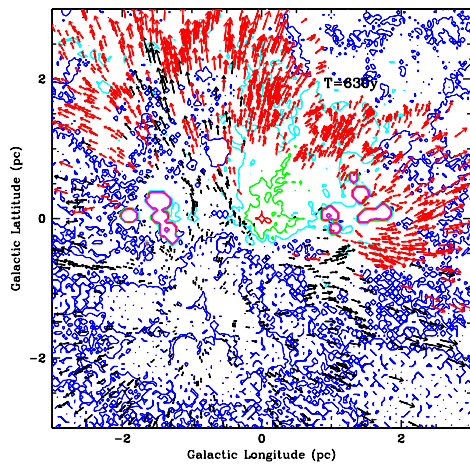
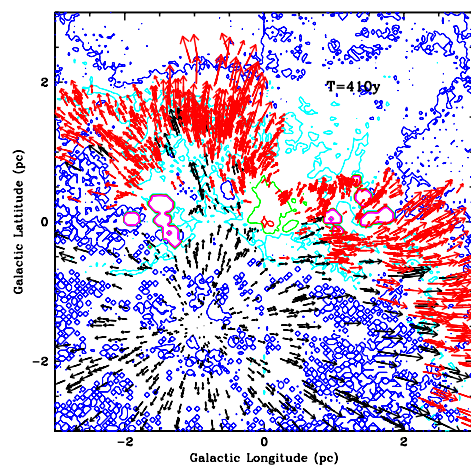
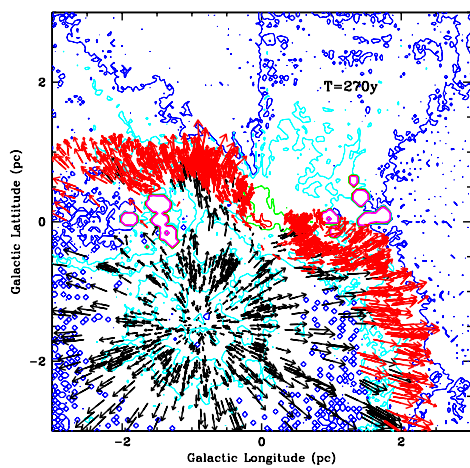
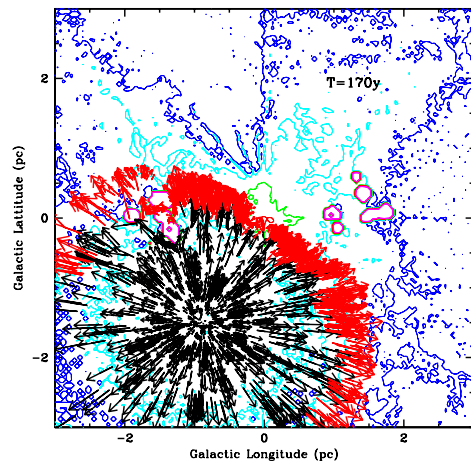
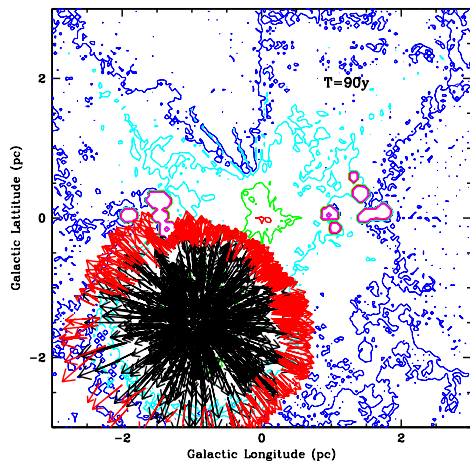


Figure 5.4 Simulated density contours from the 1.2×10^{52} erg explosion. Same as Fig. 5.3, but now for the 1.2×10^{52} erg explosion. The shock penetrates to within 0.1-0.2 pc of Sgr A*, reaching maximum penetration at only 200-270 years. It clears out the Galactic center more comprehensively than the $\sim 10^{51}$ erg explosion, but some material is still shadowed by the dense stellar wind region surrounding Sgr A*. By 1,200 years, the stellar winds have begun to reassert themselves.



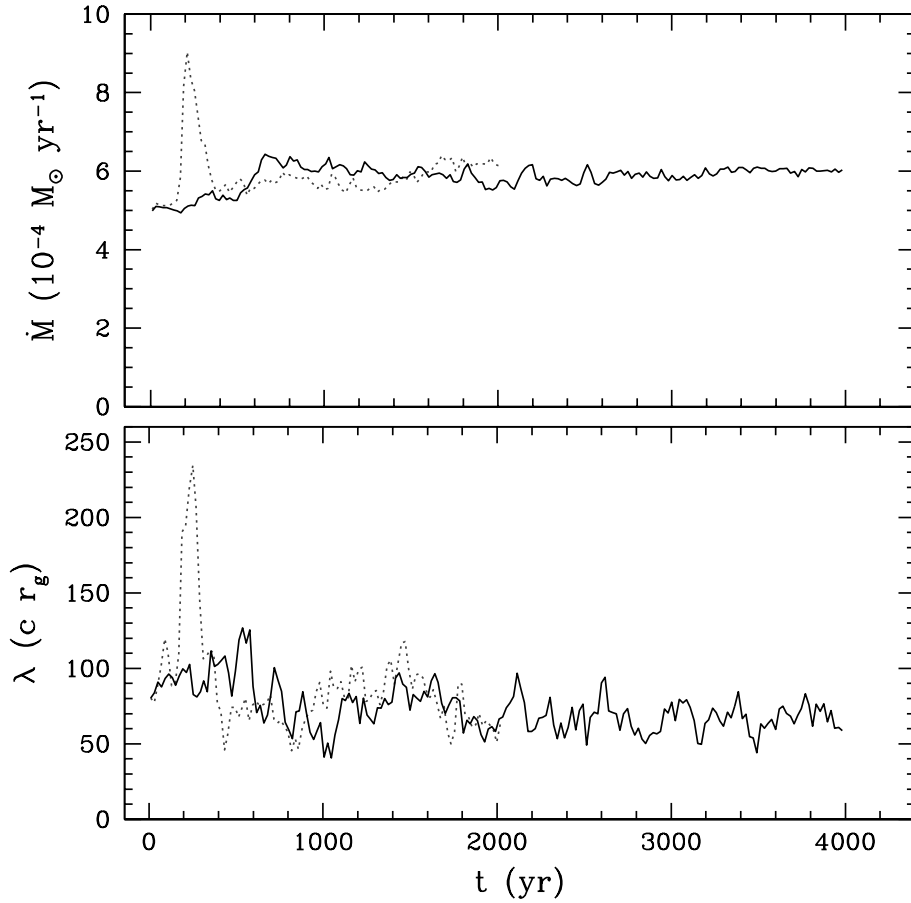


Figure 5.5 Accretion rate and accreted specific angular momentum. The mass accretion rate (top) and accreted specific angular momentum (bottom) as functions of time for the standard (solid line) and energetic (dotted line) simulations. The standard simulation undergoes a small ($\sim 20\%$) change in accretion rate around the time of closest approach of the supernova shock to Sgr A* (~ 650 yr), while the energetic simulation shows an increase in \dot{M} of nearly a factor 2 for a short period of time. Similarly, the accreted specific angular momentum (λ , in units of $c r_g$, where $r_g \equiv GM/c^2$) changes by $\lesssim 20\%$ in the standard simulation, but undergoes a brief increase of more than a factor 2 in the energetic simulation.

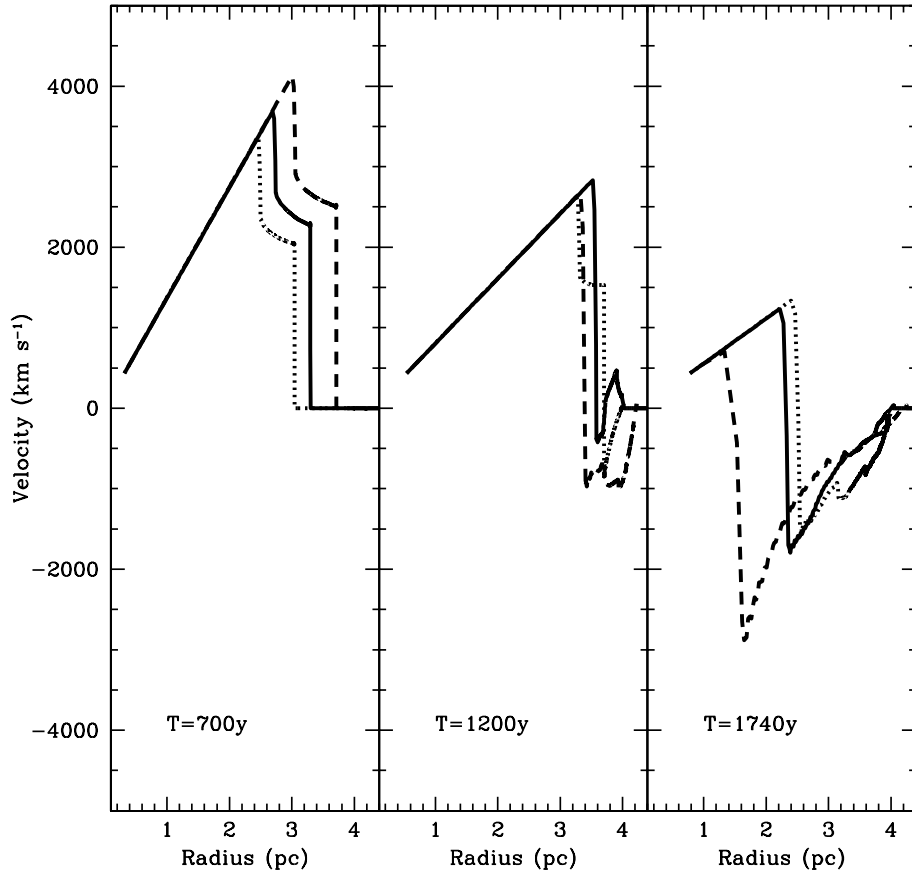


Figure 5.6 Velocity radial profiles. Velocity versus radius at 3 snapshots in time from our 1-dimensional simulation, modeling the encounter of the supernova shock with the surrounding 50 km s^{-1} molecular cloud. The solid line denotes our standard model, which is essentially a 1-dimensional spherical version of the 1.5×10^{51} erg supernova explosion modeled in our 3-dimensional simulation. We assume a 4 pc windswept medium (with density $n = 1 \text{ cm}^{-3}$) surrounded by a dense ($n = 10^4 \text{ cm}^{-3}$) molecular cloud. The dotted line is the same explosion, but with a slightly higher density in the windswept medium ($n = 2 \text{ cm}^{-3}$) and a gradient in the molecular cloud density rising ultimately up to $n = 10^5 \text{ cm}^{-3}$. The dashed line is an explosion with a 20% increase in energy, and a 4.2 pc windswept region, but with the same densities as in our standard model.

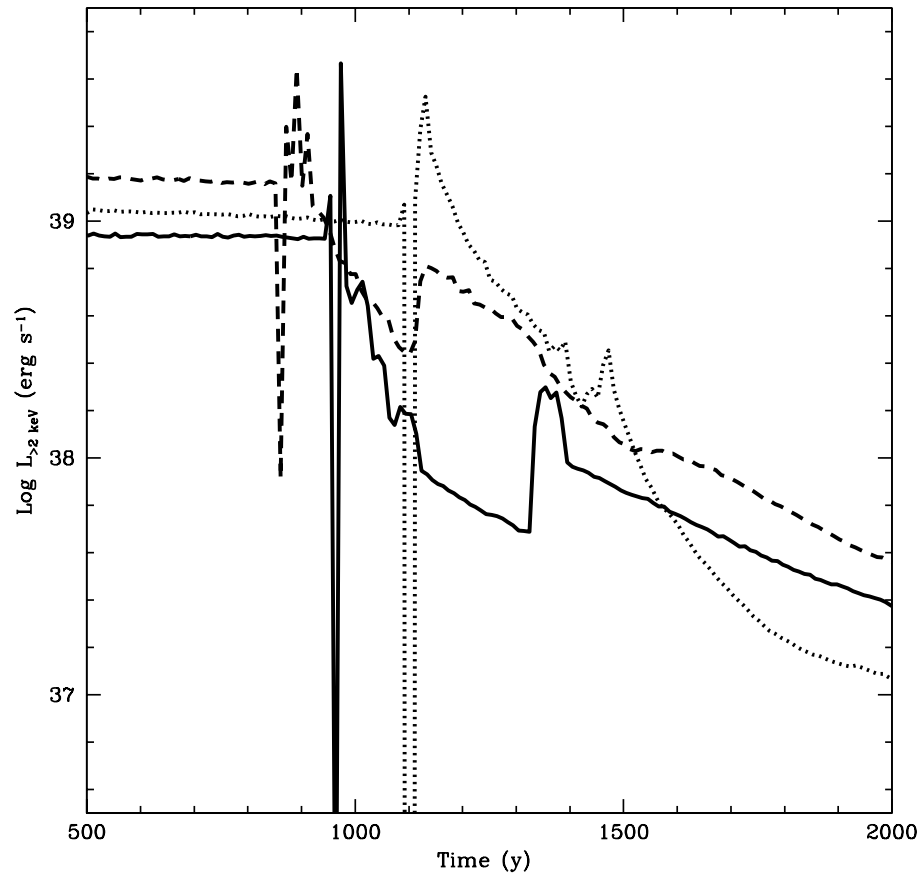


Figure 5.7 Simulated high-energy emission. The 2 – 200 keV luminosity versus time for the 3 shock models shown in Figure 5.6. Our best-fit model, with a slightly increased density in the windswept region and a density gradient (dotted line), produces considerable high energy emission (enough to illuminate Sgr B2) up to 400 years ago (assuming the supernova remnant is 1,700 years old), yet the high energy flux has decreased significantly by the current epoch. Note that the 2 – 10 keV flux is $\sim 20\%$ of this total (i.e., bolometric) high energy value. Geometric effects, ignored in these spherically symmetric simulations, will alter these results somewhat, but these calculations do establish the plausibility of a model in which Sgr A East illuminated Sgr B2 when it first encountered the giant molecular cloud.

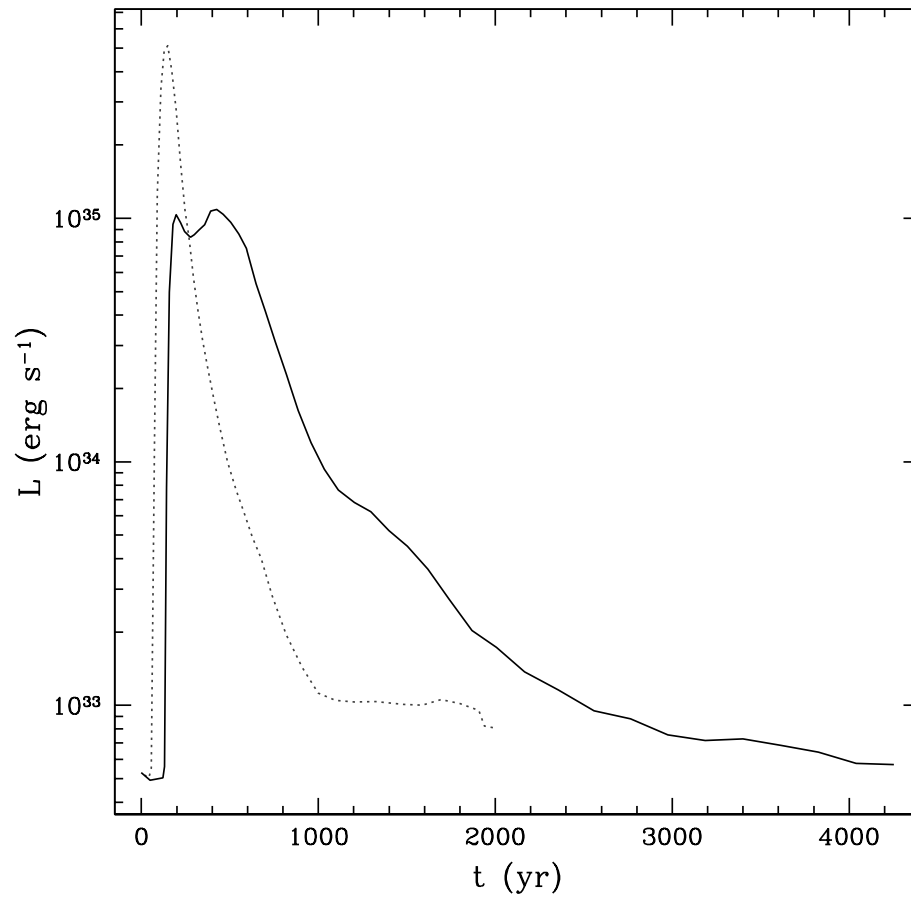


Figure 5.8 X-ray luminosity from simulated arc toward Sgr A East. The 2–10 keV X-ray luminosity from a 170° arc on the simulated sky between $9''$ and $15''$ to the east of Sgr A* (toward the supernova). The solid line shows the 2–10 keV luminosity from the standard simulation; the dotted line shows the luminosity from the energetic simulation.

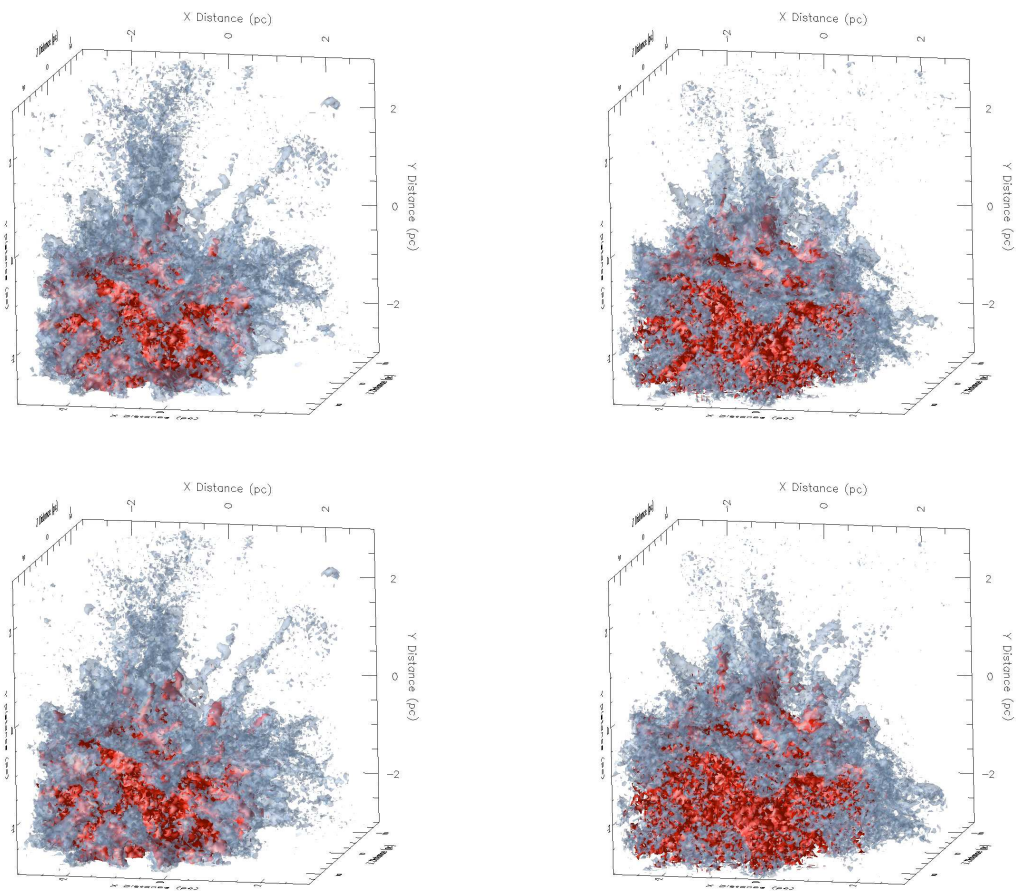


Figure 5.9 Isosurfaces of nickel, iron, titanium, and magnesium. Abundance plots for both the standard (left column) and energetic (right column) explosions. The top panels show the nickel (iron) abundance surrounded by the silicon abundance. Note that at this time, because the silicon was produced further out, it had a higher expansion velocity and has therefore mixed further out. The silicon-to-iron ratio should be much higher than typical solar abundances at these larger distances. The bottom panels show the inner titanium (made in the outer part of the region where the iron is made) surrounded by the magnesium abundance for comparison.

CHAPTER 6

SPIN-INDUCED DISK PRECESSION IN SAGITTARIUS A*

6.1 Introduction

At the Galactic center, the compact radio source Sgr A* appears to be the radiative manifestation of an accreting $3.7 \times 10^6 M_\odot$ supermassive black hole (Ghez et al., 2005). Its radio to mm spectrum is thought to be a composite of two principal components—a slightly inverted power-law with a notable bump at mm/sub-mm wavelengths. The latter is somewhat reminiscent of the “big blue bump” seen in many Active Galactic Nuclei (AGNs), evidently produced by an accretion disk feeding the supermassive black hole (see, e.g., Brotherton et al., 2001). But unlike the blackbody emission process that gives rise to the optical/UV thermal feature in an AGN spectrum, the radiative mechanism responsible for Sgr A*'s mm/sub-mm spectral excess appears instead to be a combination of thermal and non-thermal synchrotron emission within the inner portion ($r < 10 r_S$) of a hot, magnetized Keplerian flow (Melia et al., 2001; Liu & Melia, 2001). (The Schwarzschild radius, r_S , for an object of this mass M is $2GM/c^2 \approx 10^{12}$ cm, or roughly 1/15 A.U.) The inferred characteristics of the compact region surrounding Sgr A* are also consistent with the $\sim 10\%$ linear polarization detected from this source at mm wavelengths (Melia et al., 2000; Bromley et al., 2001). Given the complex spatial arrangement of the mass-losing stars that feed this object, it is unlikely that the disk angular momentum axis is aligned with the spin axis of the black hole.

The possible (but currently unconfirmed) detection of a 106-day cycle in the radio signal from Sgr A* (Zhao et al., 2001) has added significant intrigue to this

picture, since it may indicate precession of the disk induced by the spin of the black hole (Liu & Melia, 2002b). The dynamical time scale near the marginally stable orbit around an object with this mass is ≈ 20 minutes. Thus, since the physical conditions associated with the disk around Sgr A* imply unwarped, coherent precession, a precession period of 106 days may be indicative of a small black-hole spin ($a \sim 0.1$) if the circularized flow is confined to a region within $\sim 30 r_S$. (Throughout this chapter, we define a to be the black hole angular momentum divided by GM^2/c .) The precession of a larger structure at the same rate would require a bigger black hole spin; alternatively, for a given black hole spin, a larger disk would precess with a longer period. Liu & Melia (2002b) also noted that a small value of a (< 0.1) would be favored if the non-thermal ($\sim 1 - 20$ cm) portion of Sgr A*'s spectrum is powered with energy extracted via a Blandford-Znajek type of process, for which the observed luminosity would correspond to an outer disk radius $r_{out} \sim 30 r_S$. In addition, a small disk size was suggested by earlier hydrodynamical and magnetohydrodynamical simulations (Coker & Melia, 1997; Igumenshchev & Narayan, 2002), and is implied by Sgr A*'s spectral and polarimetric characteristics.

For a thin, cold disk, the differential Lense-Thirring precession dominates the internal coupling of the plasma at small radii and therefore leads to the so-called Bardeen-Petterson effect (Bardeen & Petterson, 1975), in which the inner region flattens toward the equatorial plane, producing a warped accretion pattern. As shown by Nelson & Papaloizou (2000) and confirmed recently by Fragile & Anninos (2005), however, thicker disks with a mid-plane Mach number of ~ 5 or less can suppress warping effects due to the coupling provided by pressure gradients and viscosity in the gas. The mid-plane Mach number in Sgr A* is ~ 3 (for detailed comparisons of model disks to observations, see, e.g., Melia et al., 2001; Igumenshchev & Narayan, 2002), so it seems that the disk in this system may be precessing as one unwarped

structure (Liu & Melia, 2002b). In this chapter, we report the results of smoothed particle hydrodynamics (SPH) simulations we have carried out to test these ideas at a higher level of sophistication than was attempted earlier by Liu & Melia (2002b).

6.2 Physical Principles and Method

We evolve gaseous disks in the gravitational potential of the black hole at the Galactic center using the three-dimensional smoothed particle hydrodynamics (SPH) code described in Fryer et al. (2006a). The inner boundary of the calculation is placed at a radius corresponding to the innermost stable circular orbit, as a function of a . For simplicity in this first generation of calculations, particles crossing the inner boundary carry all of their mass and angular momentum into the black hole, and no additional infalling material enters the simulation at the outer edge of the disk; we also do not model the magnetic field or evolve the equations of magnetohydrodynamics, but we include a prescription for the role of the magnetorotational instability in transporting angular momentum (see below). In principle, infalling material can exert an additional torque on the disk with a tendency to align the disk's angular momentum vector with that of the accreting plasma. However, the angular momentum flow through the disk is also subject to magnetic coupling effects at its inner boundary (Krolik & Hawley, 2002), which can either offset or enhance the effect of the external torque, depending on the configuration of the magnetic field (see Liu & Melia, 2002b). We do not fully explore the range of inner and outer boundary conditions in this first treatment and instead leave this important survey to future publications. Consequently, our simulated disks mediate an outward viscous transport of angular momentum, which causes them to slowly grow in radius.

We construct disks based on current estimates of flow properties in the Galactic

center (Melia et al., 2001), and we incorporate important effects of general relativity in a Kerr metric and an anomalous viscosity due to the magnetorotational instability that the observations strongly indicate is active in this system. The gravomagnetic force per unit mass and the anomalous viscosity dominate the dynamics of the disk; even at its turbulent saturation point, the magnetic field energy represents only about 15 percent of the equipartition value. Since the adoption of a post-Newtonian approach to handle the general relativistic effects (see below) introduces ~ 10 percent errors, it is reasonable to ignore the dynamical impact of the magnetic field for the first set of simulations. Advancing this study to the next level of sophistication will entail the use of a more elaborate magnetohydrodynamic treatment, which is currently in development. In the final analysis, we will indeed follow the evolution of the inner disk in Sgr A* with all effects included in the simulation: the magnetic field and associated anomalous viscosity and the gravomagnetic force per unit mass. The calculations we describe here will provide a powerful baseline against which the later calculations may be compared and tested.

6.2.1 The Conservation Equations and SPH Code

Since the physical effect simulated here occurs many Schwarzschild radii from the black hole, we follow Nelson & Papaloizou (2000) and include the relativistic effects only in a post-Newtonian approximation. Our momentum equation therefore takes the form

$$\frac{d\vec{v}}{dt} = -\frac{1}{\rho}\vec{\nabla}P + \vec{v} \times \vec{h} - \vec{\nabla}\Phi + \vec{F}_{visc}, \quad (6.1)$$

where ρ is the density, \vec{v} is the velocity, P is the pressure, Φ is the gravitational potential, and \vec{F}_{visc} is the viscous force per unit mass. The term $\vec{v} \times \vec{h}$ is the lowest-order post-Newtonian approximation to the gravomagnetic force per unit mass near

a rotating black hole (see, e.g., Blandford, 1996). In this equation, \vec{h} is defined as

$$\vec{h} \equiv \frac{2\vec{S}}{r^3} - \frac{6(\vec{S} \cdot \vec{r})\vec{r}}{r^5}, \quad (6.2)$$

where

$$\vec{S} = \frac{G\vec{J}}{c^2} \quad (6.3)$$

in terms of the (cylindrical) coordinate vector $\vec{r} = (\eta, \phi, z)$, and $r = |\vec{r}|$. The spin angular momentum of a Kerr black hole (using our definition of a ; see above) is given by

$$\vec{J} = \frac{aGM^2}{c} \hat{k}, \quad (6.4)$$

where \hat{k} denotes the unit vector in the z -direction. We calculate the gravitational acceleration due to the black hole using

$$-\vec{\nabla}\Phi = -\frac{GM}{r^3} \left(1 + \frac{6r_g}{r} \right) \vec{r} \quad (6.5)$$

(where $r_g \equiv r_S/2 = GM/c^2$), which produces the correct apsidal precession frequency at large distances from the black hole (Nelson & Papaloizou, 2000).

We use an equation of state of the form $P = K\rho^\gamma$ —where P is the pressure, $\gamma = 5/3$ is the heat capacity ratio, and K is a constant chosen to set the midplane Mach number. Energy dissipated through artificial viscosity is allowed to leave the system.

6.2.2 The Anomalous Viscosity

Many of the properties derived by Balbus & Hawley (1991, 1992) for weakly magnetized accretion disks appear to be present in Sgr A*. One of the most important defining characteristics is the existence of an anomalous viscosity arising from the Maxwell stress, which in Sgr A* easily dominates over the Reynolds stress. In our calculations, we model the effect of this anomalous viscosity using the α -disk

prescription

$$\nu = \frac{\alpha c_s^2}{\Omega}, \quad (6.6)$$

where c_s is the local sound speed and Ω is the Keplerian angular velocity. Earlier quasi-analytical fits to Sgr A*'s spectrum, and analysis of X-ray flares detected from this object by *Chandra* (Liu & Melia, 2002a) concluded that the ratio β_0 of Maxwell stress to thermal pressure is $\simeq 0.05$; since the viscosity ν can also be written as

$$\nu = \frac{2}{3} \frac{\beta_0 c_s^2}{\Omega}, \quad (6.7)$$

we relate α and β_0 using $\alpha = (2/3)\beta_0$ and find that α should be approximately 0.03 in our model disks.

We implement the viscosity using the same technique used by Nelson & Papaloizou (2000), i.e., we adjust the bulk viscosity coefficient α_{SPH} and the Von Neumann-Richtmyer viscosity coefficient β_{SPH} of the standard SPH artificial viscosity prescription. Following Nelson & Papaloizou (2000), we set $\alpha_{SPH} = 0.5$ and $\beta_{SPH} = 0.0$. By tracking the motion of particles in our calculations, measuring the ratio of orbital period P to accretion timescale τ_{acc} , and relating the ratio of timescales to the viscosity parameter $\alpha \simeq P/\tau_{acc}$, we find that a value of $\alpha_{SPH} = 0.5$ corresponds to a value of $\alpha \simeq 0.02$.

6.3 Results

The characteristics of the three simulations we ran that directly address the questions we wish to answer in this chapter are summarized in Table 6.1. Simulation E1 is a direct comparison with the calculation of the same name reported by Nelson & Papaloizou (2000). Simulation GC20 was constructed with an initial outer radius of $20 r_S$; the parameters of this model were chosen to be fully consistent with the physical conditions outlined above. It is the contrast between this model and E1

Table 6.1. Galactic Center disk simulation properties

Simulation	i^a (deg)	a^b	\mathcal{M}^c	R_{init}^d (r_S)	N_{init}^e
E1	10	1	12	25	327357
GC20	30	0.1	3	20	475671
GC30	30	0.1	3	30	757337

^aInclination angle

^bBlack hole spin parameter in units of GM^2/c

^cMid-plane Mach number

^dInitial disk outer radius

^eInitial number of SPH particles

that we expect to highlight the difference between the behavior of a cold disk that is subject to the Bardeen-Petterson effect and the low-Mach-number disk that we believe is present at the Galactic center; according to earlier semi-analytical analysis, the Galactic center disk ought not to experience this effect. However, because we have chosen not to feed the disk from outside, the viscous transport of angular momentum leads to a slow growth in its size; to test the dependence of the disk's temporal behavior on the initial conditions, we also carried out simulation GC30, which has an initial size of $30 r_S$ and is otherwise identical to GC20.

Figure 6.1 shows the 3-D arrangement of SPH particles in our reproduction of test E1 by Nelson & Papaloizou (2000). In this image, the black hole spin axis

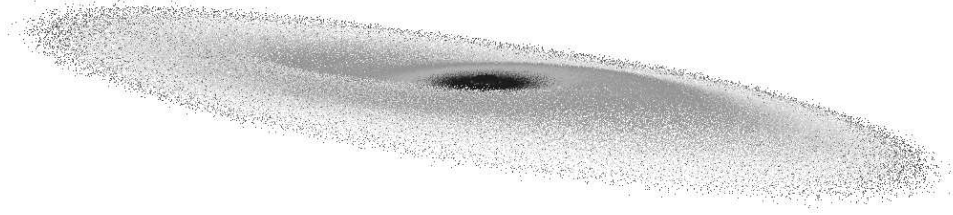


Figure 6.1 SPH particles in a simulated warped disk. The 3-D arrangement of 326,034 SPH particles in a reproduction of test E1 of Nelson & Papaloizou (2000). The inner portion of the inclined disk is warped into the equatorial plane of the black hole (aligned horizontally in the image) through the action of the Bardeen-Petterson effect.

points in the vertical direction. The outer portion of the disk has maintained its original 10-degree inclination relative to this direction. However, due to the Bardeen-Petterson effect, the inner portion of the disk has become warped and now lies in the equatorial plane of the black hole. By this time in the simulation, which corresponds to 4 Keplerian orbital periods at $r = 25 r_S$, the transition region between the outer inclined portion of the disk and the inner warped portion has stabilized at a radius of $7 r_S$, in good agreement with Nelson & Papaloizou (2000).

In contrast, a disk constructed according to the best estimates for conditions in the Galactic center does not warp; instead, the entire disk remains tilted out of the equatorial plane and precesses around the spin axis of the black hole. Figure 6.2 shows the 3-D arrangement of SPH particles in simulation GC30 after 85 Keplerian

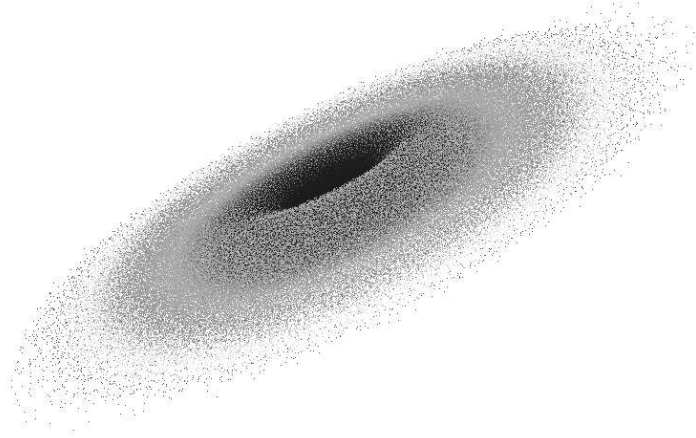


Figure 6.2 SPH particles in a simulated Galactic Center disk. The 3-D arrangement of 423,626 SPH particles in a simulated disk constructed using the gas temperature and density, constrained by the observations, in the environment near the black hole at the Galactic center. The disk is relatively thick, so the Bardeen-Petterson effect is suppressed; even the innermost portion of the disk remains aligned with the outer disk and is not warped into the equatorial plane of the black hole.

orbits at $30 r_S$, when the disk has an outer radius of $55 r_S$; the central portion of the disk lies in the same plane as the rest of the disk, and not in the equatorial plane of the black hole. Nelson & Papaloizou (2000) also considered one case in which the midplane Mach number was low (specifically, $\mathcal{M} = 5$) and found that that particular disk did not warp. Our result for model GC30, which has a midplane Mach number of 3, is consistent with their finding. Simulation GC20 behaves in exactly the same way. A principal result of this work is that the physical conditions inferred from Sgr A*'s spectrum evidently imply that the entire disk precesses coherently around the black hole spin axis, confirming the prediction of Liu & Melia (2002b).

An important observational signature of this effect is the dependence of the

precession period on the size of the disk for a given value of the black hole spin parameter. The size of the disk provides a measure of the moment of inertia of the structure, whose response to the applied gravomagnetic torque determines the rate of precession.

Liu & Melia (2002b) argued that the precession period of a coherent simplified model disk should vary as $r_{out}^{5/2}$, under the assumption that the surface density in the disk is constant. To test this predicted dependence, we evolved the disk over many orbital periods, tracing its growth in size and corresponding change in precession period; the relationship is summarized in Figure 6.3. Note that the disk radius plotted along the horizontal axis is actually the radius of the thickest portion of the disk, not the radius of the outermost particle in the simulation. The low number density of particles at the outer disk edge inhibits a consistent and accurate determination of what actually constitutes the disk size; choosing the radius where the disk is thickest, on the other hand, provides a more stable and reliable determination of the disk size.

Starting with an outer radius of $20 r_S$, and assuming that $a = 0.1$ (see Table 1), the precession period is 69 days. The period grows smoothly and monotonically as the disk expands under the action of viscous angular momentum transport and reaches approximately 600 days when the outer radius is $46 r_S$. In this figure, the solid curve indicates the calculated behavior of the period as a function of outer disk radius; the dashed curve gives a strict $P \propto r_{out}^{5/2}$ dependence. Our simulations clearly exhibit a period that varies as $r_{out}^{5/2}$; this is a consequence of the fact that our GC20 and GC30 disks precess as coherent structures.

Future work will include the effect of infalling material and a more thorough survey of the dependence of disk evolution on black hole parameters such as a . Very importantly, we will study another potentially significant signature: the prograde-

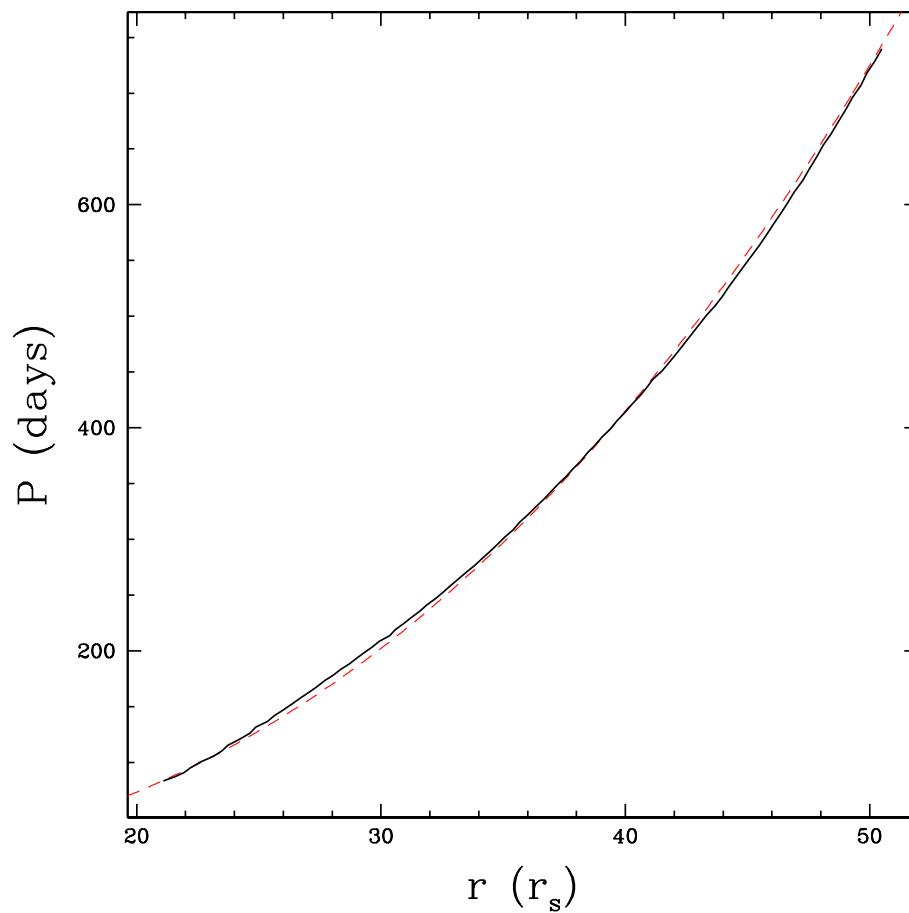


Figure 6.3 Precession period versus disk size. The precession period of the simulated Galactic center disk versus the size of the disk. The solid curve, measured from the simulation, matches the $P \propto r^{5/2}$ relationship (shown as a thin dashed line) predicted by Liu & Melia (2002b), demonstrating that a disk formed in the Galactic center likely does precess as one coherent, unwarped structure.

retrograde flip that might occur due to sudden changes in the accreted angular momentum L . Past hydrodynamic simulations (Coker & Melia, 1997) have hinted that the complex, clumpy structure of the infalling plasma can lead to significant fluctuations in both the magnitude and direction of L .

6.4 Conclusions

We find that the physical conditions associated with accretion onto Sgr A* imply the presence of a compact accretion disk that precesses as a coherent, unwarped structure about the black hole spin axis. Our simulations confirm the general results of Nelson & Papaloizou (2000); specifically, we find that the low-Mach-number disk in Sgr A* would not be subject to the Bardeen-Petterson effect. Given the observed constraints on disk parameters, we provide an accurate determination of the precession period of such a disk. The fact that this period varies as $r_{out}^{5/2}$ may eventually lead to a compelling determination of the black hole spin; alternatively, if other independent techniques or observations can provide accurate estimates of the spin, our results determine the radius of the disk around Sgr A*.

Observationally, our work provides some motivation for expecting a modulation in Sgr A*'s flux with a period of $\sim 50 - 500$ days; we have found that the precession period is in this range as long as the disk size is $\sim 20 - 30 r_S$. Such a modulation might arise in portions of Sgr A*'s spectrum produced by an occulted emitter; for example, it is known that Sgr A*'s radio emission is produced on scales of $20 - 100 r_S$ (see, e.g., Bower et al. 2004). Thus, since this disk is optically thick to cm radiation (Liu & Melia, 2002b; Prescher & Melia, 2005), its precession may lead to a variable aspect that periodically attenuates the total radio flux from this region.

This effect may already have been observed; Zhao et al. (2001) report a detection of a ~ 106 -day cycle in Sgr A*'s radio emission. If this result is eventually confirmed,

and if indeed it appears that only a disk precessing in a non-isotropic gravitational field can account for it, we may eventually be able to use it as a probe of the spacetime within the inner $\sim 10 r_S$ of a Kerr metric and, more importantly, as a means of directly measuring the black hole's spin.

On the other hand, a non-confirmation of such a modulation on a $\sim 50 - 500$ -day timescale would tell us that either no disk is present in Sgr A* or that its properties—specifically, its size and orientation—are different from what we now understand, or that the geometry of the emission region has not yet been identified. The fact that such a determination can be made points to the predictive power of detailed numerical simulations like those reported here and argues for the need for more sophisticated calculations incorporating the effects we have ignored thus far.

APPENDIX A

SMOOTHED PARTICLE HYDRODYNAMICS: ALGORITHM AND CODE DETAILS

A.1 Introduction

The simulations presented in this dissertation were performed using the grid-less Lagrangian hydrodynamics algorithm known as smoothed particle hydrodynamics (SPH). The particular code used is a version of the radiation hydrodynamics code SNSPH. SNSPH uses smooth particle hydrodynamics (SPH) to model the Euler equations and a flux-limited diffusion package to model radiation transport. It is built around a treecode which accelerates the calculation of gravitational forces and the neighbor-finding operations that are common in SPH. The tree algorithm is designed for fast traversal on parallel systems (Warren & Salmon, 1993, 1995) and has been shown to scale well up to high processor number (> 1024 processors) on a wide variety of computer architectures.

The sections below describe the components of SNSPH that were used in the Galactic center simulations. In addition to the components described here, SNSPH includes a radiation (specifically, neutrino) transport module that implements a flux-limited diffusion algorithm, and an equation of state appropriate for the densities and temperatures encountered in stellar cores in supernova and gamma-ray burst simulations.

A.2 Physics Implementation

In this section, we describe the physics algorithms incorporated into the Galactic-center variant of SNSPH.

A.2.1 Gravity

Newton’s second law of motion and law of gravitation provide an expression for the acceleration of one body under the combined gravitational influence of a set of $N - 1$ other bodies, according to

$$\frac{d^2 \vec{x}_i}{dt^2} = \sum_{j \neq i}^N \vec{a}_{ij} = \sum_{j \neq i}^N \frac{Gm_j \vec{r}_{ij}}{|\vec{r}_{ij}|^3}, \quad (\text{A.1})$$

where $\vec{r}_{ij} \equiv \vec{x}_i - \vec{x}_j$. Using this equation to calculate the acceleration for one body requires $N - 1$ evaluations of the term inside the sum, so determining the accelerations of all N bodies in a simulation requires $N(N - 1)$ or $O(N^2)$ operations. Performing this type of pairwise summation to calculate gravitational interactions is prohibitively expensive for all but the smallest sets of bodies, even on the fastest supercomputers.

A number of approximate methods have been developed to calculate gravitational forces among large numbers of bodies by considering as one interaction the total effect of a set of bodies on one body, or the effect of one set of bodies on another set, with time requirements that scale as $O(N \log N)$ or $O(N)$, respectively. Codes that use adaptive tree structures to subdivide the volume of a simulation and distinguish between nearby and distant bodies can easily implement such accelerated techniques; our code uses such a tree and is therefore one of a class of codes called “treecodes”. This class includes many SPH codes such as Gadget (Springel et al., 2001) and Gasoline (Wadsley et al., 2004) as well as particle mesh codes (Suryadeep, 2004) and some Adaptive Mesh Refinement (AMR) codes such as RAGE (Coker et al., 2006).

Knowledge of the spatial arrangement of bodies in a simulation allows the tree-code to distinguish between “nearby” bodies, for which direct pairwise calculation of gravitational forces is necessary, and “distant” bodies, for which an approximate technique will yield a sufficiently accurate value for the force. The simplest approximation combines a set of distant bodies into one object with a total mass equal to the sum of the masses of the individual bodies in the group, positioned at the location of the center of mass of the group:

$$\sum_{j \neq i} -\frac{Gm_j \vec{r}_{ij}}{|\vec{r}_{ij}|^3} \approx -\frac{GM \vec{r}_{i,cm}}{|\vec{r}_{i,cm}|^3}, \quad (\text{A.2})$$

where $\vec{r}_{i,cm} = \vec{r}_i - \vec{r}_{cm}$, \vec{r}_{cm} is the location of the center of mass of the group of bodies, and M is the total mass of the group. In principle this equation could include additional terms on the right-hand side to account for the quadrupole and higher moments of the mass distribution. In practice, equivalent accuracy and higher performance is obtained for moderate levels of accuracy (~ 0.1 percent) by including only the monopole contribution (and, implicitly, the dipole contribution, which is equal to zero) and using an appropriate criterion for determining when the approximation is accurate enough.

Some criterion must be used to determine when the multipole approximation in equation A.2 is sufficiently accurate to use instead of direct summation of the accelerations due to each body in the set. This criterion is called the “multipole acceptability criterion” or MAC. Many different MACs have been proposed, and several are in widespread use. Salmon & Warren (1994) analyzed the worst-case behavior of several different MACs and developed a technique to determine a strict upper limit on the errors in each acceleration calculation. As described in Warren & Salmon (1993, 1995), we use a MAC that incorporates such an error estimate into

the calculation of a critical radius, according to

$$r_c \geq \frac{b_{max}}{2} + \sqrt{\frac{b_{max}^2}{4} + \sqrt{\frac{3B_2}{\Delta_{interaction}}}}, \quad (\text{A.3})$$

where b_{max} is the size of the cell and $B_2 = \sum_i m_i |\vec{r}_i - \vec{r}_{cm}|^2$ is the trace of the quadrupole moment tensor. A body and cell separated by a distance greater than r_c can use equation A.2 to evaluate the acceleration, and the absolute error is guaranteed to be less than $\Delta_{interaction}$; a body and cell closer than r_c must use pairwise summation for each body in the cell, or subdivide the cell into smaller cells and reconsider the interactions, to ensure that the error is not larger than that tolerance.

A.2.2 SPH Hydrodynamics

The particle-based structure of our code allows us to easily implement smoothed particle hydrodynamics (SPH) to model the Euler (inviscid) equations. SPH, invented in 1977 (Lucy, 1977; Gingold & Monaghan, 1977), has become the primary multi-dimensional Lagrangian technique used in astrophysics. Its versatility allows it to be used on a variety of astrophysics problems (see Benz, 1988; Monaghan, 1992, for a review). Many variants of SPH have been developed and a number of excellent reviews on the SPH technique, and its variations, already exist (Benz, 1989; Monaghan, 1992; Morris, 1996; Rasio, 1999; Monaghan, 2005); we provide a brief review here and direct readers interested in more details to the above reviews. Our code was developed using the Benz version of SPH (Benz, 1984, 1988, 1989) as a model and is nearly identical to those codes based on this version of SPH.

A.2.2.1 Brief SPH Primer

SPH is a particle-based method where particles act as interpolation points to determine matter conditions throughout the simulation space. Consider the following

integral representation of the quantity A :

$$A_s(\vec{r}) = \int A(\vec{r}')W(\vec{r} - \vec{r}', h)dr' \quad (\text{A.4})$$

where $W(\vec{r} - \vec{r}', h)$ (the “kernel”) has the following properties:

$$\int W(\vec{r} - \vec{r}', h)dr' = 1 \quad (\text{A.5})$$

and

$$\lim_{h \rightarrow 0} W(\vec{r} - \vec{r}', h) = \delta(\vec{r} - \vec{r}'). \quad (\text{A.6})$$

By integrating A with our kernel, A_s is the “smoothed” version of A (hence the origin of the “smoothed” in SPH). Note that A_s approaches A as $h \rightarrow 0$. If we expand $A(\vec{r}')$ in a Taylor series, we find that:

$$A_s(r) = A(r) + c(\nabla^2 A)h^2 + O(h^3) \quad (\text{A.7})$$

This SPH formalism introduces an error of order h^2 in the estimate of the quantity $A(r)$. Discretizing this method, the integral over A is reduced to a summation over a number of points (particles) in space:

$$A_s(r) = \sum_j A_j(m_j/\rho_j)W(\vec{r} - \vec{r}_j, h) \quad (\text{A.8})$$

where A_j , m_j , and ρ_j are the respective values of A , the mass, and the density of particle j . The structure of the smoothing is determined by the kernel $W(\vec{r} - \vec{r}', h)$ where h denotes the size over which the smoothing occurs (see below).

Although any kernel will work as long as it satisfies equations A.5 and A.6, determining the best kernel for a given problem can be a black art. One of the simplest kernels, and the one we use for most of our calculations (although we also

use other spline kernels) is a cubic spline kernel:

$$W(r, h) = \pi^{-1} h^{-3} \begin{cases} 1 - 1.5v^2 + 0.75v^3 & \text{if } 0 \leq v \leq 1, \\ 0.25(2 - v)^3 & \text{if } 1 \leq v \leq 2, \\ 0. & \text{otherwise,} \end{cases}$$

where $v = r/h$. With this kernel, a given interpolation point (particle) contributes to the value of $A(r)$ only if r is within $2h$ of that particle. The value of h for a given particle i , termed the “smoothing length”, is allowed to vary with time using the relation presented in Benz (1989):

$$dh_i/dt = -1/3(h_i/\rho_i)(d\rho_i/dt) \quad (\text{A.9})$$

This variation is necessary to ensure full spatial coverage by the particles (we would like any position to overlap with a base number of particles) and, as long as h varies on a time scale similar to other variables, the errors remain of order $O(h^2)$ (Hernquist & Katz, 1989). We define the interaction between a particle i and a neighboring particle j by evaluating a mean value $h \equiv (h_i + h_j)/2$. We additionally set limits for the number of neighbors (the standard range for our 3-dimensional models is between ~ 40 and ~ 80 neighbors). In the extreme case that the number of neighbors falls above (or below) these maximum (minimum) values, we additionally lower (raise) h_i by a configurable amount on each timestep (typically a factor of 0.002-0.1) to enforce this range of neighbors (this occurs rarely, if at all, for a given particle during the course of a simulation).

We can now use our interpolation points to calculate the value of any quantity and its derivatives over our spatial domain. The density at position i is simply:

$$\rho_i = \sum_j m_j W(\vec{r}_i - \vec{r}_j, h). \quad (\text{A.10})$$

As with any numerical technique, there is more than one way to discretize our system. This is most apparent in the calculation of derivatives. For example, in principal, the gradient of a function A at particle i is just:

$$\nabla A_i = \sum_b A_j(m_j/\rho_j)\nabla W(\vec{r}_i - \vec{r}_j, h). \quad (\text{A.11})$$

In practice, it is more accurate to use,

$$\nabla A_i = 1/\rho[\nabla(\rho A) - A\nabla\rho] \quad (\text{A.12})$$

$$= 1/\rho_i \sum_j (A_j - A_i)m_j\nabla W(\vec{r}_i - \vec{r}_j, h). \quad (\text{A.13})$$

The review by Morris (1996) includes quite a bit of discussion about these “techniques” used to improve SPH, also noting the situations when one technique might be better than another. We follow the Benz version of SPH for all our discretization assumptions in solving the hydrodynamics equations.

A.2.2.2 Continuity Equation

The Benz version of SPH is a true Lagrangian code - the mass and number of particles is conserved, so the total mass in the system is also conserved.

A.2.2.3 Momentum Equation

We evaluate momentum and energy conservation for the particles themselves and assume an inviscid gas. Hence, the hydrodynamic equations reduce to the Lagrangian form of the Euler equations:

$$d\vec{v}_i/dt = -1/\rho_i(\nabla P)_i \quad (\text{A.14})$$

where $\vec{v}_i = d\vec{r}_i/dt$ and P_i is the pressure of particle i . If we simply use equation A.12, the pressure gradient for particle i is written as

$$(\nabla P)_i = 1/\rho_i \sum_j m_j(P_j - P_i)\nabla_i W_{ij} \quad (\text{A.15})$$

where $W_{ij} = W(\vec{r}_i - \vec{r}_j, h)$. Although such a scheme can be used, it is not symmetric (and hence does not conserve linear and angular momentum). We can instead use

$$\nabla P/\rho = \nabla(P/\rho) + P/\rho^2 \nabla \rho. \quad (\text{A.16})$$

Now using equation A.12 on this representation, we obtain

$$d\vec{v}_i/dt = - \sum_j m_j (P_i/\rho_i^2 + P_j/\rho_j^2) \nabla_i W_{ij}. \quad (\text{A.17})$$

Let's confirm that this algorithm conserves linear momentum. The force on particle i due to particle j is equal to the negative force on particle j due to particle i :

$$m_i d\vec{v}_i/dt = m_i m_j (P_i/\rho_i^2 + P_j/\rho_j^2) \nabla_i W_{ij} = -m_j d\vec{v}_j/dt, \quad (\text{A.18})$$

where we have taken advantage of the fact that the kernels are anti-symmetric $\vec{\nabla}_i W_i(|\vec{r}_i - \vec{r}_j|, h) = -\vec{\nabla}_j W_j(|\vec{r}_i - \vec{r}_j|, h)$. We will show that angular momentum is conserved in section A.4.3.

A.2.2.4 Energy Conservation

Most hydrodynamics codes evolve either the total energy (kinetic + internal) or the internal (thermal) energy alone. In a system with gravity, the total energy also can include the gravitational potential energy. Evolving the total energy ensures a better conservation of the total energy. But in astrophysics, accurate temperatures (and hence energies) are important even in cases where the gravitational potential and kinetic energies dominate the total energy by many orders of magnitude. To obtain reliable internal energies, it is often better to evolve the internal energy alone in the energy equation. The evolution of the specific internal energy u is

$$du/dt = -(P/\rho) \nabla \cdot \vec{v}, \quad (\text{A.19})$$

corresponding to the following SPH formulation,

$$du_i/dt = P_i/\rho_i^2 \sum_j m_j (\vec{v}_i - \vec{v}_j) \cdot \nabla_i W_{ij}. \quad (\text{A.20})$$

See Morris (1996) for other valid SPH formulations of the energy equation.

It is easy to show that this formulation combined with our momentum equation conserves total energy (kinetic and thermal energies). The total energy for all particles is given by

$$d/dt \sum_i m_i u_i = \sum_i \sum_j m_i m_j P_i / \rho_i^2 (\vec{v}_i - \vec{v}_j) \cdot \nabla_i W_{ij}. \quad (\text{A.21})$$

By interchanging indices and again making use of the identity $\nabla_i W_{ij} = -\nabla_j W_{ij}$, we get

$$d/dt \sum_i m_i u_i = \sum_i \sum_j m_i m_j (P_i / \rho_i^2 + P_j / \rho_j^2) (\vec{v}_i - \vec{v}_j) \cdot \nabla_i W_{ij}. \quad (\text{A.22})$$

Comparing this to equation A.17, we find

$$d/dt \sum_i m_i u_i = d/dt (1/2 \sum_i m_i v_i^2) \quad (\text{A.23})$$

which shows that the work done by pressure forces changing the kinetic energy comes at the expense of the internal energy, ensuring the conservation of total energy.

A.2.2.5 Artificial Viscosity

We have limited our description of hydrodynamics to inviscid (Euler) equations. It is well known that any Euler method with finite resolution is unable to describe shocks and will result in large, unphysical oscillations unless one includes some sort of viscosity, low order diffusion or a Riemann solver. Although Godunov-type methods have been developed for SPH (Inutsuka, 1994; Monaghan, 1997; Inutsuka, 2002), most techniques introduce a viscosity term to handle shocks (Benz, 1989; Monaghan, 1992, 2005):

$$\Pi_{ij} = \begin{cases} (-\alpha \bar{c} \mu_{ij} + \beta \mu_{ij}^2) / \bar{\rho}_{ij} & \text{if } (\vec{v}_i - \vec{v}_j) \cdot (\vec{r}_i - \vec{r}_j) \leq 0, \\ 0 & \text{otherwise,} \end{cases}$$

where

$$\mu_{ij} = \frac{h(\vec{v}_i - \vec{v}_j) \cdot (\vec{r}_i - \vec{r}_j)}{|\vec{r}_i - \vec{r}_j|^2 + \epsilon h^2}, \quad (\text{A.24})$$

$\bar{\rho}_{ij} = 1/2(\rho_i + \rho_j)$ and $\bar{c}_{ij} = 1/2(c_i + c_j)$ are the average of the densities and sound speeds of the interacting particles, α and β are the bulk and von Neumann-Richtmyer viscosity coefficients respectively (typically set to 1.5 and 3.0), and ϵ is a factor to avoid divergences at small separations (typically set to 0.01).

The momentum and energy (internal + kinetic) equations can now be rewritten to include this viscosity:

$$d\vec{v}_i/dt = - \sum_j m_j (P_i/\rho_i^2 + P_j/\rho_j^2 + \Pi_{ij}) \nabla_i W_{ij} \quad (\text{A.25})$$

and

$$du_i/dt = P_i/\rho_i^2 \sum_j m_j (\vec{v}_i - \vec{v}_j) \cdot \nabla_i W_{ij} + 1/2 \sum_j m_j \Pi_{ij} (\vec{v}_i - \vec{v}_j) \cdot \nabla_i W_{ij}. \quad (\text{A.26})$$

Clearly, the addition of the artificial viscosity term retains our total (kinetic + internal) energy conservation.

A.2.2.6 Equation of State

To complete these equations, we must include an equation of state to determine pressures from internal energies or entropies. Our basic SPH scheme includes equations of state for isothermal and ideal gases.

A.3 Computational Issues

On a single processor, careful attention to the computational details can significantly accelerate a code's performance. For large-scale parallel architectures, these details are critical to taking full advantage of these supercomputers. Unfortunately, the more complex the code becomes, the more ingenious the computational techniques must be to preserve scalability. Here we discuss just the basic computational issues,

focusing on our tree algorithm (see also Warren & Salmon, 1993, 1995) and the basic parallelization issues arising from use of this tree. We conclude with a discussion of the timestep integrator.

A.3.1 Treecode

The calculation of gravitational forces between bodies in a N-body simulation and the identification of neighbors in a SPH calculation are both accelerated significantly through the use of a treecode, in which a hierarchical “tree” data structure is constructed to represent the spatial arrangement of bodies in a simulation. Our code uses a “parallel hashed oct-tree algorithm” (Warren & Salmon, 1993, 1995), in which each node in the tree can have up to eight “daughter” nodes below it. The “root” of the tree (often imagined to be at the top of the tree in computer science discussions) represents the entire volume of a simulation; each of the root’s eight daughter nodes represents one octant of that overall volume. A complete hierarchical representation of the volume can be created by recursively subdividing each octant and adding more levels of daughter nodes to the tree until some stopping condition is reached. In our implementation of a treecode, we stop subdividing a volume when that volume contains zero particles or only one particle; the node representing that volume in the tree is called a “leaf” node and has no daughters of its own. By performing traversals of the hierarchical tree structure, the treecode can rapidly distinguish between nearby and distant particles and accelerate the calculation of gravitational and pressure forces in simulations.

In descriptions of N-body techniques, the term “body” generally refers to one of the fundamental entities being simulated. In smoothed particle hydrodynamics, the interacting entities are logically called “particles”. In the following discussion, the terms “particle” and “body” are used interchangeably; both refer to a data-carrying entity in a simulation. The term “cell” refers to a cubic region of space containing

(possibly zero) particles; a cell is represented as a node in the tree data structure that stores data used by the treecode, and phrases like “daughter cell” refer to the combined knowledge about a spatial region in the simulation and its topological location within the tree.

Conventional implementations of tree structures represent connections between nodes within the tree as pointers stored in parent nodes that point to the memory locations of the daughters. This technique is difficult to implement on a parallel machine: a parent node on one processor may have daughter nodes located on different processors. Our treecode instead uses multi-bit “keys” to identify particles and cells in the tree; a hash table translates keys into actual memory locations where cell data is stored (hence the word “hashed” in the phrase “parallel hashed oct-tree algorithm”). This level of indirection enables uniform handling of local and non-local cell data; the algorithm that maps hash keys to cell data can request non-local data from other processors and only make it available to the local process once it has arrived.

A.3.1.1 Key Construction

As was mentioned above, each body and cell in the tree is identified by a key; by using the key as an index into a hash table, the code can quickly locate or request delivery of data about any entity in a simulation, and the hash algorithm transparently handles retrieval of data stored on other processors in a parallel machine. The algorithm described below generates keys that, when sorted, arrange the particles into Morton order within the volume of solution; such keys are often called “Morton keys”. Morton ordering results in a list of particles that fairly well reflects spatial locality of bodies in the tree, i.e. particles with Morton keys that fall near each other in the sorted list of keys generally lie near each other in the simulated volume. However, particles sorted into e.g. Peano-Hilbert order can exhibit an even

higher correlation between proximity in the sorted key list and proximity in space, which can lead to more efficient distribution of data on a parallel computer, so modern treecodes have tended to use Peano-Hilbert keys to refer to particles (see, e.g. Springel, 2005). Our treecode supports both Morton and Peano-Hilbert keys, but in practice we have found no noticeable difference in performance; we generally use Morton keys, as described below.

Each Morton key is a set of l_k bits derived from the d floating point coordinates of a body in d -dimensional space. One bit is reserved as a placeholder, for reasons explained below, which leaves $n = (l_k - 1)/d$ bits to represent each of the coordinates of a body. To generate a key for each particle in a simulation, we start by calculating the spatial extent of the simulation and then divide the largest spatial dimension into 2^n equal intervals; the intervals can then be indexed by a n -bit integer. For simplicity, the same interval spacing is used for the other (smaller) spatial dimensions as well. Each floating point coordinate of each body in the simulation is mapped to the n -bit integer index of the spatial interval containing that coordinate.

To construct a key from the d integers derived from the spatial coordinates of a body, the integers are interleaved bit-by-bit. The result is a key composed of n groups of bits, each of length d , where the bits in the i th group are the i th bits of each of the integers identifying the body, arranged in dimension order.

A.3.1.2 Hashing

The mapping from keys and pointers to cell data is maintained via a hash table. The actual hashing function is very simple—we select the h least-significant bits of the key—but because a key reflects the spatial location of the associated cell, the spatial distribution of bodies and cells determines which hash table entries are filled. Each hash table entry is stored in a “hcell”; the hcell contains a pointer to the actual cell data (if the data is local) and maintains knowledge of the state of the

cell data—whether it is local or nonlocal, or if it has been requested from another processor.

A.3.1.3 Tree Construction

The key length l_k determines how many levels of cells the tree can represent, or how close two particles can be, relative to the spatial extent of the simulation, and still be stored separately in the tree. Intermediate (i.e. non-leaf) cells in the tree can be represented in the same key space as individual bodies if the highest bit of every key is set to 1 as a placeholder; the position of this placeholder (the highest non-zero bit) in a cell’s key indicates the depth of that cell in the tree. Given a key for any cell or body, the key of the parent cell can be found by right-shifting the key by d bits (i.e. the number of spatial dimensions). The root of the tree has a key of “1”—the placeholder bit is the lowest (and only) bit in the key.

Keys constructed for bodies are used first to sort the particles and distribute them across the set of processors used in a parallel calculation (see § A.3.2). After each processor receives the bodies assigned to it, a tree of cells is constructed and all local bodies are inserted into the tree. The key associated with a body is not changed when the body is added to the tree; instead, the body is associated with a cell, and the cell key represents the location and depth of the cell in the tree. The first body is inserted into a cell immediately below the root. Subsequent cells are inserted by starting from the location of the previous cell and searching for the appropriate location in the tree; because the bodies are already sorted, the correct location is usually very close to the previously-inserted cell. Often the insertion of a new cell will require a previously-inserted cell to be split, and both the old and new cell will be moved to a lower location in the tree; empty cells are inserted at each tree level between the old and new locations.

An intermediate cell is “finished” when it is clear that no new bodies will be

inserted below it—because the bodies have already been sorted into Morton order, it is easy to determine when no additional bodies will be inserted below a particular cell. The process of “finishing” includes calculating the total mass and spatial extent of the set of all daughter cells, which permits fast evaluation of multipole contributions during calculation of gravitational forces among groups of particles.

A.3.2 Parallelization

Sorting the list of body keys is equivalent to arranging the bodies in Morton order. Morton ordering does a reasonably good job of maintaining locality of data in the sorted list; bodies that are close together in space end up close to each other in the list. This ordering of bodies also allows easy domain decomposition for parallelization; data can be distributed over a set of processors in a parallel machine by cutting the list of bodies into “equal-work” lengths and sending each list section to a different processor. The “work” required to update a particle is usually defined as the number of interactions in which the particle participated during the previous timestep, which generally results in good load-balancing. It is also possible to adjust the estimated work associated with any set of particles to account for, e.g., complex equation of state calculations which take a predictable number of iterations to converge.

Parallel tree construction adds one additional step to the process described in § A.3.1; after building a local tree, each processor finds and transmits a set of “branch cells” to all other nodes. The set of branch cells on a given processor is the coarsest set of cells that contains all of the data stored on that processor. Branch cells are the highest “finished” cells in the local tree; all cells and bodies below a branch cell are also stored on the processor, while cells above the branch cell include regions of space containing particles stored on other processors. Every processor broadcasts its branch cells to every other processor, so that each processor can directly request

non-local cell data from the correct processor during traversals of the tree.

Characterizing the performance of parallel scientific codes is difficult, and trying to doing so for SNSPH presents all the usual pitfalls. Per-processor performance metrics, and scaling of performance with number of processors in a parallel calculation, both vary strongly depending on the size of simulation under consideration, the hardware platform on which the simulation is run, and even the particular physical or numerical conditions present in the simulation. Scaling for SNSPH is linear on hundreds through thousands of processors on modern supercomputers, as long as the problem being simulated is sufficiently large, and the definition of "large" for a given computer depends on the details of the CPU architecture, memory subsystem, node interconnects, and other system components. For a core-collapse simulation including all physics modules within SNSPH, a 4-million-particle set of initial conditions is sufficiently large to support nearly linear scaling on up to 256 processors on Pink at Los Alamos National Laboratory.

A.3.3 Time integration

After the rates of change of all fluid quantities are calculated using the SPH equations, we apply an integration scheme to advance all quantities to the next timestep. To update the specific internal energy u of each particle, we use the 2nd-order Adams-Bashforth method, a 2nd-order method for 1st-order ODEs:

$$u_{i+1} = u_i + \dot{u}_i \left(dt_i + \frac{dt_i^2}{2dt_{i-1}} \right) - \dot{u}_{i-1} \left(\frac{dt_i^2}{2dt_{i-1}} \right). \quad (\text{A.27})$$

The smoothing length h of each SPH particle is updated using the 2nd-order Leapfrog method:

$$h_{i+1} = h_i + \dot{h}_i \frac{dt_i + dt_{i-1}}{2}. \quad (\text{A.28})$$

We update the position x and velocity \dot{x} of each SPH and N-body particle using the Press method, a 2nd-order method for 2nd-order ODEs:

$$\dot{x}_{i+1} = \frac{x_i - x_{i-1}}{dt_{i-1}} + \ddot{x}_i \left(dt_i + \frac{dt_{i-1}}{2} \right), \quad (\text{A.29})$$

$$x_{i+1} = x_i + (x_i - x_{i-1}) \frac{dt_i}{dt_{i-1}} + \ddot{x}_i \frac{dt_i (dt_i + dt_{i-1})}{2}. \quad (\text{A.30})$$

Note that u_{i+1} depends on u_i and u_{i-1} , and x_{i+1} depends on x_i and x_{i-1} (not x_i and \dot{x}_i). Equations A.27, A.29, and A.30 are not self-starting; when a simulation is started (or restarted from an intermediate point), we assume that $u_{i-1} = u_i$ and $x_{i-1} = x_i - \dot{x}_i dt$. At all other times, \dot{x}_i is updated only for the benefit of the user; the Press method updates the position of each particle using the current and previous position.

The term $(x_i - x_{i-1})/dt_{i-1}$ in equation A.29 can suffer from large floating-point roundoff errors if dt_{i-1} is small, the current and previous positions are nearly equal, and the precision of the variables used to store the positions is low; for this reason, the code stores current and previous positions in double-precision variables.

A.4 Code Tests

There are a number of ways to verify and validate a numerical code. These two words have specific meaning in the computational community; verification refers to the process of testing that a code is correctly solving the physical equations it is supposed to be solving, while validation is the process of testing that the physical equations used are the right set of equations required for a given study. Validation is often interpreted as any test that compares results from the code to results from experiments. This is only strictly true if the comparison experiment is (or is nearly identical to) the problem for which one is validating the code. Most tests in astrophysics are verification tests, and we will focus on these here. Astrophysical

verification tests include comparisons to analytic solutions (good for testing specific pieces of physics), convergence studies, and comparisons to other codes. Code comparison is the only true way to test a code’s validity on a complex problem. This mode of code verification will still fail if the codes used for the comparison arrive at the same erroneous result because of different weaknesses in the different codes.

The SNSPH code has already been tested in many of the previous papers that use this code. Fryer & Warren (2002) presented a code-comparison test comparing the 3-dimensional results of the newly developed SNSPH code to the 2-dimensional results from the code described in Herant et al. (1994). The techniques in both these codes are similar, but the codes themselves are very different. Glaring differences due to coding errors would likely have been caught. We are also conducting a detailed comparison of Rayleigh-Taylor and Richtmyer-Meshkov instabilities between SNSPH and the RAGE adaptive mesh refinement code (Fryer et al., 2006c). We have also run precessing disk calculations (Rockefeller et al., 2005c, and chapter 6), comparing the results to both analytical estimates and past SPH calculations (Nelson & Papaloizou, 2000) to test angular momentum transport in the code. Another test of the conservation of angular momentum conducted by Fryer & Warren (2004) is discussed in more detail in § A.4.3.

Here we present three additional tests of our code. We use the same code for all tests and the code was not tuned to produce better results for any specific test. The Sedov-Taylor blast wave problem tests the code’s ability to handle the formation and propagation of shocks; the test has an analytic solution and our code can be tested to high precision. To test the underlying treecode and gravitational force calculations, we run an adiabatic collapse calculation and a binary orbit calculation. The binary orbit calculation can also be used to test angular momentum conservation. In the binary calculation subsection, we also describe techniques in SPH to test the amount

of numerical angular momentum transport.

A.4.1 Sedov-Taylor Blast Wave

The Sedov-Taylor blast wave problem was first discussed by Sedov (1959) and Taylor (1950); Sedov ultimately developed an analytic solution to the problem. An amount of energy $E = 1$ is deposited at time $t = 0$ into a small volume at the center of a uniform-density, low-pressure medium (density $\rho_0 = 1$ and specific internal energy $u = 10^{-5}$ in our test) with a gamma-law equation of state

$$P = (\gamma - 1)\rho u. \quad (\text{A.31})$$

where γ , the ratio of specific heats in the medium, is chosen to be 1.4. The deposited energy heats the gas and drives a spherical shock wave outward through the medium.

The radius of the blast wave R evolves according to the equation

$$R = S(\gamma)t^{2/5}E^{1/5}\rho_0^{-1/5} \quad (\text{A.32})$$

where t is the time elapsed since the explosion and $S(\gamma)$ is a function of the ratio of specific heats. The density, pressure, and radial velocity behind the shock evolve self-similarly according to

$$\rho/\rho_0 = \psi, \quad (\text{A.33})$$

$$P/P_0 = R^{-3}f_1, \quad (\text{A.34})$$

$$v_r = R^{-3/2}\phi_1, \quad (\text{A.35})$$

where ρ_0 and P_0 are the density and pressure of the ambient medium and ψ , f_1 , and ϕ_1 are all functions of $\eta = r/R$. The simplicity of the initial conditions and the existence of an analytic solution make the Sedov-Taylor problem one of the most frequently-used tests of a code's ability to model strong shocks.

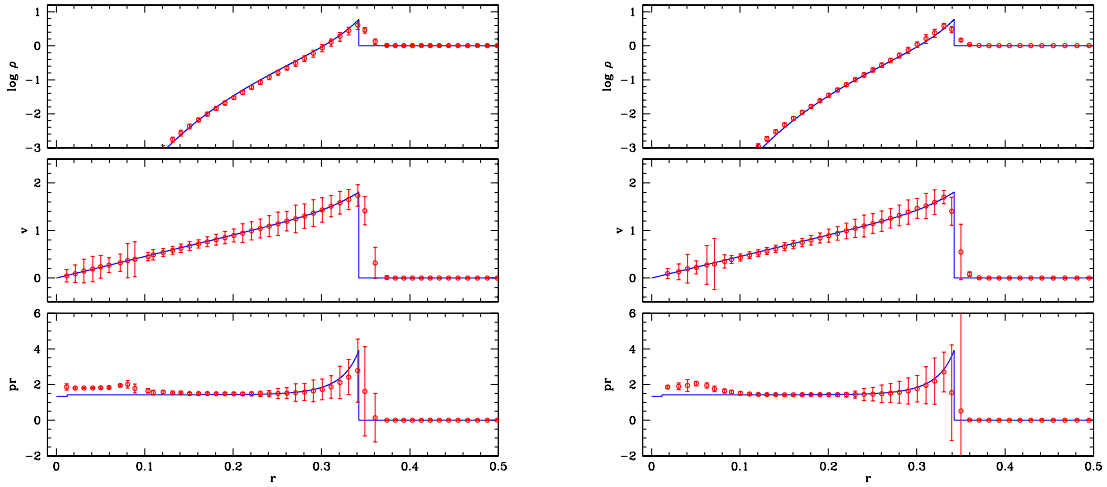


Figure A.1 Sedov blast wave profile. Angle-averaged density, velocity, and pressure profiles at time $t = 0.063$ from two SPH simulations of a Sedov blast wave; the blue lines indicate the analytic solution. The two simulations use slightly different initial conditions, and consequently the results differ slightly as well; for example, the calculated density behind the shock generally falls below the analytic value in the first simulation but above the analytic value in the second. See § A.4.1 in the text for further discussion.

Figure A.1 shows the angle-averaged density, velocity, and pressure profiles taken at time $t = 0.063$ from two Sedov explosions simulated using SPH. The two simulations differ only in the specific arrangement of particles used for the initial conditions; both sets of initial conditions were constructed from concentric spherical shells of particles, but the simulation shown in the right-hand plot had an inner shell radius ten times smaller than the inner shell radius used in the left-hand simulation. Each circle represents the mass-weighted mean flow quantity and location of particles in a single radial bin (where the width of each bin is 0.01). The error bars indicate one (mass-weighted) standard deviation around the weighted mean. The blue line indicates the analytic solution.

Part of the scatter in the particle densities and pressures at a given radius arises

from uncertainties in the initial density profile. One drawback of SPH is that there is an intrinsic scatter in the density because of the dependence on and variability of individual smoothing lengths and particle-particle separations. Even if we fine-tune the initial model, the scatter will develop after a few timesteps. This scatter places a low-level perturbation to seed any convection. In most past simulations using SNSPH, this scatter introduced a 1-sigma error of 10% in the density. Although we now can reduce this scatter somewhat, it is still an issue with SNSPH calculations. In stellar collapse, it is likely that the explosive burning just prior to collapse produces density perturbations at this level. If anything, the 10% scatter in our SPH set-up is on par with what we expect to be the true initial conditions. We have run calculations with a factor of 2 larger scatter, and it did not alter our convection or mixing results in the explosion calculation.

The two simulations also illustrate the effect of different initial particle arrangements on flow quantities throughout the simulation. Decreasing the radius of the innermost shell of particles results in a pressure profile that more accurately matches the analytic solution behind the shock front. Additionally, the density profile in the left-hand simulation falls slightly below the analytic value, while the density in the right-hand simulation is slightly higher than the analytic value. This variation demonstrates the sensitivity of SPH to the initial arrangements of particles in a simulation and emphasizes the importance of carefully constructing and testing sets of initial conditions.

From these calculations, we see that the SPH calculation produces fairly accurate shock velocities, but densities and pressures that are low (although the shock entropy is more accurate). These errors decrease with resolution but, in most of our core-collapse simulations, we have not yet reached a satisfactory convergence on the shock modeling. A more realistic, but less standard, test would have a shock traverse a

density gradient instead of a constant density profile. Fryer et al. (2006c) compares the results of such a test for a number of coding techniques, including this SNSPH code.

A.4.2 Adiabatic Collapse

The adiabatic collapse of an initially isothermal spherical cloud of gas has been used in several investigations of SPH codes with gravity (Steinmetz & Müller, 1993; Thacker et al., 2000; Springel et al., 2001; Wadsley et al., 2004). We follow the units used in the first presentation of this problem (Evrard, 1988). With $G = M = R = 1$, the initial density distribution is

$$\rho(r) = M/(2\pi R^2)r^{-1} = (2\pi r)^{-1}, \quad (\text{A.36})$$

where M is the total mass of the system within the cut-off radius R .

The initial internal energy of the system is chosen as $0.05GM/R$, with the adiabatic index $\gamma = 5/3$. The initial physical density distribution was applied to a grid with hexagonal symmetry using the technique of Davies et al. (1992). The gravitational potential was smoothed with a Plummer softening of $0.01 R$ (Plummer, 1911). The SPH kernel was initially set to give roughly 60 neighbors for each particle, and the SPH smoothing length was allowed to evolve within the constraints of $h_{max} = 150$ and $h_{min} = 30$.

We show results for simulations with 47,000 particles, and with 864,000 particles in Figure A.2. The 864k simulation conserves total (kinetic + internal + potential) energy to the 1% level at $t=2.1$ using 1475 timesteps. The 47k simulation conserves total energy to 1.2% at $t=3.0$ using 600 timesteps. Our version of SPH gives very similar results to the version of SPH presented in Steinmetz & Müller (1993). As we increase resolution, our solution approaches the solution from their 1-dimensional PPM simulation which has a much higher effective resolution per dimension.

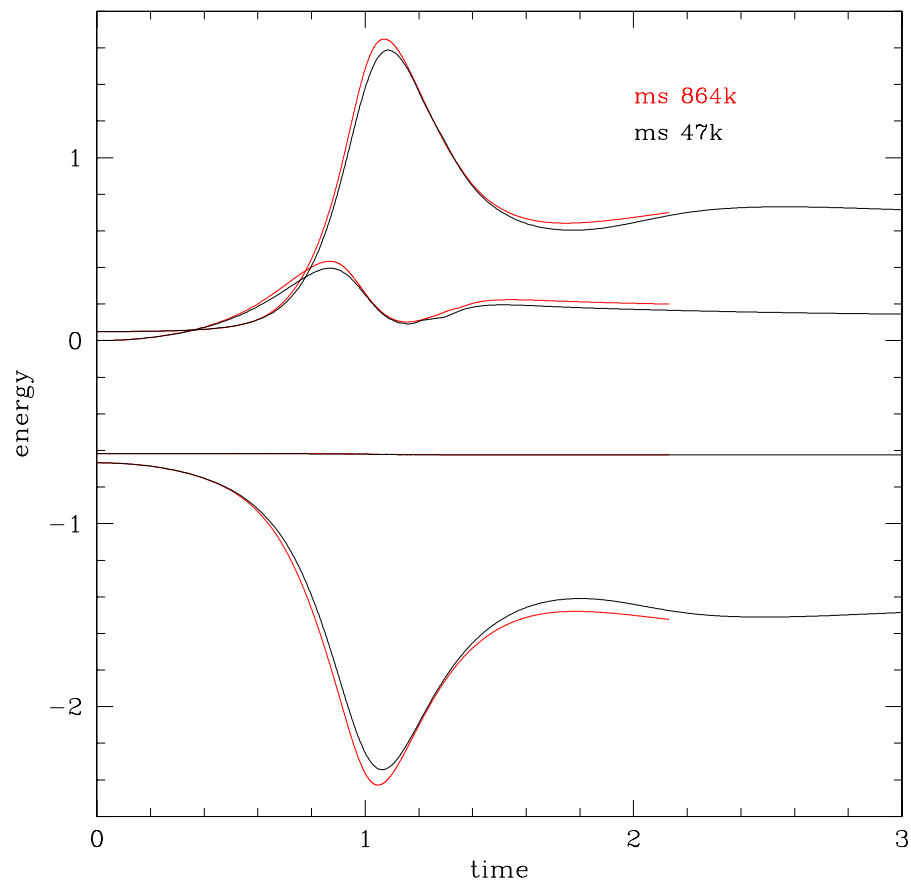


Figure A.2 Energy evolution during adiabatic collapse. The time evolution of thermal, kinetic, total and gravitational potential energies during the adiabatic collapse of an initially isothermal gas sphere for SPH calculations with 43,000 and 864,000 particles. This figure may be compared with the 1-dimensional PPM and 3-dimensional SPH calculations from Figure 6 of Steinmetz & Müller (1993).

A.4.3 Binary Orbits: Testing Angular Momentum Conservation

One of the true strengths of the SPH method is that it can conserve both linear and angular momentum at the same time. This feature makes SPH an ideal technique in modeling binary interactions and rotation in core-collapse calculations. However, even though SPH conserves angular momentum between particle interactions and hence is globally conserved, a code may still numerically transport that angular momentum and one must test both the conservation and artificial transport before running simulations that depend heavily on angular momentum. In this subsection, we will focus on a test to determine the level at which angular momentum is conserved in our SPH code. We first show how the SPH equations lead to angular and linear momentum conservation. To test the actual application of these equations, we follow the evolution of a close binary system for over 15 orbits. This test allows an ideal measurement of the angular momentum conservation in a system. We end with a discussion of methods to test the importance of numerical angular momentum transport.

Angular momentum is conserved by noting that the forces are always directed along a line joining the particle pairs (eq. A.18). Recall that the torque on a given particle i by particle j is $\tau_{i,j} = \vec{r}_i \times \vec{F}_i$ where \vec{r}_i is the vector from a reference point to particle i and \vec{F}_i is the force on particle i due to particle j . Figure A.3 shows our particle pair. Because the acceleration of our particles is along the line joining these particles, the torque on any two particles are equal in magnitude, but opposite in sign:

$$\tau_i = r/\sin(\theta_i)F_i\sin(\theta_i) = rF_i = r/\sin(\theta_j)F_j\sin(\theta_j) = -rF_i = -\tau_i, \quad (\text{A.37})$$

where we have used the relation $F_i = m_i(d\vec{v}_i/dt)_j = -m_j(d\vec{v}_j/dt)_i = -F_j$ from equation A.18. The SPH equations strictly conserve linear and angular momentum.

To test how well such a formalism works in an applied problem, we consider the

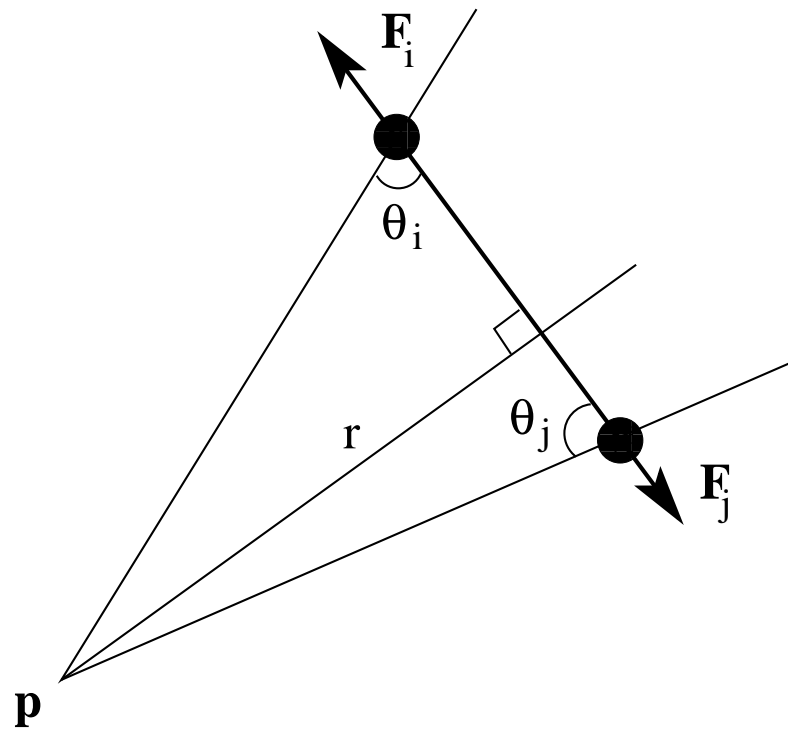


Figure A.3 Diagram of forces between SPH particles. Diagram of the force interactions between a pair of particles in an SPH calculation. The torque on particle i from particle j viewed from an arbitrary reference point p is $(r/\sin\theta_i)F_i\sin\theta_i$. Using $F_i = -F_j$ from § A.4.3, one can easily show that the torque on particle i from particle j is equal, but opposite, to the torque exerted on particle j by particle i .

problem of a binary system in an extremely close orbit. We use two equal-massed stars with a semi-major axis of $2 \times R_{\text{star}}$. The initial stars were evolved for the equivalent of 6 orbits as single stars before being placed into this binary system. These two single stars were then placed in a close orbit around each other with spin periods set to the orbital period. This close orbit was chosen to study the angular momentum conservation in an extreme situation, but bear in mind that the stellar radius is roughly 20% larger than its Roche-radius, so as time proceeds, the stars will gradually lose matter. But since we run our simulations only for 18 orbits, we shall see that this is only a large effect at late times. Such a binary test simulation, but under less extreme orbital conditions, has been done with grid-based codes (e.g. Motl et al., 2002) and we compare, where possible, with these simulations.

Fig. A.4 shows a slice ($|z| < 50$ code units) in particle distribution for our binary system at 6 different times (roughly corresponding to the same point in the orbit except for the last time which corresponds to our final time dump). No particles leave the system (all particles remain bound to their star). However, because they are both overfilling their Roche-radius, the stars slowly expand with time, preferentially building up mass at the L1 Lagrange point. Fig. A.5 shows the angular momentum as a function of time (bottom) and the orbital radius as a function of time (top) for the binary. The orbital radius oscillates because of a slight error in our choice of the orbital velocity in the initial condition. As we shall see, this ultimately causes the code to break. As we are using our tests to find weaknesses in the code, we believe this initial deviation from a circular orbit a nice additional test to the code. In addition, the orbital separation drops by nearly 1% after 18 orbits. This is mostly because material is piling up at the L1 point, causing the mass-weighted center of the stars to move slightly toward that Lagrange point. The orbital angular momentum remains nearly constant, deviating by only 0.01% after 15 orbits. This occurred with

fairly lenient error tolerances on our MAC and no tuning of the code to address this problem. The lack of angular momentum conservation is a result of the distortion in the stars coupled to the lenient tolerances on the MAC (leading to growing errors in the gravitational acceleration). A circular orbit initial condition, or more stringent MAC tolerances could reduce this error. In comparison, the tuned simulations (the best we have seen thus far by grid codes) by Motl et al. (2002) using grid methods found deviations of nearly 0.08% after only 5 orbits!

Not all of the expansion of the star is due to Roche-Lobe overflow. The tidal forces in this problem lead to friction that, with our artificial viscosity, causes the star to heat up and expand. This numerical artifact of codes with artificial viscosity leads to poor energy conservation. Many fixes exist (Balsara, 1995; Owen, 2004), but in most of the problems we have studied, shocks develop quickly and are fairly extensive. For such problems with widespread shocks, these fixes do not seem to make a noticeable difference in the simulation and we do not include these techniques in any of the current simulations done with this code. Figure A.6 shows the absolute value of the energy components as a function of time in units of the total energy. Because the stars are bound, the potential (dotted line) and total (solid) energies are negative. The magnitude of the total, potential, and thermal energy all decrease with time because of the expansion of the stars. The kinetic energy, the primary diagnostic of the orbits, remains relatively constant (which is a simple reflection of the conserved angular momentum and the rough conservation in the orbital radius). Because of the high artificial viscosity in this simulation, the system gains 10% of its total energy after 10 orbits, and another 15% after 18 orbits. The artificial viscosity terms were reduced slightly from our standard set: $\alpha = 1.0, \beta = 2.0$, but varying this value did not change our momentum conservation noticeably. At the expense of accuracy in shock modeling, we could decrease the artificial viscosity to reduce

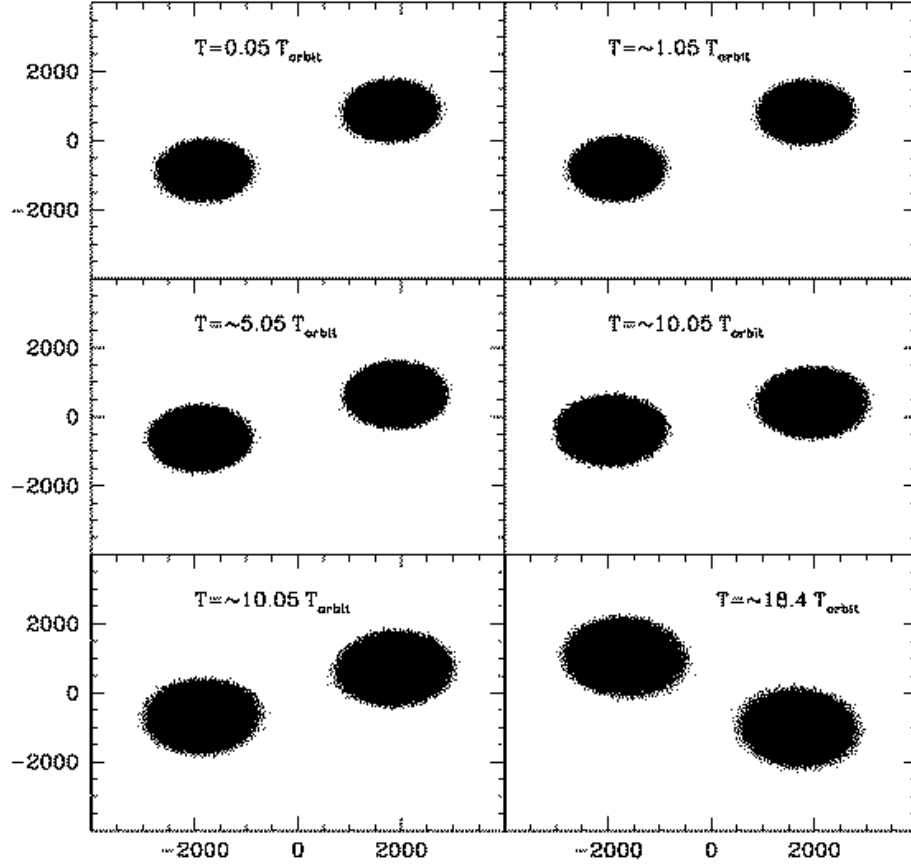


Figure A.4 Snapshots of a self-gravitating binary system. Snapshots in time of the evolution of a binary system put just inside the Roche-radius separation. The particles shown are limited to a slice in the orbital plane, $-50 < z < 50$ in code units. Although most aspects of this problem are scalable, the actual problem is of two $16 M_{\odot}$ stars with a separation of 4×10^{11} cm placed in a nearly circular orbit.

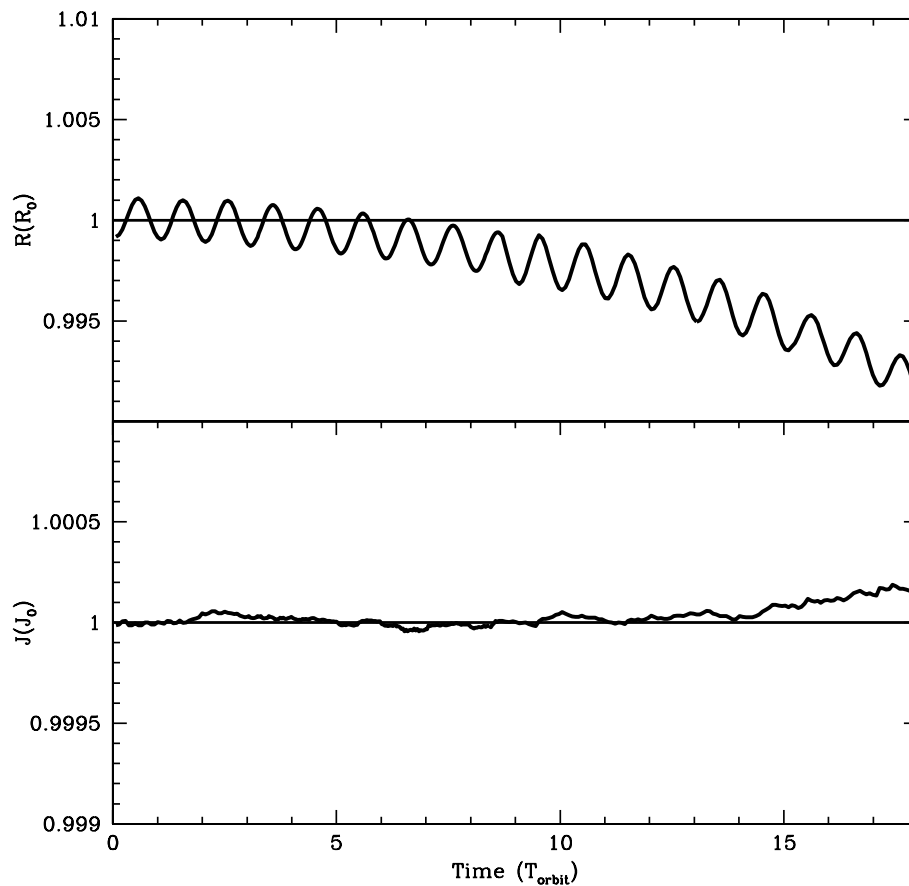


Figure A.5 Orbital separation and angular momentum of binary system. Top: Mass-averaged orbital separation (in units of the initial separation) versus time (in units of orbital periods) for the binary simulation. The oscillations arise from errors in the initial orbital velocities. As mass begins to fill the Lagrange point, the mass-averaged orbital separation begins to decrease. Bottom: total angular momentum (in units of initial total angular momentum) versus orbital time. The total angular momentum is conserved to better than 0.01% for 15 orbits.

the errors in the energy conservation.

The artificial viscosity in SPH, acting like any viscosity (real or numerical), leads also to angular momentum transport. Fryer & Warren (2004) worried about this specific effect in their collapse calculations of rotating supernovae. Fortunately, numerical viscosity can be controlled and its effects can be understood. Figure A.7 shows the angular momentum profile versus mass (top) for a standard model (1 million particles - solid line), a model with high resolution (5 million particles - dashed line) and a model with the artificial viscosity reduced by a factor of 10 (dotted line). The high resolution and reduced viscosity simulations reduce the effect of numerical angular momentum transport (in the reduced viscosity simulation, by nearly a factor of 10). The bottom panel of figure A.7 shows the ratio of angular velocities of the two modified simulations with respect to the standard simulation. What we find is roughly 20% more angular momentum in the core. With our extreme reduction in viscosity, this corresponds to the maximum errors in the angular momentum transport caused by numerical viscosity. This result eased the concerns of Fryer & Warren (2004) regarding the effects of numerical viscosity on the angular momentum transport in their collapse calculations.

Both the conservation and numerical transport of angular momentum must be studied when modeling rotating systems. In most cases, SNSPH exhibits very few numerical errors with angular momentum and is an ideal technique for rotating problems.

A.5 Conclusions

The SNSPH code is built upon the parallel tree code of Warren & Salmon (1993, 1995). This code has proven extremely portable and scalable (beyond 1000 processors) on a number of computer architectures from large supercomputers, such as the

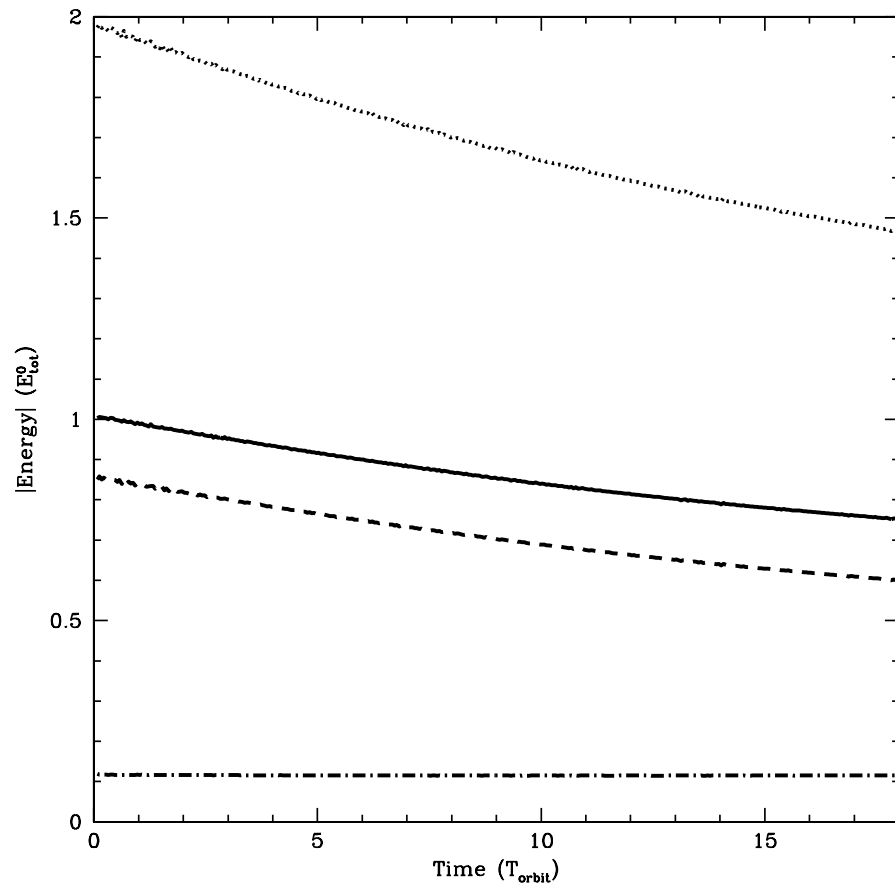


Figure A.6 Energy evolution of binary system. Absolute energy versus orbital time. The total (kinetic plus thermal plus potential) energy (solid line) and potential energy (dotted line) are both negative (the system is bound). Artificial viscosity causes the star to heat up, but because it then expands, the total thermal energy (dashed line) actually decreases with time. The kinetic energy (dot-dashed line), however, remains relatively constant, a reflection of the angular momentum conservation.

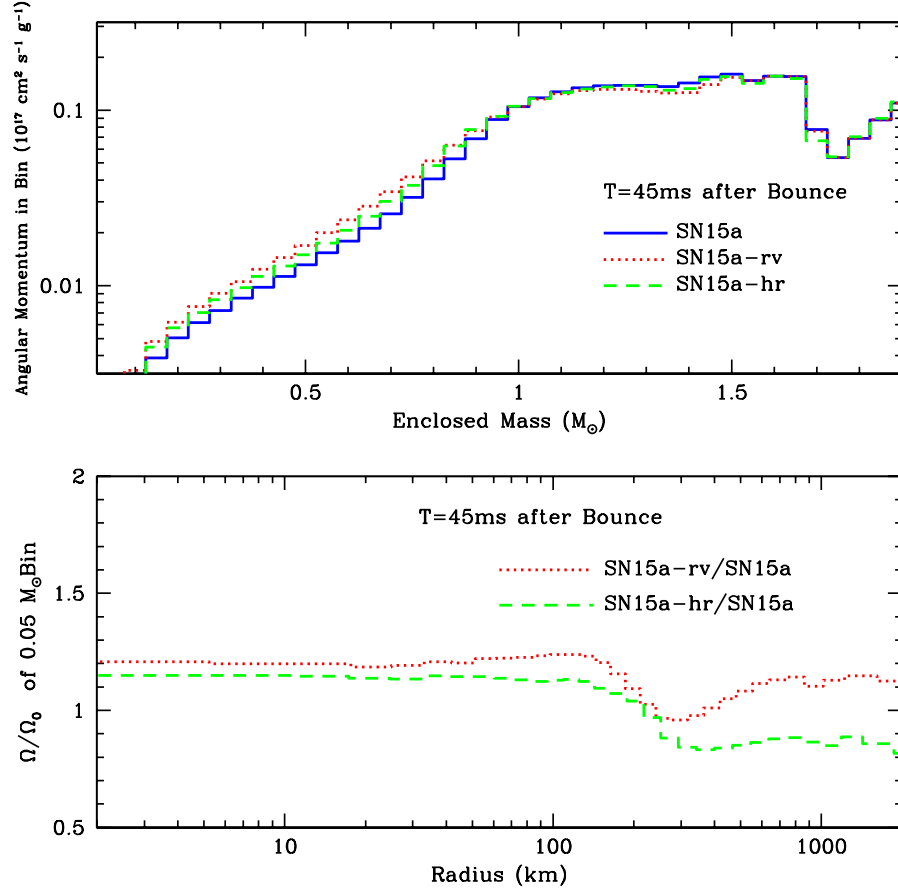


Figure A.7 Angular momentum and angular velocity profiles. Top: Angular momentum versus enclosed mass for a rotating collapsing star (Fryer & Warren, 2004). The 3 lines represent the standard model (solid line), a model using an artificial viscosity reduced by a factor of 10 (dotted line), and a high resolution model (dashed line). Bottom: The ratio of these angular velocities: reduced viscosity/standard (dotted line) and high resolution/standard (dashed). The answer does not change by more than 10-20% when reducing the artificial viscosity, and it is unlikely that we are off by more than that value for the angular momentum in our simulations.

Advanced Simulation and Computing Program (e.g. Red, Pink, Q) and National Energy Research Scientific Computing Center systems (e.g. Seaborg), to local Beowulf clusters, such as the Space Simulator at Los Alamos National Laboratory. SNSPH uses the Benz version (Benz, 1989) of smoothed particle hydrodynamics to model the Euler equations. A number of equations of state have been implemented to close these equations, from ideal and perfect gas equations of state to planetary equations of state (Benz et al., 1986) to the equation of state cocktail used to model core-collapse (Herant et al., 1994). SNSPH also includes an explicit flux-limited diffusion scheme to moderate neutrino transport (Herant et al., 1994; Fryer & Warren, 2002). This transport scheme is even now being modified to model photon transport.

Although the focus of SNSPH has been to study stellar collapse (Fryer & Warren, 2002, 2004; Fryer, 2004) it has also been adapted to model stellar explosions (Hungerford et al., 2003, 2005a) and the Galactic center (Rockefeller et al., 2004, 2005a) with a list of ongoing projects that spreads even further to planet formation and cosmology.

But, as with any computational technique, this code has both advantages and disadvantages. We have presented a number of tests of this SNSPH code. Our tests mark just the beginning set of tests SNSPH must pass if it is to become a multi-purpose radiation hydrodynamics code.

Even so, we can already outline the strengths and weaknesses of the SNSPH technique. The particle based scheme allows modelers to preserve many advantages of a Lagrangian scheme in turbulent flows where typical grid-based Lagrangian cells become tangled. We have shown that the hydrodynamics scheme conserves both total energy and momentum. Our scheme is easily modified to include a wide variety of equations of state and external forces and the transport scheme can be

modified to model the transport of photons as well as neutrinos. The advantages include:

- 1: Lagrangian technique allows the resolution to follow the mass. This is ideal for problems that cover a large range of spatial scales, but that focus the mass in one place (e.g. supernova explosions). It is also ideal for problems where the area of interest moves with time (e.g. in neutron star kicks and in binaries).
- 2: The Lagrangian scheme also avoids any numerical diffusion (either heat or elemental abundances) that plague any Euler scheme during the advection step. Such artificial diffusion can lead to disastrous results in problems where the abundances must be tracked exactly (e.g. nucleosynthesis issues in supernova explosions) and abundance gradients are large. The same is true for problems where the temperature gradient is large.
- 3: SPH conserves angular momentum and linear momentum at the same time.
- 4: The explicit flux-limited diffusion transport scheme scales well (for transport schemes).

The disadvantages of the particle based method are relatively few:

- 1: SPH initial conditions tend to have small perturbations on the 5-10% level that will artificially seed convection. Such perturbations are difficult to reduce completely and their effects must be understood when interpreting simulation results.
- 2: The artificial viscosity term added to model shocks does not work as well as Riemann methods when the shock moves parallel to the grid. However, when the shock is not so well-behaved, SPH behaves as well as most grid codes. The artificial viscosity also leads to both an artificial angular momentum and

artificial heating term. In shear flows, such numerical effects can lead to unrealistic heating. We have shown (Fryer & Warren, 2004) that this is not an issue for even our fast-rotating supernova cores.

- 3: Transport schemes are generally designed for grid-based codes. The flux-limited transport scheme in this code works at a basic level, but more sophisticated schemes have not been incorporated into SPH, and much more work must be done to prove that more sophisticated schemes can be added smoothly.

No code is ideal for all problems. Without the development of a more sophisticated transport scheme for SPH (whether it be a direct discretization method such as S_n or a Monte-Carlo technique), our SNSPH code will not be able to model the types of radiation-hydrodynamic problems now being investigated with cutting-edge grid codes and transport schemes. New transport schemes applicable for SPH are being pursued and the current dearth of schemes may not prove a long-term limitation. There are many problems that are most easily solved with a Lagrangian technique, from supernova explosions to binary mergers to galaxy collisions. SNSPH is ideally suited for these problems and has the versatility to adapt to these problems quickly. With other problems, such as black hole accretion disks, the gas accretion during the formation of Jovian planets or the complex shock structure in the Galactic center, SNSPH has its advantages and disadvantages over grid-based codes. SNSPH is a powerful tool in developing a solution to these outstanding astrophysical problems.

REFERENCES

- Allen, D., Hyland, A., & Hillier, D. 1990, MNRAS, 244, 706
- Baganoff, F. K., Maeda, Y., Morris, M., Bautz, M. W., Brandt, W. N., Cui, W., Doty, J. P., Feigelson, E. D., Garmire, G. P., Pravdo, S. H., Ricker, G. R., & Townsley, L. K. 2003, ApJ, 591, 891
- Balbus, S. A. & Hawley, J. F. 1991, ApJ, 376, 214
- Balbus, S. A. & Hawley, J. F. 1992, ApJ, 400, 610
- Balick, B. & Brown R. L. 1974, ApJ, 194, 265
- Balsara, D. S. 1995, J. Comput. Phys., 121, 357
- Bardeen, J. M. & Petterson, J. A. 1975, ApJL, 195, L65
- Benz, W., Thielemann, F.-K., & Hills, J. G. 1989, ApJ, 342, 986
- Benz, W. 1984, \dot{a} , 139, 378
- Benz, W. 1988, Comp. Phys. Comm., 48, 97
- Benz, W. 1989, in “Numerical Modeling of Stellar Pulsation: Problems and Prospects”, NATO Workshop, Les Arcs, France (1989), 269
- Benz, W., Slattery, W. L., & Cameron, A. G. W. 1986, Icarus, 66, 515
- Blandford, R. D. 1996, in Gravitational Dynamics, Terlevich, R., Terlevich, E., eds., Cambridge University Press, 125
- Blinnikov, S. I., Dunina-Barkovskaya, N. V., & Nadyozhin, D. K. 1996, ApJS, 106, 171
- Blondin, J. M., Mezzacappa, A., & DeMarino, C. 2003, ApJ, 584, 971
- Bower, G. C., Wright, M. C. H., Falcke, H., & Backer, D. C. 2003, ApJ, 588, 331
- Bower, G. C., Falcke, H., Herrnstein, R. M., Zhao, J.-H., Goss, W. M., & Backer, D. C. 2004, Science, 304, 704
- Bromley, B., Melia, F., & Liu, S. 2001, ApJL, 555, L83
- Brotherton, M. S., Green, R. F., Kriss, G. A., Alexander, T., Kim, J., Zheng, W., Kaiser, M. E., Oegerle, W., & Hutchings, J. 2001, BAAS, 33, 1514

- Burrows, A., Livne, E., Dessart, L., Ott, C., & Murphy, J. 2006, *ApJ*, 640, 878
- Bykov, A. M., Chevalier, R. A., Ellison, D. C., & Uvarov, Yu. A. 2000, *ApJ*, 538, 203
- Cantó, J., Raga, A. C., & Rodríguez, L. F. 2000, *ApJ*, 536, 896
- Chevalier, R. A. 1974, *ApJ*, 188, 501
- Chevalier, R. 1992, *ApJL*, 397, L39
- Christopher, M. H., Scoville, N. Z., Stolovy, S. R., & Yun, M. S. 2005, *ApJ*, 622, 346
- Coker, R. & Melia, F. 1997, *ApJL*, 488, L149
- Coker, R. et al., in preparation
- Cotera, A. S., Erickson, E. F., Colgan, S. W. J., Simpson, J. P., Allen, D. A., & Burton, M. G. 1996, *ApJ*, 461, 750
- Cox, D. P. 1972, *ApJ*, 178, 159
- Davies, M. B., Benz, W., & Hills, J. G. 1992, *ApJ*, 401, 246
- DePoy, D. L., Gatley, I., & McLean, I. S. 1989, *IAU Symp.*, 136, 361
- Eckart, A. & Genzel, R. 1996, *Nature*, 383, 415
- Evrard, A. E. 1988, *MNRAS*, 235, 911
- Fabian, A. 1977, *Nature*, 269, 672
- Figer, D. F., Najarro, F., Morris, M., McLean, I. S., Geballe, T. R., Ghez, A. M., & Langer, N. 1998, *ApJ*, 506, 384
- Figer, D. F., McLean, I. S., & Morris, M. 1999a, *ApJ*, 514, 202
- Figer, D. F., Kim, S. S., Morris, M., Serabyn, E., Rich, R. M., & McLean, I. S. 1999b, *ApJ*, 525, 750
- Figer, D. F., Najarro, F., Gilmore, D., Morris, M., Kim, S. S., Serabyn, E., McLean, I. S., Gilbert, A. M., Graham, J. R., Larkin, J. E., Levenson, N. A. & Teplitz, H. I. 2002, *ApJ*, 581, 258
- Fragile, P. C. & Anninos, P. 2005, *ApJ*, 623, 347
- Fromerth, M. J., Melia, F., & Leahy, D. A. 2001, *ApJL*, 547, L129

- Fryer, C. L. & Heger, A. 2005, *ApJ*, 623, 302
- Fryer, C. L. & Kusenko, A. 2006, *ApJS*, 163, 335
- Fryer, C. L. & Warren, M. S. 2002, *ApJL*, 574, L65
- Fryer, C. L. & Warren, M. S. 2004, *ApJ*, 601, 391
- Fryer, C. L., Benz, W., Herant, M., & Colgate, S. A. 1999, *ApJ*, 516, 892
- Fryer, C. L., Rockefeller, G., Hungerford, A., & Melia, F. 2005, *ApJ*, 638, 786
- Fryer, C. L., Rockefeller, G., & Warren, M. S. 2006a, *ApJ*, 643, 292
- Fryer, C. L., Rockefeller, G., & Young, P. A. 2006b, *ApJ*, 647, 1269
- Fryer, C. L. et al. 2006, in preparation
- Fryer, C. L. 2004, *ApJ*, 601, L175
- Güsten, R., Genzel, R., Wright, M. C. H., Jaffe, D. T., Stutzki, J., and Harris, A. I. 1987, *ApJ*, 318, 124
- Gatley, I., Jones, T., Hyland, A., Wade, R., Geballe, T., & Krisciunas, K. 1986, *MNRAS*, 222, 299
- Geballe, T. R., Wade, R., Krisciunas, K., Gatley, I., & Bird, M. C. 1987, *ApJ*, 320, 562
- Geballe, T., Krisciunas, K., Bailey, J., & Wade, R. 1991, *ApJL*, 370, L73
- Genzel, R., Thatte, N., Krabbe, A., Kroker, H., & Tacconi-Garman, L. E. 1996, *ApJ*, 472, 153
- Genzel, R., Eckart, A., Ott, T. & Eisenhauer, F. 1997, *MNRAS*, 291, 219
- Gerhard, O. 2001, *ApJ*, 546, L39
- Ghez, A. M., Salim, S., Hornstein, S. D., Tanner, A., Lu, J. R., Morris, M., Becklin, E. E., & Duchêne, G. 2005, *ApJ*, 620, 744
- Gingold, R. A., & Monaghan, J. J. 1977, *MNRAS*, 181, 375
- Hall, D., Kleinmann, S., & Scoville, N. 1982, *ApJL*, 260, L53
- Haller, J. W., Rieke, M. J., Rieke, G. H., Tamblyn, P., Close, L., & Melia, F. 1996, *ApJ*, 456, 194

- Herant, M., Benz, W., Hix, W. R., Fryer, C. L., & Colgate, S. A. 1994, *ApJ*, 435, 339
- Hernquist, L. & Katz, N. 1989, *ApJS*, 70, 419
- Herrnstein, R. & Ho, P. T. P. 2005, *ApJ*, 620, 287
- Hix, W. R., & Thielemann, F. K. 1996, *ApJ*, 460, 869
- Hungerford, A. L., Fryer, C. L., & Warren, M. S. 2003, *ApJ*, 594, 390
- Hungerford, A. L., Fryer, C. L., & Rockefeller, G. 2005a, *ApJ*, 635, 487
- Hungerford, A. L., Fryer, C. L., Timmes, F. X. & McGhee, K. 2005, *Nucl. Phys. A*, 758, 15
- Igumenshchev, I. V. & Narayan, R. 2002, *ApJ*, 566, 137
- Inutsuka, S. 1994, *Memorie della Societa Astronomia Italiana*, 65, 1027
- Inutsuka, S. 2002, *J. Comput. Phys.*, 179, 238
- Jackson, J. M., Geis, N., Genzel, R., Harris, A. I., Madden, S., Poglitsch, A., Stacey, G. J., & Townes, C. H. 1993, *ApJ*, 402, 173
- Koyama, K., Maeda, Y., Sonobe, T., Takeshima, T., Tanaka, Y., & Yamauchi, S. 1996, *PASJ*, 48, 249
- Krabbe, A., Genzel, R., Drapatz, S., & Rotaciuc, V. 1991, *ApJL*, 382, L19
- Krolik, J. & Hawley, J. 2002, *ApJ*, 573, 754
- Krolik, J. 1999, *ApJL*, 515, L73
- Lacy, J. H., Achtermann, J. M., & Serabyn, E. 1991, *ApJL*, 380, L71
- Lang, C. C., Figer, D. F., Goss, W. M., & Morris, M. 1999, *AJ*, 118, 2327
- Lang, C. C., Goss, W. M., & Rodríguez, L. F. 2001, *ApJL*, 551, L143
- Lang, C. C. 2002, in *A Massive Star Odyssey, from Main Sequence to Supernova*, IAU Symp. 212, Eds. K. A. van der Hucht, A. Herrero, & C. Esteban
- Lattimer, J. M., & Swesty, F. D. 1991, *Nucl. Phys. A*, 535, 331
- Law, C. & Yusef-Zadeh, F. 2004, *ApJ*, 611, 858
- Leising, M. 2002, *NewA Rev.*, 46, 529

- Lis, D. C. & Carlstrom, J. E. 1994, ApJ, 424, 189
- Liu, S. & Melia, F. 2001, ApJL, 561, L77
- Liu, S. & Melia, F. 2002a, ApJL, 566, L77
- Liu, S. & Melia, F. 2002b, ApJL, 573, L23
- Lo, K. Y., & Claussen, M. J. 1983, Nature, 306, 647
- Lucy, L. 1977, AJ, 83, 1013
- Maeda, Y., Baganoff, F. K., Feigelson, E. D., Morris, M., Bautz, M. W., Brandt, W. N., Burrows, D. N., Doty, J. P., Garmire, G. P., Pravdo, S. H., Ricker, G. R., & Townsley, L. K. 2002, ApJ, 570, 671
- Maillard, J. P., Paumard, T., Stolovy, S. R., & Rigaut, F. 2004, *a*, 423, 155
- Marr, J. M., Wright, M. C. H., & Backer, D. C. 1993, ApJ, 411, 667
- McGinn, M. J., Sellgren, K., Becklin, E. E. & Hall, D. N. B. 1989, ApJ, 338, 824
- McMillan, S. L. W. & Portegies Zwart, S. F. 2003, ApJ, 596, 314
- Melia, F. & Coker, R. 1999, ApJ, 511, 750
- Melia, F. & Falcke, H. 2001, ARA&A, 39, 309
- Melia, F. 1994, ApJ, 426, 577
- Melia, F., Liu, S., & Coker, R. 2000, ApJL, 545, L117
- Melia, F., Liu, S., & Coker, R. 2001, ApJ, 553, 146
- Mezger, P. G., Zylka, R., Salter, C. J., Wink, J. E., Chini, R., Kreysa, E., & Tuffs, R. 1989, *a*, 209, 337
- Monaghan, J. J. 1992, ARA&A, 30, 543
- Monaghan, J. J. 1997, J. Comput. Phys., 136, 298
- Monaghan, J. J. 2005, Reports on Progress in Physics, 68, 1703
- Morris, M. 1993, ApJ, 408, 496
- Morris, J. P. 1996, PhD thesis, Monash University, Melbourne
- Motl, P. M., Tohline, J. E., & Frank, J. 2002, ApJS, 138, 121

- Murakami, H., Koyama, K., Sakano, M., Tsujimoto, M., & Maeda, Y. 2000, *ApJ*, 534, 283
- Nagata, T., Woodward, C. E., Shure, M., & Kobayashi, N. 1995, *AJ*, 109, 1676
- Najarro, F., Krabbe, A., Genzel, R., Lutz, D., Kudritzki, R., & Hillier, D. 1997, *A&A*, 325, 700
- Nelson, R. P. & Papaloizou, J. C. B. 2000, *MNRAS*, 315, 570
- Owen, J. M. 2004, *J. Comput. Phys.*, 201, 601
- Ozernoy, L. M., Genzel, R., & Usov, V. V. 1997, *MNRAS*, 288, 237
- Panagia, N. & Felli, M. 1975, *A&A*, 39, 1
- Paumard, T., Maillard, J. P., Morris, M., & Rigaut, F. 2001, *Å*, 366, 466
- Plummer, H. C. 1911, *MNRAS*, 71, 460
- Prescher, M., & Melia, F. 2005, *ApJ*, 632, 1048
- Raga, A. C., Navarro-González, R., & Villagrán-Muniz, M. 2000, *Rev. Mex. Astron. Astrophys.*, 36, 67
- Raga, A. C., Velázquez, P. F., Cantó, J., Masciadri, E., & Rodríguez, L. F. 2001, *ApJL*, 559, L33
- Rasio, F. A. 1999, in the 5th International Conference on Computational Physics (ICCP5), held in Kanazawa, Japan, Oct 11-13 (Progress of Theoretical Physics)
- Revnivtsev, M. G., Churazov, E. M., Sazonov, S. Yu., Sunyaev, R. A., Lutovninov, A. A., Gilfanov, M. R., Vikhlinin, A. A., Shtykovsky, P. E., & Pavlinsky, M. N. 2004, *A&A*, 425, L49
- Rieke, G. H. & Rieke, M. J. 1988, *ApJL*, 330, L33
- Rockefeller, G., Fryer, C. L., Melia, F., & Warren, M. S. 2004, *ApJ*, 604, 662
- Rockefeller, G., Fryer, C. L., Baganoff, F. K., & Melia, F. 2005a, *ApJL*, 635, L141
- Rockefeller, G., Fryer, C. L., Melia, F., & Wang, Q. D. 2005b, *ApJ*, 523, 171
- Rockefeller, G., Fryer, C. L., & Melia, F. 2005c, *ApJ*, 635, 336
- Salmon, J. K. & Warren, M. S. 1994, *J. Comput. Phys.*, 111, 136
- Sedov, L. I. 1959, "Similarity and Dimensional Methods in Mechanics" (New York: Academic Press)

- Sellgren, K., Hall, D. N. B., Kleinmann, S. G., & Scoville, N. Z. 1987, *ApJ*, 317, 881
- Sellgren, K., McGinn, M. T., Becklin, E. E. & Hall, D. N. 1990, *ApJ*, 359, 112
- Serabyn, E., Guesten, R., Walmsley, J. E., Wink, J. E., & Zylka, R. 1986, *A&A*, 169, 85
- Serabyn, E., Shupe, D., & Figer, D. F. 1998, *Nature*, 394, 448
- Sidoli, L. 1999, Ph.D. thesis, Univ. degli Studi di Milano
- Springel, V., Yoshida, N., & White, S. D. M. 2001, *New Astronomy*, 6, 79
- Springel, V. 2005, *MNRAS*, 364, 1105
- Steinmetz, M., & Müller, E. 1993, *Å*, 268, 391
- Sunyaev, R., & Churazov, E. 1998, *MNRAS*, 297, 1279
- Sunyaev, R. A., Markevitch, M., & Pavlinsky, M. 1993, *ApJ*, 407, 606
- Suryadeep, R. 2004, *Å*, 25, 103
- Sutherland, R. S. & Dopita, M. A. 1993, *ApJ*, 88, 253
- Sutton, E. C., Danchi, W. C., Jaminet, P. A., & Masson, C. R. 1990, *ApJ*, 348, 503
- Tanner, A., Figer, D., Najarro, F., Kudritzki, R. P., Gilmore, D., Morris, M., Becklin, E. E., McLean, I. S., Gilbert, A. M., Graham, J. R., Larkin, J. E., Levenson, N. A., & Teplitz, H. I. 2006, *ApJ*, 641, 891
- Taylor, G. I. 1950, *Proc. R. Soc. London*, A201, 159
- Thacker, R. J., Tittley, E. R., Pearce, F. R., Couchman, H. M. P., & Thomas, P. A. 2000, *MNRAS*, 319, 619
- Tillotson, J. H. 1962, General Atomic Report GA-3216
- Vainshtein, L. A. & Sunyaev, R. A. 1980, *Soviet Ast.*, 6, L353
- Wadsley, J. W., Stadel, J., & Quinn, T. 2004, *New Astronomy*, 9, 137
- Wang, Q. D. 2003, IAU Symposium No. 214: High Energy Processes and Phenomena in Astrophysics, Eds: X. D. Li, V. Trimble, & Z. R. Wang., 214, 32
- Wang, Q. D. 2004, in preparation
- Warren, M. S. & Salmon, J. K. 1993, in *Supercomputing '93* (Los Alamitos; IEEE Comput. Soc.), 12

- Warren, M. S. & Salmon, J. K. 1995, *Comp. PhysComm.*, 87, 266
- Wellstein, S. & Langer, N. 1999, *ã*, 350, 148
- Wheeler, J. C., Mazurek, T. J., & Sivaramakrishnan, A. 1980, *ApJ*, 237, 781
- Young, P. A., Fryer, C. L., Hungerford, A. L., Arnett, D., Rockefeller, G., Meakin, C., & Eriksen, K. A. 2006, *ApJ*, 640, 891
- Yusef-Zadeh, F. & Melia, F. 1991, *ApJL*, 385, L41
- Yusef-Zadeh, F., Roberts, D. A., Goss, W. M., Frail, D. A., & Green, A. J. 1996, *ApJL*, 466, L25
- Yusef-Zadeh, F., Roberts, D. A., Goss, W. M., Frail, D. A., & Green, A. J. 1999, *ApJ*, 527, 172
- Yusef-Zadeh, F., Law, C., Wardle, M., Wang, Q. D., Fruscione, A., Lang, C. C., & Cotera, A. 2002, *ApJ*, 570, 665
- Zhao, J.-H., Bower, G. C., & Goss, W. M. 2001, *ApJL*, 547, L29